Dusty Super Star Cluster Winds: Their Impact on the Interstellar Medium and Infrared Manifestations

by

Sergio Martínez González

Thesis submitted in partial fulfillment of the requirements

for the degree of

DOCTOR OF SCIENCE IN ASTROPHYSICS

at the

Instituto Nacional de Astrofísica, Óptica y Electrónica

December 2015

Tonantzintla, Puebla

Advised by:

Ph.D. Guillermo Tenorio-Tagle

Tenured Researcher INAOE

Ph.D. Sergiy Silich

Tenured Researcher INAOE

Abstract

In light of the growing evidence pointing at core-collapse supernovae as large dust producers, and given their immense number in young massive stellar clusters (SSCs), this work is devoted to address the influence of stochastic injection, sputtering and outflow of dust grains on their emission properties inside the hot and dense intracluster medium. The theory of dust radiative cooling, which considers time-dependent dust size distributions and chemical composition, is combined with a self-consistent semi-analytic method, in order to study the hydrodynamics of spherically symmetric winds driven by SSCs with a generalized Schuster stellar density profile. The location of the critical line, which separates stationary from thermally unstable winds, defined by Tenorio-Tagle et al. (2007) is thus reexamined. In addition, the dusty wind model is applied to the high-velocity blue-shifted absorption features observed in the optical spectra of the central cluster of *PHL 293B*. Then infrared spectral energy distributions which are to be expected from the dusty interior of SSCs are presented using the theory of stochastic dust temperature fluctuations. The last part of the thesis is focused on studying the effects that radiation pressure, acting on dust grains and recombining atoms, has on the distribution of density and thermal pressure within wind-blown shells and thus how it may affect the velocity of the outer shock and the dynamics of the ionized gas around young stellar clusters. As a result of all these considerations, this work offers predictions for the observational manifestations of young dusty star clusters in the infrared, optical, ultraviolet and X-ray regimes.

Resumen

A la luz de la creciente evidencia que apunta a las supernovas tipo II como grandes productoras de polvo, y dado su inmenso número en súper cúmulos estelares jóvenes (SSCs, por sus siglas en inglés), este trabajo está dedicado a estudiar la influencia de la inyección estocástica, pulverización y flujo de granos de polvo en sus propiedades de emisión dentro del caliente y denso medio intracúmulo. La teoría del enfriamiento radiativo inducido por polvo, la cual considera una distribución de tamaños del polvo dependiente del tiempo y su composición química, es combinada con un método semi-analítico autoconsistente para estudiar la hidrodinámica de los vientos producidos por cúmulos esféricamente simétricos con un perfil de densidad estelar del tipo Schuster. La localización de la línea crítica, que separa vientos estacionarios y vientos térmicamente inestables, definida por Tenorio-Tagle et al. (2007), es reexaminada. Además, el modelo de vientos con polvo es aplicado a las líneas en absorción de alta velocidad corridas hacia el azul observadas en el espectro óptico del cúmulo central de la galaxia enana *PHL 293B*. A continuación se presentan distribuciones espectrales de energía en el infrarrojo que son esperadas del interior polvoriento en SSCs usando la teoría de las fluctuaciones estocásticas de la temperatura del polvo. La última parte de la tésis está enfocada en estudiar los efectos que la presión de radiación, actuando en granos de polvo y átomos recombinantes, tiene en las distribuciones de densidad y presión térmica de los cascarones empujados por vientos y por lo tanto, cómo se afectaría la velocidad del choque externo y la dinámica del gas ionizado alrededor de cúmulos estelares jóvenes. Como resultado de todas estas consideraciones, este trabajo ofrece predicciones para las manifestaciones observacionales de estos cúmulos con polvo en los regímenes infrarrojo, óptico, ultravioleta y de rayos X.

Contents

Chapter 1

Introduction

The study of the energy and momentum transfer from plasma particles to dust grains is a key issue in astrophysics; from comet tails (Finson & Probstein, 1968), planetary atmospheres (Pollack et al., 1979), molecule formation (Dieter & Goss, 1966) and the collapse of molecular clouds (Goldreich & Kwan, 1974) in the interstellar medium, to the large scale structure of the intergalactic and intracluster medium (cf. Spitzer, 1978; Stickel et al., 1998; Wright, 1981).

As cosmic dust grains cover a large range in sizes, from angstrom to micron scales, they are very effective at absorbing/scattering light at wavelengths comparable to their sizes. This large range of grain sizes make them also prone to suffer multiple inelastic collisions with the particles in a hot plasma (atomic nuclei, free electrons, molecules and even other dust grains). As a consequence of these collisions, the gas cools down, dust grains are heated up and then reemit some fraction of the previously gained energy in the infrared regime; redistributing the spectral energy distributions expected from plasma environments. On the other hand, dust in HII regions absorb an important fraction of the ionizing flux from the central star cluster and, as a consequence, the size of the HII region is diminished. Another consequence is that radiation pressure acting on dust grains may pile up the ionized gas and thus reconfigure the dynamics and inner structure in dusty HII regions.

Very efficient condensation of dust grains occurs either in the circumstellar envelopes of AGB stars (Ferrarotti & Gail, 2001) and in the ejecta of core-collapse (Type II) supernovae and less efficiently in Type Ia supernovae and in novae (Temim et al., 2015). Dust production in coeval star clusters is dominated by core-collapse SN during the first ~ 40 yr of their evolution, while AGB stars increasingly start to contribute at ~ 30 Myr, becoming dominant between 150 and 500 Myr (Valiante et al., 2009).

The idea of core-collapse supernovae as major dust producers was first envisaged in the pioneering work of Cernuschi, Marsicano, & Codina (1967). They showed that the effective condensation of refractory elements to the large variation of temperature in the ejecta of core-collapse supernovae can lead to the formation of massive quantities of dust.

However, it took more than two decades until *SN1987A* provided the first direct evi-

dence for the condensation of iron into dust grains (Bautista et al., 1995; Moseley et al., 1989, and references therein) in the SN ejecta. According to Todini & Ferrara (2001) and Nozawa et al. (2003), one can expect the formation of $(0.1 - 1)$ M$_\odot$ of dust in the first decades after a type II SN event while a dust mass fraction between 0.2-1.0 would be destroyed by the supernova reverse shock before being injected into the ISM (Nozawa et al., 2007).

These predictions find strong support in recent Herschel and ALMA observations of nearby supernova remnants like the *Crab Nebula*, *Cassiopeia A* and *SN1987A*. Gomez et al. (2012) found evidence for the presence of $0.1 - 0.25$ M$_\odot$ of ejected dust in the Crab Nebula, a value that is orders of magnitude higher than what was obtained with Spitzer data (Temim et al., 2012). Barlow et al. (2010) estimated 0.075 M$_\odot$ of cool dust (~ 35 K) in the ejecta of Cassiopeia A, however, due to high cirrus contamination along the line of sight, they were not able to identify the presence of cold dust (~ 20 K) which can increase the content of dust in the ejecta to values in the range of $0.5 - 1.0$ M$_\odot$ (Gomez, 2013). Indebetouw et al. (2014) and Matsuura et al. (2014) fitted the spectral energy distribution of SN1987A and derived ~ 0.8 M$_\odot$ of newly formed dust in the ejecta of the supernova with ~ 0.3 M$_\odot$ of amorphous carbon and ~ 0.5 M$_\odot$ of silicates.

1.1 Dusty Super Star Cluster Winds

The large SN rate expected in super star clusters (SSCs) (a few thousand SN events during the type II SN era for a 10^5 M$_\odot$ star cluster), together with the large production of dust, implies a continuous replenishment of dust inside the star cluster volume (Tenorio-Tagle et al., 2013). On the other hand, the thermalization of the matter reinserted by massive stars and SNe leads to the launching of hot ($\sim 10^7$ K) and dense (1-1000 cm^{-3}) super star cluster winds in which newly formed dust grains are immersed. These considerations make super star clusters ideal laboratories to study dust grains heated due to the transfer of thermal energy from the gas via stochastic collisions with electrons and nuclei as discussed by Dwek (1986). Dust grains then cool down in a short time scale (a few seconds to several hours) and re-emit the obtained energy in the infrared regime. This is a very effective cooling mechanism for the hot and dusty gas which can surpass the cooling from a gas in collisional ionization equilibrium by several orders of magnitude (Dwek, 1987; Dwek & Werner, 1981; Guillard et al., 2009; Ostriker & Silk, 1973; Smith et al., 1996). Therefore, dust effectively redistributes the energy in the starburst spectra producing infrared excesses with respect to the stellar continuum and nebular emission. These led Reines et al. (2008) to invoke a hot dust component (~ 800 K) to fit the near infrared spectral energy distributions observed in the bright SSCs 1 and 2 in *SBS 0335-052*. Similar infrared excesses have been observed in a considerable number of star clusters in low-metallicity blue compact dwarf galaxies, e.g *SBS 0335-052E, Haro 11, Mrk 930* and *IZw18* (Adamo et al., 2010a, 2011, 2010b; Fisher et al., 2014; Izotov et al., 2014; Vanzi et al., 2000).

1.2 The feedback from Massive Star Clusters

Super star clusters (SSCs) are high-density coeval young stellar systems with masses between $10^5 - 10^7$ M$_\odot$ within a radius of few parsecs (Whitmore, 2000). They are usually found in interacting and starburst galaxies (Portegies Zwart et al., 2010) with an intense mode of star formation, such as the most luminous HII and starburst galaxies (Johnson et al., 2000; Meurer et al., 1995; O'Connell et al., 1994; Whitmore & Schweizer, 1995, and references therein).

The feedback from massive young stellar clusters to the interstellar gas determines the natural link between the stellar and gaseous components in galaxies. Their high velocity outflows affect the structure of the interstellar medium (ISM) which then can be described as collection of shells expanding around an X-ray emitting region (Wang et al., 2010). Such shells accumulate and compress the interstellar matter often creating secondary generations of star forming clumps within the expanding shells (Oey et al., 2005) and massive young stellar systems in the shell sections that collide with other shells, as it seems to be the case of *30 Dor* and other regions in the *Large Magellanic Cloud* (Book et al., 2009; Dawson et al., 2013). The expanding shells trap the ionizing radiation produced by the central clusters affecting the dynamics and the distribution of their ionized gas.

In the case when a star cluster wind impacts a constant density ISM, a four zone structure is established: there is a central free wind zone, surrounded by a shocked wind region. The latter is separated by a contact discontinuity from the matter swept up by the leading shock which evolves into the constant density ISM (cf. Koo & McKee, 1992; Mac Low & McCray, 1988; Weaver et al., 1977).

In their pioneer work, Chevalier & Clegg (1985, hereafter CC85), presented an analytical solution for winds driven by starbursts of radius R_{SC} with uniform stellar density distribution and constant energy deposition rates. They proposed that star cluster winds are formed due to the efficient thermalization of the kinetic energy caused by random collisions of gas ejected by supernova explosions and stellar winds. This produces a large central overpressure that allows the reinserted matter to accelerate and form strong outflows, the star cluster winds.

Cantó et al. (2000) compared the CC85 analytic predictions with winds generated by a collection of individual stars (with a mean separation of 0.1 pc). They also carried out numerical simulations and found that the analytic solution and the numerical results are in a reasonable agreement. These adiabatic models predict the existence of extended X-ray envelopes that could be observationally detected.

In these models, the expansion velocity grows rapidly from zero km s^{-1} at the star cluster center to the sound speed at the star cluster surface R_{SC}, while the density, pressure and temperature of the reinserted gas remain almost uniform. However, outside R_{SC}, the hydrodynamical properties of the resultant wind outflow (the run of density, temperature and expansion velocity), asymptotically approach $\rho \sim r^{-2}$, $T \sim r^{-4/3}$ and $u \sim V_{A\infty}$, respectively, where $V_{A\infty}$ is the adiabatic wind terminal velocity.

Silich et al. (2004) presented a self-consistent stationary semi-analytic solution for

3

spherically symmetric winds driven by massive star clusters with a homogeneous stellar density distribution which includes radiative cooling. They also found that radiative cooling may change significantly the temperature distribution of the wind in the case of very massive and compact star clusters. They found a threshold line in the plane L_{SC} $vs.$ R_{SC} (where L_{SC} is the mechanical luminosity), above which the stationary wind solution is inhibited.

Additionally, they discussed the solution topology for the hydrodynamic equations. In their model, there are three possible types of integral curves: the stationary wind solution in which the sonic point is located at the star cluster surface and the flow is subsonic inside and supersonic outside the star cluster. The breeze solution in which the central temperature is smaller than in the stationary wind solution; the sonic point is shifted outside the star cluster and and leads to zero velocity at infinity. The unphysical double valued solution in which the central temperature is larger than in the stationary wind case.

Tenorio-Tagle et al. (2007) confirmed with 1D numerical simulations the location of the threshold line found in Silich et al. (2004) in the case of a homogeneous distribution of stars and found solutions above that threshold line. In that case, the singular point remains fixed at the star cluster surface and the stagnation point (R_{st}; the point where the expansion velocity is zero km s^{-1}), moves from the star cluster center towards the star cluster surface when more massive and compact clusters are considered. This is because densest regions result in an immediate loss of pressure and of the outward pressure gradient. These results were confirmed by both, 1D and 2D numerical simulations (Tenorio-Tagle et al., 2010; Wünsch et al., 2008). They concluded that the importance of cooling increases for larger mass clusters. For a given cluster radius, when the cluster mass surpasses a critical value, the stationary wind solution vanishes.

On the other hand, Rodríguez-González et al. (2007) proposed a non-radiative analytic wind model for star cluster winds with a power-law stellar density distribution, $\rho_* \propto R^\alpha$, where α is a constant and R the distance to the star cluster center. They introduced a truncation radius, R_c, to impose a star cluster surface and assumed that the singular point is located exactly at $R = R_c$. They also compared the analytic star cluster wind solutions with 3D numerical simulations and obtained a good agreement. Ji et al. (2006), solved one-dimensional hydrodynamic equations numerically and obtained stationary adiabatic wind solutions for star clusters with an exponential stellar density distribution $\rho_* \propto \exp(-r/R_c)$, where r is the distance to the star cluster center and R_c the star cluster core radius. They confirmed that the location of the singular point depends on the stellar density distribution alone. The impact of radiative cooling on winds driven by stellar clusters with an exponential stellar density distribution was explored by Martínez-González (2011), where a semi- analytic method was developed, which allows one to localize the position of the singular point and calculate the run of all hydrodynamical variables in this case. However, the observed star cluster brightness profiles, which can be linked to the stellar density distribution, are quite different from those discussed in the above studies.

In most cases a generalized Schuster density profile (see Ninkovic, 1998) with $\rho_* \propto [1 + (r/R_c)^2]^{-\beta}$ and $\beta = 1.5$, where R_c is the core radius of the cluster stellar distribution, provides the best fit to the empirical mass distribution in young stellar clusters (Veltmann, 1979). Elson et al. (1987) revealed that the generalized Schuster model with $\beta = 1.75$, provides a very good fit to the stellar densities of young stellar clusters in the *Large Magellanic Cloud*. Furthermore, Mengel et al. (2002) used HST observations of young stellar clusters in the *Antennae galaxies* (Whitmore et al., 1999), and found that a King model (King, 1962, 1966) provides the best agreement with the observed stellar surface densities, corresponding to a generalized Schuster model (Ninkovic, 1998).

1.3 Dusty HII Regions

HII regions are fundamental to our understanding of young stellar clusters radiative and mechanical feedback on the interstellar medium (ISM). They are strong sources of emission-line radiation and thus are powerful diagnostic tool to study star formation as well as the chemical composition of local and high-redshift galaxies (Capriotti & Kozminski, 2001; Dopita et al., 2006, 2005; Yeh & Matzner, 2012). The idealized (Strömgren, 1939) model for spherical static HII regions with a homogeneous density distribution was a revolutionary step forward in the study of photoionized nebulae. However the consideration of a number of physical effects have led to a much more robust paradigm. Winds produced by the exciting clusters (Arthur, 2012; Capriotti & Kozminski, 2001; Silich & Tenorio-Tagle, 2013) and the impact that radiation pressure provides on the swept-up interstellar gas (Capriotti & Kozminski, 2001; Elmegreen & Chiang, 1982; Krumholz & Matzner, 2009; Matzner, 2002; Nath & Silk, 2009; Sharma & Nath, 2012) are among such major physical effects. As shown by Draine (2011), the absorption of photons emerging from an exciting cluster by dust grains and recombining atoms, leads to a non homogeneous density distribution even within static or pressure confined HII regions and under certain conditions, radiation pressure may pile up the ionized gas into a thin outer shell, as assumed by Krumholz & Matzner (2009). The action of cluster winds, together with the strong evolution of the ionizing photon flux and the star cluster bolometric luminosity make the situation even more intricate (Silich & Tenorio-Tagle, 2013).

Powerful winds driven by SSCs form strong shocks that move supersonically and sweep the ambient ionized gas into thin, wind-driven shells. These shells cool down in a short time scale and begin to absorb ionizing photons causing the ionization front to move back towards the cluster and finally become trapped within the shell. The size and density distribution of such ionized shells have little to do with the original Strömgren model. Their evolution depends not only on the ambient gas density distribution and the available Lyman continuum, but also on the mechanical power of the exciting cluster. Silich & Tenorio-Tagle (2013, hereafter ST13) discussed the impact that radiation pressure has on the dynamics of wind-driven shells powered by young star clusters and found radiation pressure not to be a dominant factor. They, however, did not consider

5

the detailed impact that radiation pressure provides on the inner shell structure. They also assumed that shells absorb all photons escaping from the central cluster and thus found an upper limit to the radiative feedback from the central cluster on the dynamics of the swept-up shell.

1.4 Aims of the Thesis

The ultimate goal of this thesis is to provide a theoretical framework for the physical interpretation of observations dealing with massive young stellar clusters and their impact on the ambient ISM.
In this respect, the major issues which are addressed throughout this work are:

- Using a semi-analytic self consistent method, to evaluate the role that the stellar density distribution has on the hydrodynamical properties of the matter reinserted within young and massive stellar clusters.

- Given the large SN rate and large dust production inside young and massive stellar clusters, to combine the theory of stochastic dust injection, stochastic dust temperature fluctuations and dust-induced radiative cooling with the hydrodynamics of the reinserted matter in such clusters.

- To provide infrared spectral energy distribution which are expected from the dust embedded into the hot and dense plasma within massive stellar clusters.

- To explore the effects of radiation pressure acting on dust grains and recombining atoms on the distribution of density and thermal pressure, as well on the dynamics of dusty wind-driven shells.

Other than infrared spectral energy distributions, this work offers predictions to the observational manifestations of young dusty star clusters in the optical, ultraviolet and X-ray regimes.

1.5 Structure of the Thesis

This thesis is organized as follows.
In Chapter 2, the various relevant physical processes involving dust grains embedded into hot and dense plasmas (dust cooling, stochastic temperature fluctuations, thermal sputtering) are explored.
In Chapter 3, a self-consistent hydrodynamic scheme for the matter reinserted within young and massive star clusters is developed with the use of realistic stellar density distributions and the consideration of radiative cooling.
In Chapter 4, the hydrodynamic scheme presented in the prior chapter is applied to models which account for cooling of a gas in collisional ionization equilibrium and

cooling induced by gas-grain collisions. The model predictions from the dusty winds are contrasted with the observational evidence of stationary high velocity blue-shifted absorption features in the spectra of *PHL 293B*.

In Chapter 5, stochastic dust injection by supernovae and stochastic dust heating and cooling physics are combined with hydrodynamical calculations to derive the dust emission and the expected spectral energy distributions from the matter reinserted within SSCs.

Chapter 6 is devoted to discuss the impact that dynamic and radiation pressure, acting on dust grains and recombining atoms, provide on the distribution of density and thermal pressure within dusty wind-blown shells and static HII regions.

Finally, Chapter 7 presents a brief summary of the main results gathered from this work and outlines possible extensions to it.

Chapter 2

Dust Immersed in a Hot Plasma

Dust grains immersed in a hot plasma ($\sim 10^6 - 10^7$ K) are subject to multiple collisions with free electrons and nuclei. After each collision, energy and momentum are transfered from the plasma to the dust grains. As a result, the gas cools down and the dust grains are at first heated, eroded and, in a short timescale, radiate a fraction of the previously gained energy in the infrared regime. This process is of special relevance in young massive star clusters in which frequent core-collapse supernovae lead to the stochastic injection of massive quantities of dust. In this Chapter, the theory describing these processes is presented and adapted to the cases of interest from this work. Section 2.1 is devoted to study the evolution of the grain size distribution due to thermal sputtering within the hot and dense plasma generated by young stellar clusters. In Section 2.2, the cooling law due to gas-grain collisions is presented. Finally Section 2.3 focuses on the theory of stochastic dust temperature fluctuations and the infrared flux expected from dust grains subject to a bath of free electrons.

2.1 Evolution of the Dust Size Distribution

The balance between the dust mass input rate and the rate at which dust is depleted (if it is destroyed or expelled out as a wind) within the hot and dense plasma generated by young stellar clusters, determines the range of the dust-to-gas mass ratio. Dust is injected into the intracluster with a certain initial dust size distribution, collisionally heated and eroded before the next injection episode. For this purpose, it is assumed that supernova explosions inject dust uniformly throughout the star cluster with a standard Mathis et al. (1977, hereafter MRN) grain size distribution (dust grain number density in the size interval a and $a + \Delta a$):

$$\frac{\partial n_i^{inj}}{\partial a} = A_i^{(m)} a^{-\alpha}, \ a_{min} \leq a \leq a_{max}, \tag{2.1}$$

where a_{min} and a_{max} are the minimum grain size and cut-off value of the size distribution. In this definition, subindex i is used to distinguish between dust species, in

9

this case graphite and silicate, and subindex m numbers the consecutive dust injection events.

Table 2.1: Dust Properties

Symbol	Silicate	Graphite	Definition
ρ_{gr}	3.3	2.26	Dust grain density (g cm^{-3}) [1]
α	3.5	3.5	Power index of the MRN distribution
f_i	0.5	0.5	Mass fraction of the grain species

[1] Hirashita & Nozawa (2013).

The normalization factors, $A_i^{(m)}$ (with units cm$^{\alpha-4}$), are obtained from the condition:

$$A_i^{(m)} = \frac{f_i M_{dSN}^{(m)}/V_{SC}}{\int_{a_{min}}^{a_{max}} \frac{4}{3}\pi\rho_{gr}a^{3-\alpha} \, \mathrm{d}a},$$ (2.2)

where ρ_{gr} is the dust grain density, f_i is the mass fraction of the silicate and graphite species, $M_{dSN}^{(m)}$ is the total mass of dust injected in a single supernova event and V_{SC} is the star cluster volume. Table 2.1 summarizes the input parameters for the injected dust size distribution and the characteristics of the dust species, i.e. graphite and silicate grains.

The dust lifetime against thermal sputtering at temperatures above 10^6 is defined as $\tau_{sput} = a/|\dot{a}|$; where $\dot{a}$, the rate at which the dust grain with radius a decreases with time t when dust is immersed into a hot plasma with temperature T and density n. It can be approximated from by the relation (Tsai & Mathews, 1995):

$$\dot{a} = \frac{\mathrm{d}a}{\mathrm{d}t} = -1.4nh\left[\left(\frac{T_s}{T}\right)^w + 1\right]^{-1},$$ (2.3)

where h, T_s and w are constants with values $h = 3.2 \times 10^{-18}$ cm^4 s^{-1}, $T_s = 2 \times 10^6$ K and $w = 2.5$. The above formula is an approximation to the detailed calculations of Draine & Salpeter (1979) and Tielens et al. (1994) for graphite and silicate grains. Equation (2.3) then predicts that a single dust grain with radius 0.001 μm, embedded into a 10^7 K plasma with density ~ 10 cm^{-3}, can survive for roughly one hundred years, while a grain with radius 0.1 μm immersed into the same conditions, is likely to survive for more than ten thousand years.

The continuity equation which governs the evolution of the dust size distribution due to thermal sputtering is (Laor & Draine, 1993; Yamada & Kitayama, 2005):

$$\dot{a}\frac{\partial}{\partial a}\left(\frac{\partial n_i}{\partial a}\right) + \frac{\partial}{\partial t}\left(\frac{\partial n_i}{\partial a}\right) = \begin{cases} A_i^{(m)}a^{-\alpha}/\tau_{inj}^{(m)}, \\ \text{if } t \leq \tau_{SN}^{(m)} + \tau_{inj}^{(m)}, \\ 0, \\ \text{if } t > \tau_{SN}^{(m)} + \tau_{inj}^{(m)}, \end{cases} \tag{2.4}$$

where the first case applies for a constant MRN dust injection during a timescale $\tau_{inj}^{(m)}$ after the m-supernova event has occurred (at $t = \tau_{SN}^{(m)}$); and the second case considers that the m-supernova dust injection has ceased. The solutions of equations (2.4) after the n-supernova event (the last event considered) are then:

$$\frac{\partial n_i}{\partial a} = \begin{cases} \displaystyle\sum_{m=1}^{n} \frac{A_i^{(m)}}{\tau_{inj}^{(m)}\dot{a}}\left[\frac{a^{-\alpha+1}}{(-\alpha+1)} - \frac{\left[a - \dot{a}(t - \tau_{SN}^{(m)})\right]^{-\alpha+1}}{(-\alpha+1)}\right], \\ \text{if } t \leq \tau_{SN}^{(m)} + \tau_{inj}^{(m)}, \\ \displaystyle\sum_{m=1}^{n} \frac{A_i^{(m)}}{\tau_{inj}^{(m)}\dot{a}}\left[\frac{\left[a - \dot{a}(t - \tau_{SN}^{(m)} - \tau_{inj}^{(m)})\right]^{-\alpha+1}}{(-\alpha+1)} - \frac{\left[a - \dot{a}(t - \tau_{SN}^{(m)})\right]^{-\alpha+1}}{(-\alpha+1)}\right], \\ \text{if } t > \tau_{SN}^{(m)} + \tau_{inj}^{(m)}, \end{cases} \tag{2.5}$$

with the conditions that $A_i^{(m)} = 0$ until the m-supernova event occurs and the mass of dust at $t = \tau_{SN}^{(1)} = 0$ equals zero. These general solutions take into account the residual mass of dust from the previous injections and the evolved dust size distribution associated to them.

The total mass of dust for each dust species as a function of time is then:

$$M_d(t) = \frac{4\pi}{3}\rho_{gr}V_{SC}\int_{a_{min}}^{a_{max}} a^3\frac{\partial n_i}{\partial a}\, da, \tag{2.6}$$

which implies a time-dependent dust-to-gas mass ratio given by:

$$Z_d(t) = \frac{4\pi}{3}\frac{\rho_{gr}}{\rho}\int_{a_{min}}^{a_{max}} a^3\frac{\partial n_i}{\partial a}\, da, \tag{2.7}$$

where $\rho = 1.4 m_H n$ is the gas mass density and m_H is the hydrogen mass.

Equation (2.7) shows that the dust-to-gas mass ratio must be smaller in more compact and more energetic clusters as in such clusters the average density of the reinserted matter is larger and thus the timescale for thermal sputtering is smaller. The average
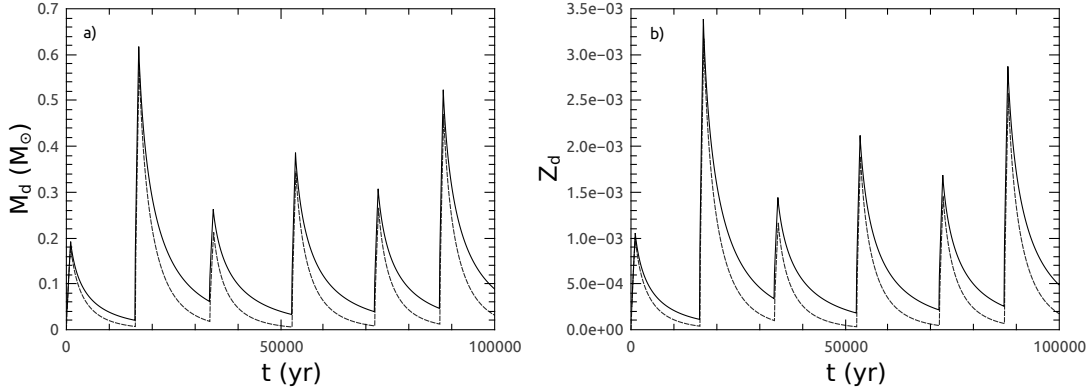
11

Figure 2.1: Evolution of the dust mass and dust-to-gas mass ratio with and without the exit of dust grains from the starburst region. Panels a) and b) show the residual $M_d(t)$ and dust-to-gas mass ratio, respectively, from 6 injection events with account of thermal sputtering. Solid lines depict the case when dust grains do not exit from the star cluster volume; dashed lines consider the case when dust is expelled out of the star cluster. This case corresponds to a 3×10^5 M$_\odot$ cluster with $V_{\infty A} = 1000$ km s^{-1}, $R_{SC} = 5$ pc and $R_c = 4$ pc. The values of $M_{dSN}^{(m)}$ and the interval between consecutive supernova events $\Delta\tau_{SN}^{(m)}$ were pseudo-randomly selected. Note that the exit of dust grains from the star cluster leads to a rapid depletion of dust at $r \leq R_{SC}$.

gas number density also increases in clusters with smaller $V_{A\infty}$ what leads to a strong dependence of Z_d on the adiabatic wind terminal speed.

The above equations do not take into account that dust, independent of its size, is expelled out from the cluster and thus $A_i^{(m)}$ is no longer a constant. The rate at which dust is ejected from the cluster is $\dot{M}_d(t) = 4\pi R_{SC}^2 \rho c_s Z_d(t)$; where c_s is the outflow's local sound speed obtained from the wind hydrodynamical calculations.

In order to consider dust outflowing from the cluster, a finite differences approach was considered, and it is described as follows: (1) calculate $M_d(t)$ with the original value of $A_i^{(m)}$ at $t = \tau_{SN}^{(m)} + \Delta t$; (2) at the next time-step, $t = \tau_{SN}^{(m)} + 2\Delta t$, subtract $\dot{M}_d(t)\Delta t$ to $M_d(t)$ and with this mass, replace $A_i^{(m)}$ with

$$A_i^{(m)'} = \frac{f_i \left[M_d(t) - \dot{M}_d(t)\Delta t \right] / V_{SC}}{\dfrac{1}{A_i^{(m)}} \displaystyle\int_{a_{min}}^{a_{max}} \frac{4}{3}\pi\rho_{gr}a^3 \frac{\partial n_i}{\partial a}(t)\, \mathrm{d}a};$$ (2.8)

(3) repeat the procedure for every time-step and for the normalization constants associated to each supernova dust injection. In these calculations, Δ was taken as $t = 100$ yr and $\tau_{inj}^{(m)} = \tau_{inj} = 1000$ yr (the same timescale for every dust injection). This method was compared to the analytic solution (equations 2.1-2.7), in the case when $\dot{M}_d(t) = 0$, and both methods agree very well.

These considerations, imply the presence of a time-dependent reservoir of dust grains

12

embedded into the high-temperature ($\sim 10^6$-10^7 K) thermalized gas inside the star cluster volume. As it will be explored in the next chapters, this has profound implications on the hydrodynamics of the matter reinserted within SSCs.

2.2 The Cooling Function

The idea that dust is by far the main gas coolant at high temperatures was first envisaged by Ostriker & Silk (1973) who showed that the radiation from dust particles becomes dominant over that generated by a gas in collisional ionization equilibrium at temperatures $T \geq 10^6$ K. Dust cooling can surpass by more than two orders of magnitude the gas cooling including radiative processes at $T \geq 10^7$ K and bremsstrahlung cooling at $T \sim 10^8 - 10^9$ K.

Several authors (e.g Burke & Silk, 1974; Draine, 1981; Dwek, 1981, 1987; Dwek & Werner, 1981) have considered the effects on the dust cooling law obtained from different dust properties which include different grain sizes, chemical compositions, erosion, electrical charge and shock velocities. Dust cooling has been applied to the intergalactic matter in galaxy clusters, Seyfert galaxies, supernova and their remnants, among other astrophysical environments (cf. Everett & Churchwell, 2010; Guillard et al., 2009; Montier & Giard, 2004; Smith et al., 1996). Here the general procedures to obtain the cooling law due to gas-grain collisions are outlined. These calculations are based on the prescriptions given by Dwek (1987) and include the effects of considering chemical composition and different dust size distributions.

2.2.1 Dust Cooling Calculations

Following Dwek (1987), and keeping most of his notations and definitions, the cooling rate due to the gas-grain collisions in a dusty plasma with a normal chemical composition (one He atom per every ten H atoms) is calculated as:

$$\Lambda_d = \frac{n_d}{n_e n} H_{coll} = \frac{1.4 m_H Z_d}{\rho_d} \left(\frac{32}{\pi m_e} \right)^{1/2} \pi (k_B T)^{3/2} \left[h_e + \frac{11}{23} \left(\frac{m_e}{m_H} \right)^{1/2} h_n \right], \quad (2.9)$$

where n, n_d and n_e are the gas, dust and electron number density, H_{coll} is the heating rate of a single grain due to collisions with incident gas particles and k_B is the Boltzmann constant. Functions h_e and h_H are the effective grain heating efficiencies due to impinging electrons and nuclei, respectively:

$$h_e = \int_{a_{min}}^{a_{max}} \int_0^\infty \frac{\zeta(a, E)}{2} x_e^2 e^{-x_e} a^2 \frac{\partial n_i}{\partial a} \, \mathrm{d}x_e \, \mathrm{d}a, \quad (2.10)$$

$$h_n = \int_{a_{min}}^{a_{max}} \left\{ \left[1 - \left(1 + \frac{x_H}{2} \right) e^{-x_H} \right] + \frac{1}{2} \left[1 - \left(1 + \frac{x_{He}}{2} \right) e^{-x_{He}} \right] \right\} a^2 \frac{\partial n_i}{\partial a} \, \mathrm{d}a,$$
$$(2.11)$$

13

where $\rho_d = 4/3\pi\rho_{gr} \int_{a_{min}}^{a_{max}} a^3 \frac{\partial n_i}{\partial a}\, \mathrm{d}a$ is the size-averaged dust density, ρ_{gr} is the grain density, $x_e = E/k_B T$, E is the energy of the impinging electron, $\zeta(a, E)$ is the fraction of the electron kinetic energy transfered to the dust grain, $x_H = E_H/k_B T$, $x_{He} = E_{He}/k_B T$ and the energies from the incident hydrogen and helium nuclei are $E_H = 133a$ keV, $E_{He} = 222a$ keV, where a is measured in microns,

$$\zeta(a, E) = \begin{cases} 0.875, & \text{if } E \leq E^* \\ 1 - E_f/E, & \text{otherwise,} \end{cases} \tag{2.12}$$

where $E_f = max\{E', 0.125E\}$, with E^* and E', the critical energy at which an electron penetrates the dust grain and the final energy of the electron after penetrating the dust grain, respectively. E^* and E' are obtained by solving the following system of non-linear equations based on experimental data

$$\begin{align} \log R(E^*) &= \log(4a\rho_{gr}/3) = 0.146 \log E^{*2} + 0.5 \log E^* - 8.15, \tag{2.13} \\ \log R(E) &= 0.146 \log E^2 + 0.5 \log E - 8.15, \tag{2.14} \\ \log R(E') &= \log R(E) - R(E^*) = 0.146 \log E'^2 + 0.5 \log E' - 8.15. \tag{2.15} \end{align}$$
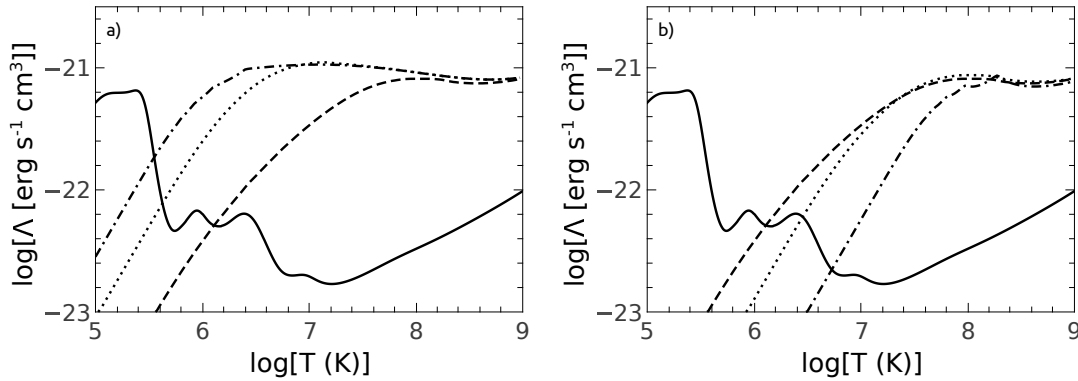

Figure 2.2: Cooling function for different dust size distributions as a function of temperature. In panel a), a_{min} is set to 0.001 μm and a_{max} takes the values 0.001, 0.01 and 0.5 μm (dashed, dotted, and dash-dotted lines, respectively). In panel b), a_{max} is set to 0.5 μm and a_{min} takes the values 0.001, 0.01 and 0.5 μm (dashed, dotted, and dash-dotted lines, respectively). In these calculations, it is assumed a dust-to-gas mass ratio of $Z_d = 10^{-3}$. In both panels, the interstellar cooling law for solar metallicity is presented as a solid curve.

In Figure 2.2, examples of dust cooling [1] curves are shown for different dust size distributions in which the value of the dust-to-gas mass ratio is set to $Z_d = 10^{-3}$. Appendix

---

[1] Despite the fact that the term 'dust cooling' seems to indicate the cooling of dust grains, here I follow the convention to use the term in reference to radiative cooling of gas due to gas-grain collisions.

A provides tables which contain the results of the calculations of the dust cooling function for different grain size distributions as a function of the gas temperature. They are normalized to the dust-to-gas mass ratio, for a_{min} set to 0.001 μm and different a_{max} values (Table A.1), and for a_{max} set to 0.5 μm and different a_{min} values (Table A.2).

2.3 Stochastic Dust Temperature Distribution

In order to calculate the temperature distribution of dust grains subject to a bath of free electrons in a hot gas, and thus the emission by such dust grains, the schemes proposed by Dwek (1986) and Guhathakurta & Draine (1989) are followed with a few extra considerations. In the Dwek's scenario, a dust grain with an initial temperature T_0, collides with a free electron with energy E which transfers a fraction of its kinetic energy, $\zeta(a, E)$, to the dust particle. Depending on the size and chemical composition of the dust grain (because its heat capacity, $C(a, T_d)$, is a function of both), the dust particle will be heated to a peak temperature T_{peak} (cf. Figure 2.3), which is obtained from iteration of the equation

$$\zeta(a, E)E = \int_{T_0}^{T_{peak}} C(a, T_d)\, \mathrm{d}T_d. \tag{2.16}$$

From T_{peak}, the dust particle starts to cool down and eventually, after many collisions, it acquires thermodynamic equilibrium unless the characteristic time for electron-grain collisions is larger than the grain cooling time, in which case the grain temperature will start to fluctuate (Dwek, 1986; Dwek & Arendt, 1992). The grain cooling time, τ_{cool}, between T_{peak} and some temperature T_d, is given by

$$\tau_{cool} = \int_{T_d}^{T_{peak}} \frac{C(a, T_d)\, \mathrm{d}T_d}{|4\pi a^2 \sigma \langle Q_{abs} \rangle T_d^4|}, \tag{2.17}$$

where σ is the Stefan-Boltzmann constant and $\langle Q_{abs} \rangle$ is the dust absorption efficiency, $Q_{abs}(\lambda, a)$ (cf. Figure 2.4), averaged by the Planck function, $B_\lambda(T_d)$ (in terms of the wavelength, λ):

$$\langle Q_{abs} \rangle = \frac{1}{\sigma T_d^4} \int_0^\infty \pi Q_{abs}(\lambda, a) B_\lambda(T_d)\, \mathrm{d}\lambda. \tag{2.18}$$

The values of $C(a, T_d)$ for silicate and graphite grains were taken from Dwek (1986) and from Draine & Anderson (1985), while the values of $Q_{abs}(\lambda, a)$ were obtained from the data files provided in the DustEM code [2] (Compiègne et al., 2011). On the other

---

[2] http://www.ias.u-psud.fr/DUSTEM
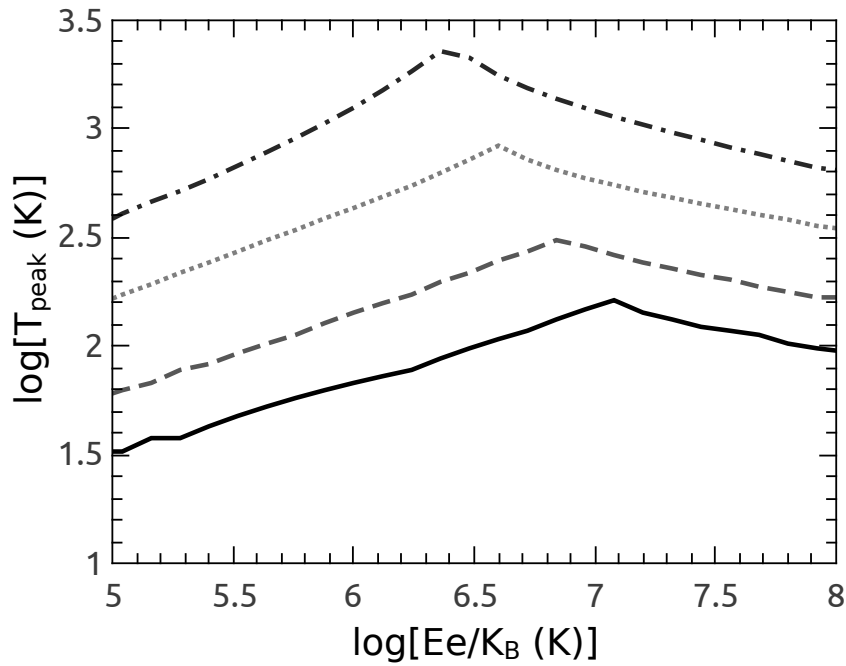
Figure 2.3: The peak temperature of a dust grain after a collision with an electron with energy E_e. The lines display the results for graphite grains with radius 0.01 μm (solid line), 0.005 μm (dashed line), 0.002 μm (dotted line) and 0.001 μm (dash-dotted line). The electron energies were normalized to the Boltzmann constant and presented in Kelvin units.
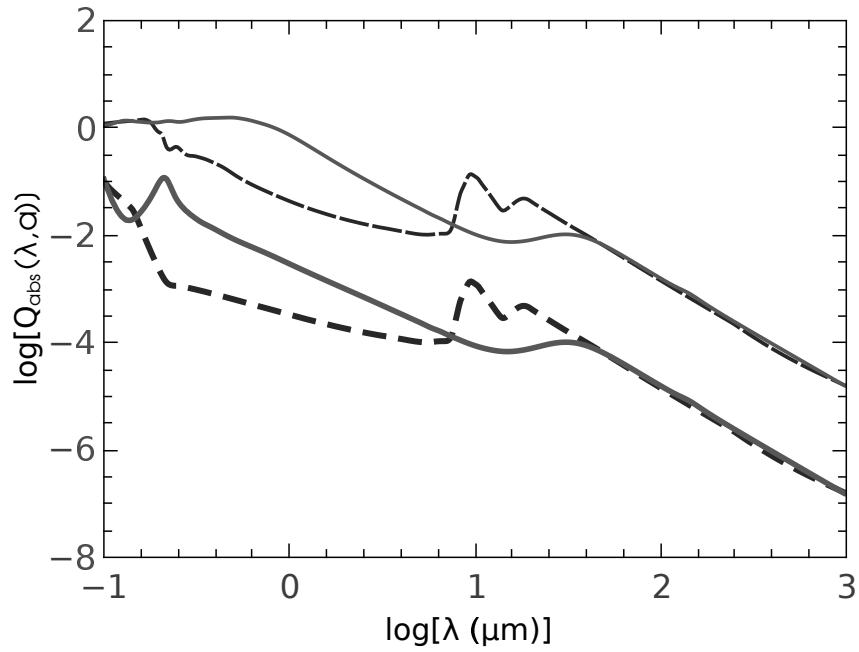
Figure 2.4: Dust absorption efficiencies, Q_{abs}, as a function of wavelength to the Mie calculations performed by Compiègne et al. (2011). The solid lines correspond to absorption efficiencies for a 0.001 μm graphite grain (thick solid line) and a 0.1 μm graphite grain (thin solid line). The dashed lines correspond to absorption efficiencies for a 0.001 μm silicate grain (thick dashed line) and a 0.1 μm silicate grain (thin dashed line).

17

hand, the characteristic time between successive electron collisions with a dust grain, τ_{coll}, is calculated as (Bocchio et al., 2013):

$$\tau_{coll}^{-1} = \pi a^2 n \sqrt{\frac{3k_B T}{m_e}}, \tag{2.19}$$

where m_e is the mass of the electron. The fraction of time in which a dust grain can be found in the temperature interval $T_d + \mathrm{d}T_d$ after a collision with an electron is (Purcell, 1976):

$$P(a, E, T_d, T_0)\,\mathrm{d}T_d = \begin{cases} \dfrac{C(a, T_d)}{4\pi a^2 \sigma \langle Q_{abs} \rangle T_d^4} \dfrac{e^{-\tau_{cool}/\tau_{coll}}}{\tau_{coll}}, & \text{if } T_d \leq T_{peak} \\ 0, & \text{otherwise.} \end{cases} \tag{2.20}$$

One can obtain now the probability, $G(a, T_d, T_0)$, that a dust grain is to be found between T_d and $T_d + \mathrm{d}T_d$ if one integrates the above quantity over all the electron energies according to the Maxwell-Boltzmann distribution

$$G(a, T_d, T_0) = \pi a^2 n \tau_{coll} \int_0^\infty P(a, E, T_d, T_0) f(E) v(E)\,\mathrm{d}E. \tag{2.21}$$

By evaluating equation (2.21), the temperature distribution of a population of grains with the same initial temperature T_0, size and chemical composition is obtained. In the above equation, $f(E)$ and $v(E)$ are the Maxwell-Boltzmann distribution of energy and the speed of the impinging electron, respectively. In order to obtain the temperature distribution of grains with a wide range of initial temperatures, the stochastic matrix method described by Guhathakurta & Draine (1989) and Marengo (2000) is employed. Let $\mathbf{A}_{T_d^i, T_0^j}$, be an $N \times N$ stochastic matrix, which describes the probability (per unit time) of a grain to make a transition between T_0 and some temperature T_d. The entries of $\mathbf{A}_{T_d^i, T_0^j}$ are obtained from evaluation of equation (2.21):

$$\mathbf{A}_{T_d^i, T_0^j} = \begin{pmatrix} G(a, T_d^1, T_0^1) & G(a, T_d^1, T_0^2) & \cdots & G(a, T_d^1, T_0^j) \\ G(a, T_d^2, T_0^1) & G(a, T_d^2, T_0^2) & \cdots & G(a, T_d^2, T_0^j) \\ \vdots & \vdots & \ddots & \vdots \\ G(a, T_d^i, T_0^1) & G(a, T_d^i, T_0^2) & \cdots & G(a, T_d^i, T_0^j) \end{pmatrix}. \tag{2.22}$$

In this work, a logarithmic grid for T_d and T_0, from 1 K to 1100 K and $N = 125$ was employed.

Let now $G_{n=0}^i$ be an initial temperature distribution given by a column vector which comes from evaluating equation (2.21) with $T_0 = T_0^{trial}$, a trial initial temperature:

18

$$G_{n=0}^i = \begin{pmatrix} G(a, T_d^1, T_0^{trial}) \\ G(a, T_d^2, T_0^{trial}) \\ \vdots \\ G(a, T_d^i, T_0^{trial}) \end{pmatrix}. \tag{2.23}$$

The stochastic matrix is applied to the initial temperature distribution to obtain a new stochastic temperature distribution, $G_{n=1}^i = G_{n=0}^i \mathbf{A}_{T_d^i, T_0^{trial}}$. One has to iterate the equation

$$G_{n+1}^i = G_n^i \mathbf{A}_{T_d^i, T_0^j}, \tag{2.24}$$

until the condition $(\mathbf{I} - \mathbf{A}_{T_d^i, T_0^j})G_{n+1} = 0$, with $\mathbf{I}$ the identity matrix, is fulfilled. This condition ensures that, after many discrete heating events, the temperature distribution does not change under the application of the stochastic matrix; this is the steady state temperature distribution, $G(a, T_d)$.

Big grains ($\gtrsim 0.1\ \mu$m), with large cross sections and heat capacities, are more likely to reach thermodynamic equilibrium due to very frequent collisions. In that case, their temperature distribution approaches a delta function around the equilibrium temperature, T_{eq}, which can be obtained by equating the heating and cooling rates:

$$\pi a^2 n \int_0^\infty f(E)v(E)\zeta(a, E)E\ \mathrm{d}E = 4\pi a^2 \sigma \langle Q_{abs} \rangle T_{eq}^4. \tag{2.25}$$

Once the dust temperature distribution is known, the infrared flux can be calculated from equation 15 of Dwek & Arendt (1992):

$$f_\lambda = \left(\frac{1.4 m_H Z_d N_H}{\rho_d} \right) \pi \Omega_{SC} \int_{a_{min}}^{a_{max}} \int_0^\infty a^2 \frac{\partial n_i}{\partial a} Q_{abs}(\lambda, a) B_\lambda(T_d) G(a, T_d)\ \mathrm{d}T_d\ \mathrm{d}a, \tag{2.26}$$

in units erg s^{-1} cm^{-2} Å^{-1}, or alternatively, in units erg s^{-1} cm^{-2} Hz^{-1} or Jansky, if one is interested in the flux per unit frequency, f_ν, where $\lambda f_\lambda = \nu f_\nu$. In this equation, Ω_{SC} is the solid angle subtended by the source, and N_H is the hydrogen column density through the source. In Figure 2.5 an example of the resultant infrared flux for an equal mix of silicate and graphite is presented with prevailing conditions inside the plasma set to $T = 1.35 \times 10^7$ K and $n = 10$ cm^{-3}. The dust properties are the same as those which will be used in Chapter 4 (see Table 2.1). The assumed column density is $N_H = 1.5 \times 10^{20}$ cm^{-2}, $Z_d = 10^{-3}$ and the distance to the source is 10 Mpc.

19

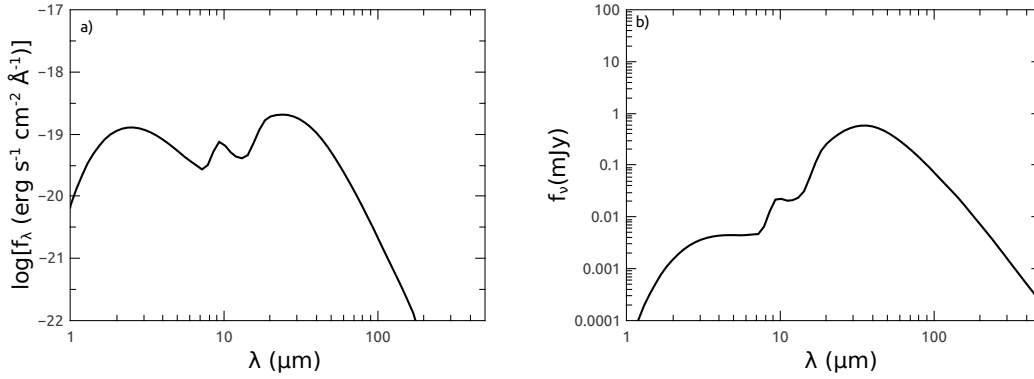Figure 2.5: Infrared flux from an equal mix of graphite and silicate. Panels a) and b) present the values of the fluxes per unit wavelength, f_λ, and per unit frequency, f_ν. In this case, the gas temperature and number density were set to $T = 1.35 \times 10^7$ K and $n = 10$ cm^{-3}. The assumed column density is $N_H = 1.5 \times 10^{20}$ cm^2 and the distance to the source is 10 Mpc.

20

Chapter 3

Hydrodynamic Scheme

The thermalization of the stellar winds and supernovae mechanical energy through nearby random collisions in young star clusters leads to a high central overpressure that results in powerful outflows; the star cluster winds. Previously in Martínez-González (2011) [1] , a semi-analytic method was developed to study the hydrodynamics of stationary spherically-symmetric winds driven by young super star clusters (SSCs) with an exponential stellar density distribution. The method allows to calculate the position of the singular/sonic point self-consistently.

In this Chapter, a step forward is taken towards considering more realistic stellar distributions. For this, a model for winds driven by SSCs with a generalized Schuster stellar mass distribution is constructed.

The Chapter is organized as follows: In Section 3.1, the star cluster model is described; i.e. the parameters for the compactness of the cluster, the mass density distribution, and mass and energy deposition rates are presented. In Chapter 3.2, the main hydrodynamic (mass, momentum and energy conservation) equations are adapted to this case and then combined and presented in a suitable form for numerical integration in a similar way to that described in Martínez-González (2011). Section 3.3 presents analytic limits for the flow velocity, density and temperature at the star cluster center. In Section 3.4, the integration procedure for the hydrodynamic equations is presented. Section 3.5 analyzes the position of the singular point at the quasi-adiabatic limit and calculates its minimum possible location.

3.1   Star Cluster Model

Consider young and compact spherical clusters with constant total mass and energy deposition rates, $\dot{M}$ and L_{SC}, and a generalized Schuster stellar mass density distribution (Ninkovic, 1998):

$$\rho_\star(r) = \frac{\rho_{\star 0}}{\left[1 + (r/R_c)^2\right]^\beta}, \tag{3.1}$$

---

[1] Available at http://www.researchgate.net/publication/261064967

where r is the distance from the cluster center, $\rho_{\star 0}$ is the central stellar density, R_c is the core radius of the stellar distribution and $\beta \geq 0$ defines the steepness of the stellar density distribution. The model considers star clusters in which other input parameters are: the star cluster mechanical luminosity, L_{SC}, and the adiabatic wind terminal speed $V_{A\infty}$, which are related to the mass deposition rate as $V_{A\infty}^2 = 2L_{SC}/\dot{M}$. It is assumed that the mechanical luminosity scales with the total mass of the star cluster, M_{SC}, as $L_{SC} = 3 \times 10^{39}(M_{SC}/10^5 \, \mathrm{M}_\odot) \, \mathrm{erg} \, \mathrm{s}^{-1}$ (Leitherer et al., 1999).
The cumulative mass within a given radius r is then:

$$M_{SC}(r) = \int_0^r \frac{4\pi\rho_{\star 0} r^2 \mathrm{d}r}{\left[1 + (r/R_c)^2\right]^\beta} = \frac{4\pi}{3}\rho_{\star 0} r^3 \,{}_2F_1(3/2, \beta, 5/2, -r^2/R_c^2), \qquad (3.2)$$

where ${}_2F_1$ is the Gauss hypergeometric function, ${}_2F_1(3/2, \beta, 5/2, -r^2/R_c^2)$, hereafter denoted as $F_\beta(r)$. If $\beta \leq 3/2$ and $r \to \infty$, the mass of the cluster is infinite. However, if $\beta > 3/2$, the cumulative mass is finite even if $r \to \infty$. In order to keep the cluster total mass finite even for $\beta \leq 3/2$, the stellar density distribution (equation 3.1) must be truncated at some radius R_{SC}. The consideration of the cluster radius R_{SC} is justified as a consequence of environmental effects, tides etc., which remove mass from the cluster periphery. Thus the radius R_{SC}, defines the star cluster edge. Both, R_c and R_{SC}, define the degree of compactness of the star cluster, which can be measured by the radius at which half of the star cluster mass is enclosed, R_{HM}. When $\beta = 3/2$ and $R_{SC}/R_c \to \infty$, equation (3.1) leads to the King (1962) surface density distribution (Ninkovic, 1998). Note, that in the case of a homogeneous stellar mass distribution ($\beta = 0$) the core radius R_c vanishes from all formulas.

Here it is assumed, as in CC85, that the mechanical energy deposited by massive stars and supernova explosions is thermalized in random collisions of nearby stellar winds and supernova and that the mass and energy deposition rates per unit volume, q_m and q_e follow the stellar density distribution:

$$q_e(r) = q_{e0} \left[1 + (r/R_c)^2\right]^{-\beta}, \qquad (3.3)$$

$$q_m(r) = q_{m0} \left[1 + (r/R_c)^2\right]^{-\beta}, \qquad (3.4)$$

where the constants q_{e0} and q_{m0} are:

$$q_{e0} = 3L_{SC}/4\pi R_c^3 F_\beta(R_{SC}), \qquad (3.5)$$

$$q_{m0} = 3\dot{M}/4\pi R_c^3 F_\beta(R_{SC}). \qquad (3.6)$$

3.2 Main Hydrodynamic Equations

The steady-state spherically symmetric hydrodynamic equations which take into consideration energy and mass continuously deposited to the flow (cf., for example, Silich et al., 2011, 2004, and references therein) are

$$\frac{1}{r^2}\frac{\mathrm{d}}{\mathrm{d}r}\left(\rho u r^2\right) = q_m, \tag{3.7}$$

$$\rho u \frac{\mathrm{d}u}{\mathrm{d}r} = -\frac{\mathrm{d}P}{\mathrm{d}r} - q_m u, \tag{3.8}$$

$$\frac{1}{r^2}\frac{\mathrm{d}}{\mathrm{d}r}\left[\rho u r^2\left(\frac{u^2}{2} + \frac{\gamma}{\gamma-1}\frac{P}{\rho}\right)\right] = q_e - Q, \tag{3.9}$$

where P, u, and ρ are the thermal pressure, the velocity and the density of the thermalized matter, $\gamma = 5/3$ is the ratio of specific heats, $Q = n^2\Lambda$ is the cooling rate, n is the wind number density. The cooling rate accounts the contribution for cooling from a gas in collisional ionization equilibrium, Λ_g which depends on the gas metallicity Z and temperature T (Raymond et al., 1976), and/or Λ_d, the cooling due to gas-grain collisions, which depends on the grain composition, size and also the gas temperature (cf. section 2.2).

The last term in the momentum conservation equation (3.8), $q_m u$, is negative because it is assumed that the thermalized injected material has zero momentum.

The integration of the mass conservation equation (3.7) yields:

$$\rho u r^2 = q_{m0} r^3 F_\beta(r)/3 + C. \tag{3.10}$$

If the central values of the wind density and the velocity are finite, the constant of integration, C, must be zero. Substituting equation (3.10) into equation (3.8), one can obtain

$$\frac{\mathrm{d}P}{\mathrm{d}r} = -\frac{q_{m0}r F_\beta(r)}{3}\frac{\mathrm{d}u}{\mathrm{d}r} - q_m u, \tag{3.11}$$

Using this expression and taking the derivative of equation (3.9):

$$q_m\left\{\frac{u^2}{2} + \frac{c^2}{\gamma-1}\right\} + \rho u\left\{u\frac{\mathrm{d}u}{\mathrm{d}r} + \frac{\mathrm{d}}{\mathrm{d}r}\frac{c^2}{\gamma-1}\right\} = q_e - Q, \tag{3.12}$$

one can present the main equations in a more suitable form for numerical integration:

$$\frac{\mathrm{d}u}{\mathrm{d}r} = \frac{(\gamma-1)(q_e - Q) + (\gamma+1)q_m u^2/2 - 2c^2\rho u/r}{\rho(c^2 - u^2)}, \tag{3.13}$$

$$\frac{\mathrm{d}P}{\mathrm{d}r} = -\rho u\frac{\mathrm{d}u}{\mathrm{d}r} - q_m u, \tag{3.14}$$

$$\rho = \frac{q_{m0}r}{3u}F_\beta(r), \tag{3.15}$$

23

where c is the local speed of sound, $c^2 = \gamma P/\rho$.

Given a cluster radius R_{SC}, outside of which there are no sources of mass and energy, the set of main equations for $r > R_{SC}$ is:

$$\frac{\mathrm{d}u}{\mathrm{d}r} = \frac{(\gamma - 1)rQ + 2\gamma pu}{r\rho(u^2 - c^2)}, \tag{3.16}$$

$$\frac{\mathrm{d}P}{\mathrm{d}r} = -\frac{\dot{M}}{4\pi r^2}\frac{\mathrm{d}u}{\mathrm{d}r}, \tag{3.17}$$

$$\rho = \frac{\dot{M}}{4\pi u r^2}, \tag{3.18}$$

where $\dot{M}$ is the flux of mass through the star cluster surface.

3.3 Analytic Limits at the Star Cluster Center

From equation (3.15), one can note that the central density remains finite and is not 0 g cm^{-3}, only if the wind velocity is 0 km s^1 at the star cluster center and grows linearly with radius near the center. The derivatives of the wind velocity and pressure at the star cluster center then are:

$$\frac{\mathrm{d}u}{\mathrm{d}r} = \left[(\gamma - 1)(q_{e0} - Q) - 2q_{m0}c_0^2/3\right]/\rho_0 c_0^2, \tag{3.19}$$

$$\frac{\mathrm{d}P}{\mathrm{d}r} = 0, \tag{3.20}$$

where c_0 is the sound speed at the star cluster center.

It is interesting to note, that these relations are identical to those, obtained for the exponential stellar density distribution (Martínez-González, 2011), and that they do not depend on the selected value of β. One has to make use of these equations in order to move from the center and start the numerical integration.

In the radiative wind model, the central gas density ρ_0 and the central temperature T_0 are related through the equation (Sarazin & White, 1987; Silich et al., 2004):

$$n_0 = q_{m0}^{1/2}\left[\frac{V_{A,\infty}^2/2 - c_0^2/(\gamma - 1)}{\Lambda}\right]^{1/2} \tag{3.21}$$

where $n_0 = \rho_0/\mu m_p$ is the central number density of ions and μm_p is the average mass per ion. The term $V_{A,\infty}^2/2 - c_0^2/(\gamma - 1)$ in equation (3.21) cannot be negative in order to have a density with a physical meaning. This is why the central temperature T_0 cannot exceed the adiabatic wind value (Chevalier & Clegg, 1985; Silich et al., 2004)

$$T_0^{max} = \frac{(\gamma - 1)\mu_i V_{A\infty}^2}{2\gamma k_B}. \tag{3.22}$$
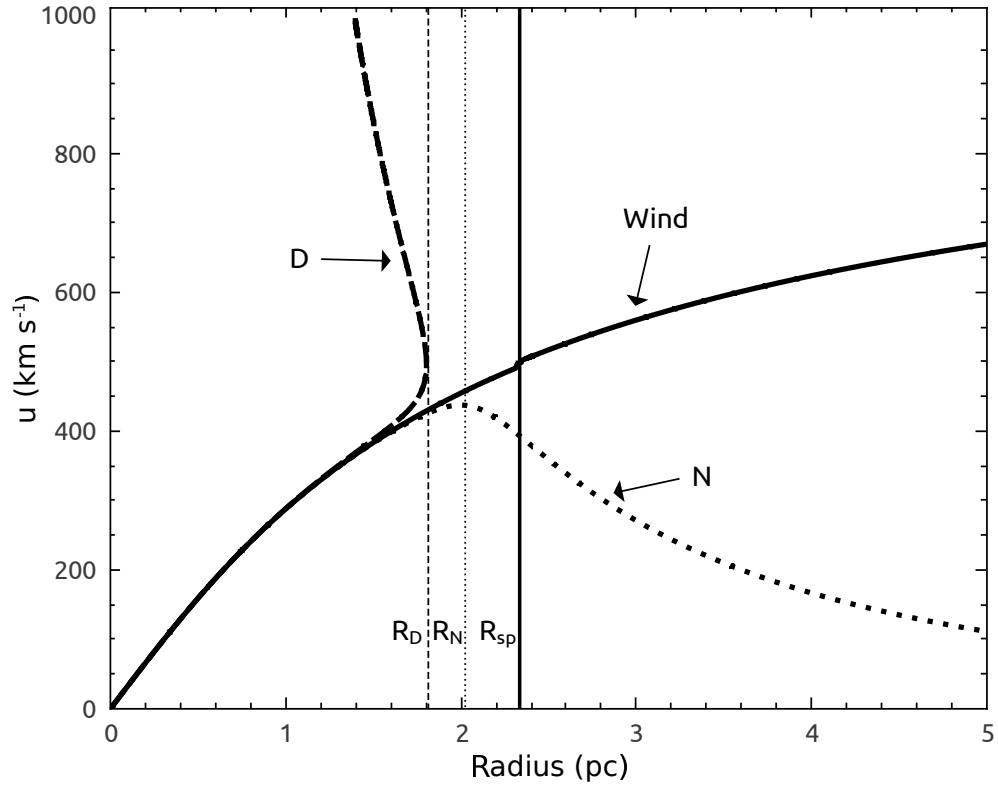
Figure 3.1: Types of integral curves for the differential equation (3.13). The solid line corresponds to the wind solution. The dotted line corresponds to the N-type solution and the dashed line corresponds to the D-type solution. The vertical solid line marks the location of the singular point.

3.4 Integration Procedure

Equations (3.11) and (3.13) have an infinite number of solutions, each one selected by the value of the central temperature. In order to select the proper integral curve from the infinite number of possible solutions it is useful to examine the solution topology:

- The wind solution is the only solution which starts subsonic, goes through the singular point, R_{sp}, where the numerator and the denominator of equation (3.13) change their sign simultaneously, and then reaches supersonic values farther outwards (i.e. the sonic point, R_{son}, coincides with the singular point). Note, that the central temperature which leads to the wind solution must be selected with high accuracy.

- The N-type solution occurs when the central temperature is lower than in the wind solution. In this case, the solution remains subsonic everywhere. The change of sign in equation (3.13) only takes place in the numerator. The outflow velocity reaches its maximum value at a radius R_N from the star cluster center and then decreases with increasing radius from there outwards.

25

- The D-type solution is an unphysical double-valued solution which occurs when the central temperature is greater than that of the wind solution. In this case only the denominator of equation (3.13) changes its sign. In order to obtain this solutions, one has to rewrite equation (3.13), using u instead of r as the independent variable.

As shown in Figure 3.1, the singular point r is located ahead of R_D and R_N. Thus, both R_D and R_N converge to r from the left when the central temperature goes to the correct value. In order to select the central temperature T_0 which corresponds to the wind solution, one can implement an iteration procedure. The procedure is as follows

1. Integrate equations (3.11) and (3.13) using three different trial central temperatures T_1, T_2 and $T_0 = (T_1 + T_2)/2$, with $T_1 < T_0 < T_2$, and search for changes of sign in the numerator, N, and the denominator, D, of equation (3.13). There are now 2 possibilities

   (a) If integrations with the central temperatures T_1 and T_0 change the sign of the numerator and integration with T_2 changes the sign of the denominator, then T_1 must be replaced with T_0.

   (b) If integrations with the central temperatures T_0 and T_2 change the sign of the numerator and integration with T_1 changes the sign of the denominator, then T_2 must be replaced with T_0.

2. Repeat iterations in the halved interval. The iteration process must be continued until the accuracy Δ for locating the singular point is achieved. This accuracy is given by

$$\Delta = \frac{\sqrt{(R_{fit} - R_N)^2 + (R_{fit} - R_D)^2}}{R_{fit}} , \qquad (3.23)$$

   where $R_{fit} = (R_N + R_D)/2$. The accuracy Δ is usually taken within the range $\sim 10^{-4} - 10^{-3}$.

If the singular point does not exist inside the cluster, the transition from a subsonic to a supersonic flow occurs abruptly at $R_{son} = R_{SC}$, where the stellar density changes discontinuously and where the velocity gradient is infinite (CC85, Cantó, Raga, & Rodríguez (2000)). In this case the numerator and denominator of equation (3.13) are both positive when one approaches R_{SC} from the inside, and both negative when one approaches it from the outside.

In order to start the outward integration from the center, one has to take a small step away, ΔR_1, from the star cluster center, and use it as initial conditions:

$$R = \Delta R_1 \tag{3.24}$$

$$u = u_0 + \left.\frac{\mathrm{d}u}{\mathrm{d}r}\right|_0 \Delta R_1 \,, \tag{3.25}$$

$$\rho = q_{m0}^{1/2}\mu_i \left[\frac{V_{A,\infty}^2/2 - c_0^2/(\gamma - 1)}{\Lambda}\right]^{1/2} \,, \tag{3.26}$$

$$P = n_0 k_B T_0 \,. \tag{3.27}$$

The determination of the analytic boundary conditions required to integrate the hydrodynamic equations is given in detail in Appendix B.

In order to start the outward integration from the singular point, one has to take a small step away, ΔR_2, using the following analytic expansions:

$$R = R_{sp} + \Delta R_2 \,, \tag{3.28}$$

$$u = c_{sp} + \left.\frac{\mathrm{d}u}{\mathrm{d}r}\right|_{R_{sp}} \Delta R_2 \,, \tag{3.29}$$

$$\rho = \frac{q_{m0}R_{sp}}{3u_{sp}} F_\beta(R_{sp}) \tag{3.30}$$

$$P = n_{sp}k_B T_{sp} + \left.\frac{\mathrm{d}P}{\mathrm{d}r}\right|_{R_{sp}} \Delta R_2. \tag{3.31}$$

The outward integration from the cut-off radius ($r > R_{SC}$), which make use of equations (3.16 - 3.18), is started with the conditions obtained from the last step of the outward integration from the singular point.

3.5 The Position of the Singular Point

In the case of a stationary wind with no radiative losses ($Q = 0$), the ratio of the energy flux through the surface with radius r,

$$L(r) \equiv 4\pi r^2 \rho u \left(\frac{u^2}{2} + H(r)\right) \,, \tag{3.32}$$

where $H = \frac{\gamma}{\gamma - 1}P/\rho$ is the enthalpy, to the mechanical energy input rate inside the enclosed volume,

$$L_{SC}(r) = \int_0^r 4\pi r^2 q_e \mathrm{d}r = 4\pi r^3 F_\beta(r)/3, \tag{3.33}$$

27

is equal to unity. At the singular point R_{sp}, the wind velocity and the local value of the sound speed coincide, $u_{sp} = c_{sp}$, which together with equations (3.32) and (3.33) and the sound speed definition $c^2 = \gamma P / \rho$ yields (Palouš et al., 2013)

$$3 \rho c^3 (\gamma + 1) = 2 q_{e0} R_{sp} F_\beta(R_{sp}). \tag{3.34}$$

Inserting the mass conservation equation (3.15) into (3.34), and keeping in mind the relation $V_{A\infty}^2 = 2 q_{e0}/q_{m0}$ and that the ratio of specific heats $\gamma = 5/3$, one obtains

$$c_{sp} = \frac{1}{2} V_{A\infty}. \tag{3.35}$$

From the numerator of equation (3.13) evaluated at the singular point, one obtains an algebraic equation for the position of the singular point R_{sp} in the adiabatic case:

$$\left[1 + \left(\frac{R_{sp}}{R_c} \right)^2 \right]^{-\beta} = \frac{4}{3(5\gamma - 3)} F_\beta(R_{sp}). \tag{3.36}$$

The solution of equation (3.36) can be found numerically. It is a function of only one parameter (β). The position of the adiabatic singular point for all clusters with a Schuster stellar density profile is shown in Figure 3.2, where the solution of equation (3.36) is also compared to the position of the singular point obtained by integration of equations (3.13-3.15) in quasi-adiabatic cases. Note that when $\beta \lesssim 1.125$ the ratio R_{sp}/R_c goes to infinity.

Winds driven by SSCs with high mechanical luminosities, small star cluster core radii, low adiabatic wind terminal velocities or high metallicities are strongly affected by radiative cooling. In these cases a rapid decay in temperature occurs just outside the singular point and the singular point moves rapidly towards the star cluster center as one considers more massive clusters, smaller star cluster core radii and lower adiabatic wind terminal velocities.

In this catastrophic cooling regime, one can explore a limiting case in which the loses of energy through radiative cooling equal the energy deposited by the stars: $q_e = Q$. This leads to a simplification on the numerator of equation (3.13) which yields a similar relation as the one in equation (3.36), but for the minimum possible location of the star cluster singular point:

$$\left[1 + \left(\frac{R_{sp}}{R_c} \right)^2 \right]^{-\beta} = \frac{4}{3(\gamma + 1)} F_\beta(R_{sp}). \tag{3.37}$$

This relation can also be solved numerically and compared to the adiabatic position of the singular point (cf. 3.2). For clusters with $\beta \lesssim 0.75$, the ratio R_{sp}/R_c in the strongly radiative cases goes to infinity and the sonic point must coincide with the star cluster surface R_{SC}.

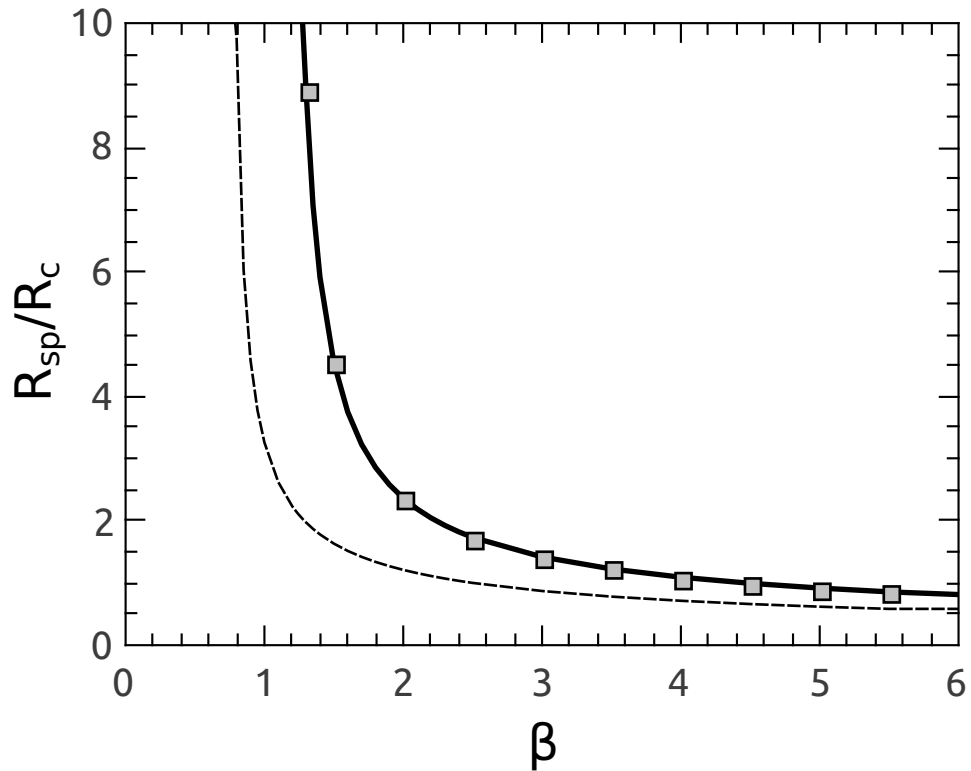Figure 3.2: The ratio R_{sp}/R_c as a function of β in the non-radiative case. The solid line shows the solution of equation (3.36), the solid squares give the position of the singular point in the quasi-adiabatic hydrodynamical calculations. When $\beta \lesssim 1.125$ the ratio R_{sp}/R_c goes to infinity. The dashed curve marks the minimum possible location of the singular point in the strongly radiative regime.

3.6   Summary

In this Chapter, a semi-analytic method was constructed to study the hydrodynamics of stationary spherically-symmetric winds driven by young super star clusters with a Schuster mass distribution. In the next chapters, this method will be employed to evaluate several different models of dustless and dusty star cluster winds and their observational manifestations in the infrared, optical, ultraviolet and X-ray regimes.

Chapter 4

Star Cluster Winds

In this chapter, the hydrodynamic scheme developed in Chapter 3 is applied to models which accounts for gas and dust cooling. In these models, a Schuster stellar density distribution with index $\beta = 1.5$ was used because it appears as an asymptotic case to King's surface formula (King, 1962) when projected onto the sky (Ninkovic, 1998).

This chapter is organized as follows: in Section 4.1 four models with different star cluster parameters and dust contents are presented. The hydrodynamic implications of the presence of dust grains in the intracluster medium are discussed. In Section 4.3, the model is applied to the high-velocity absorption line component in the spectra of the blue compact dwarf galaxy *PHL 293B*.

4.1 Dustless vs. Dusty Star Cluster Winds

Consider the case of young and massive star clusters in which massive stars follow a generalized Schuster stellar density distribution (see equation (3.1)). To investigate the impact that different stellar distributions provide on the star cluster wind hydrodynamic behavior, four cases (models *I*, *II*, *III* and *IV*) are investigated for different values of β in equation (3.1). The input parameters in these models are: L_{SC}, $V_{A\infty}$, R_c, R_{SC}, a_{min}, a_{max} and Z_d (cf. Table 4.1). The dusty models presented in this Chapter do not follow the evolution of the dust size distribution due the thermal sputtering or the exit of dust grains from the star cluster as part of a wind. Hence, the value of Z_d does not change and the assumed dust size distribution is that proposed by Mathis et al. (1977) ($\sim a^{-3.5}$, cf. Chapter 2).

All these models are located in the quasi-adiabatic regime (i.e. radiative losses are negligible compared to the energy supplied by massive stars and SNe and the transition from subsonic to the supersonic regime occurs either at the star cluster radius or at the quasi-adiabatic singular point (see equation 3.36)).

The distributions of velocity, temperature and density, for models *I - IV* are shown in the left panels (a, b and c) of Figure 4.1. The solid, dotted, dashed and dash-dotted lines correspond to models *I*, *II*, *III* and *IV*. In all cases, the flow velocity near the

31

Table 4.1: Reference models

Models	β	R_c (pc)	R_{SC} (pc)	R_{HM} (pc)	R_{son}	L_{SC} (erg s^{-1})	$V_{A\infty}$ (km s^{-1})
I	0	–	3.36	2.67	3.36	3×10^{40}	1000
II	1	1	4.14	2.67	4.14	3×10^{40}	1000
III	1.5	1	5.59	2.67	5.34	3×10^{40}	1000
IV	2	1	∞	2.67	2.78	3×10^{40}	1000

center grows almost linearly with radius, passes the singular point at about its quasi-adiabatic position, and then rapidly approaches the terminal speed value. In models *I* and *II*, the transition to the supersonic regime occurs abruptly at the star cluster surface and the temperature and density decrease sharply at the cluster edge. In models *III* and *IV*, the sonic point is located inside the star cluster (coinciding with the quasi-adiabatic singular point) and the transition from subsonic to the supersonic regime is much more gradual and smooth.

Models *I*, *II*, *III* and *IV*, are also run with full account of dust cooling (see the right-hand panels in Figure 4.1) to illustrate the roll of dust grains of the hydrodynamics on the matter reinserted within super star clusters.

In these calculations, the lower and upper limits of the MRN dust size distribution are $a_{min} = 0.001$ μm and $a_{max} = 0.5$ μm, respectively. The effect of dust cooling is noticeable in all these models as the terminal speed is much lower than in the dust-free cases (cf. panel a *vs.* panel d in Figure 4.1); also the wind temperature radial profiles decay more steeply in the dusty cases than in the dust-free cases (cf. panel b *vs.* panel e in Figure 4.1). The density radial profiles in the dust-free and dusty cases exhibit very similar behaviors with the densities in the latter case being slightly higher (cf. panel c *vs.* panel f in Figure 4.1).

4.2 The Critical Line

As one considers more massive and compact star clusters and with increased dust-to-gas ratios, radiative cooling is strongly enhanced (as the cooling rate scales with the square of density). In these cases, the radial temperature profile is radically different from the predictions of the quasi-adiabatic cases, and a rapid decay in temperature (to $\sim 10^4$ K which is the minimum temperature allowed in the models) occurs close to the sonic point. This scenario is known as the catastrophic cooling regime. Consequently, the singular/sonic point leaves its quasi-adiabatic position and moves rapidly towards the star cluster center.

For a given combination of cluster parameters β, R_c and R_{SC}, there is a critical luminosity, L_{crit}, separating the region of stationary winds from the region where thermal instabilities occur within the cluster volume what leads to clump formation and to non-
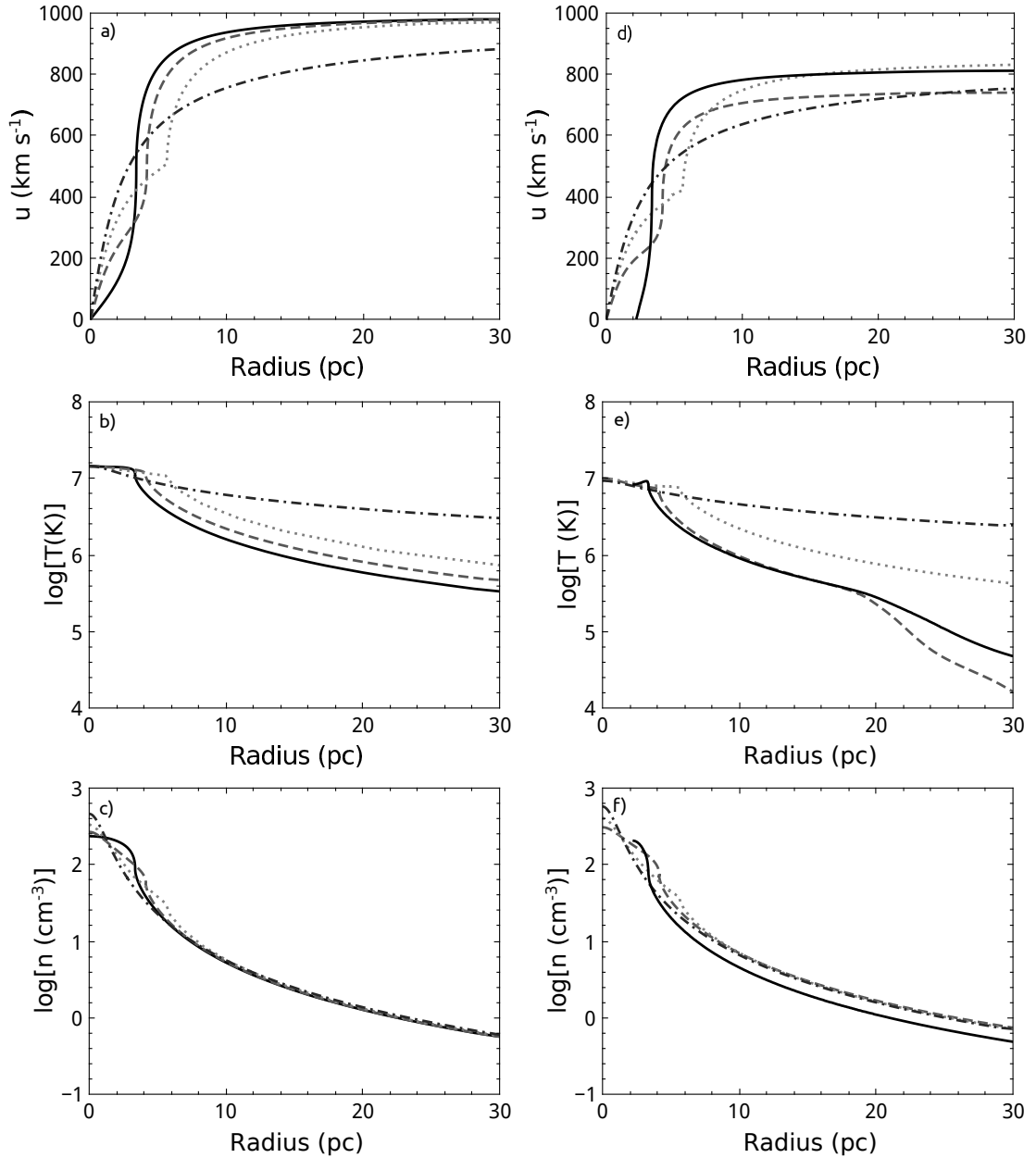
32

Figure 4.1: Stationary dust-free and dusty wind solutions. Left-panels a, b and c present the wind velocity, temperature and density for (dust-free) models *I-IV*, respectively. Right panels d, e and f, depict the runs of the hydrodynamic variables for models with the same input parameters as models *I-IV*, but including radiative cooling via gas-grain collisions for an equal mix of silicate and graphite and MRN dust size distributions with $a_{min} = 0.001$ μm and $a_{max} = 0.5$ μm. Solid, dashed, dotted and dash-dotted lines correspond to the calculations for models *I*, *II*, *III* and *IV*, respectively.

stationary outflows. In this scenario, one can distinguish two situations:

a) Clusters with $\beta > 1.125$, and compact clusters where the sonic point accommodates at R_{SC}. For these clusters the criterion discussed in Tenorio-Tagle et al. (2007) for the homogeneous case, was used. i.e. the transition to the thermally unstable solutions occurs soon after the central temperature, T_0^{max} (cf. 3.22), drops to the value which corresponds to the maximum of the central pressure. This temperature is irrespective of the values of β, R_c and R_{SC} and depends only on $V_{A\infty}$ and Λ. T_0^{max} can be calculated by solving the equation:

$$1 - \frac{q_{m0}\mu_a T_0^{max}}{2\mu_i n_0^2 \Lambda} \left[\frac{c_0^2}{(\gamma - 1)T_0^{max}} + \frac{n_0^2}{q_{m0}} \frac{\mathrm{d}\Lambda}{\mathrm{d}T_0^{max}} \right] = 0, \tag{4.1}$$

which is equivalent to equation (7) of Silich et al. (2009) with the heating efficiency, $\eta = 1$.

All these cases have in common the fact that R_{sp} remains at its adiabatic position. For example, the dusty model *I* has already surpassed the value of L_{crit}, in which case the stagnation radius (R_{st}, the radius when the wind velocity is zero) is detached from the star cluster center. Thus the flow undergo a bimodal behavior in which the central and densest zone ($r < R_{st}$) cools rapidly and accumulates the reinserted matter, in the outer zone ($R_{st} > r$), the flow is still stationary. In these case, the integration constant in equation (3.10) is not zero but $C = -1/3q_{m0}R_{st}^3$ and the mass conservation equation (3.15) becomes (Tenorio-Tagle et al., 2007):

$$\rho = \frac{q_{m0}r}{3u} F_\beta(r) \left[1 - \left(\frac{R_{st}}{R_{SC}} \right)^3 \right]. \tag{4.2}$$

b) Clusters with $\beta \leq 1.125$ except those in which the sonic point does not coincide with R_{SC}. In these cases, strong radiative cooling forces R_{sp} to detach from its adiabatic position, moving towards the center as one considers more massive clusters. Thus, the run of the hydrodynamical variables changes qualitatively, promoting the fall of temperature to 10^4 K closer and closer to R_{SC}. Therefore, L_{crit} is defined as the value for which the gas temperature falls to 10^4 K exactly at the sonic point and thermal instabilities set in. The two semi-analytical criteria have been combined to define a unique semi-analytical curve for L_{crit}.

Figure 4.2, shows the region of stationary and the region of thermally unstable solutions separated in the mechanical energy (or cluster mass) *vs* the star cluster size diagram by L_{crit} (both values normalized by R_c) for different values of β. In the left panel, L_{crit}/R_c for the dustless cases is shown, while in the right panel, L_{crit}/R_c is shown for dusty winds with $a_{min} = 0.001$ μm and $a_{max} = 0.5$ μm. As an example, a dustless star cluster with $\beta = 1.5$. $R_c = 1$ pc and $R_{SC} = 10$ pc, will enter the thermally unstable regime at $L_{crit} \sim 6.76 \times 10^{41}$ erg s^{-1} (which corresponds to a $\sim 2.25 \times 10^7$ M$_\odot$ star cluster). The same cluster with a dust-to gas mass ratio equal to 10^{-3}, would become bimodal for $L_{crit} \sim 5.36 \times 10^{40}$ erg s^{-1} ($\sim 1.78 \times 10^6$ M$_\odot$), a difference of 1.1 dex.

34

This difference could be enhanced to even larger values considering larger dust-to-gas mass ratios. A similar effect would occur if one considers a dust size distribution which gives more weight to small grains because they have smaller heat capacities and thus are more easily heated making them more effective coolants. Note that dust cooling scales as $\sim a^{-1/2}$ (cf. equation 2.9, 2.10 and 2.11).
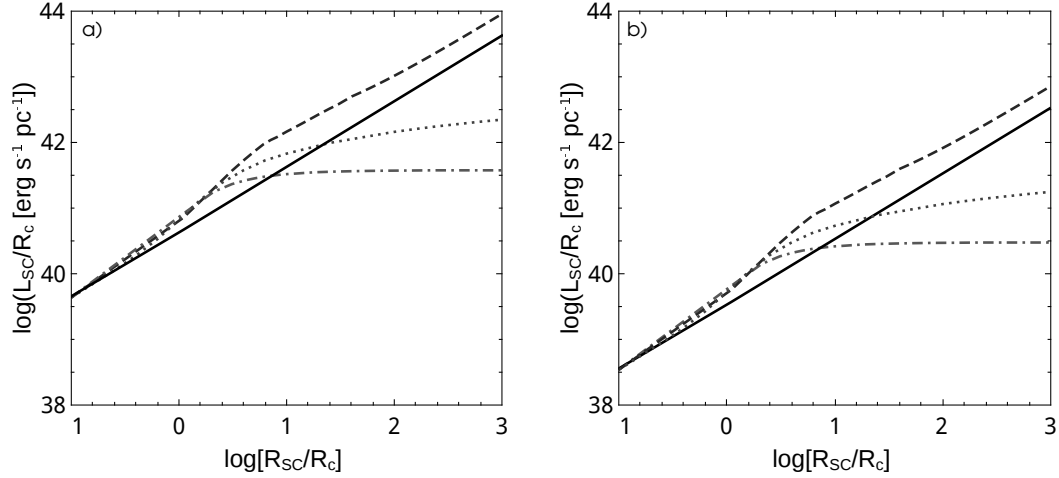

Figure 4.2: L_{crit}/R_c as a function of R_{SC}/R_c for dust-free models (left panel) and dusty models with $Z_d = 10^{-3}$, $a_{min} = 0.001$ μm and $a_{max} = 0.5$ μm (right panel) for $\beta = 0$ (solid lines), $\beta = 1$ (dashed lines), $\beta = 1.5$ (dotted lines) and $\beta = 2$ (dash - dotted lines).

The fraction of the star cluster mechanical luminosity carried out by the wind decreases with decreasing mechanical luminosities as, progressively, a larger fraction of the deposited energy is radiated away. Figure 4.3 shows the flux of energy (cf. equation 3.32) through a sphere of radius 100 pc as a function of the star cluster mechanical luminosity L_{SC} for the dustless and dusty models (left and right panels, respectively). One can observe an analogous behavior in both cases with the dusty cases displaced to lower values of L_{SC} by an order of magnitude. The right most points on the curves mark the largest mechanical luminosity for which a stationary wind solution exists. The largest loss of energy in stationary winds occurs for models *II* and *III* with $\beta = 1$ and $\beta = 1.5$, respectively.

In the case of thermally unstable solutions, the pressure in the flow is diminished, in particular in the central and densest region, inhibiting the exit of the reinserted matter which would be forced to accumulate and lead to clump formation and eventually to secondary stellar generations. In the dustless case, this assertion was confirmed by one-dimensional simulations carried out by F. Hueyotl-Zahuantitla, which demonstrated to be in excellent agreement with the semi-analytic calculations described here (cf. Palouš, Wünsch, Martínez-González, Hueyotl-Zahuantitla, Silich, & Tenorio-Tagle, 2013).
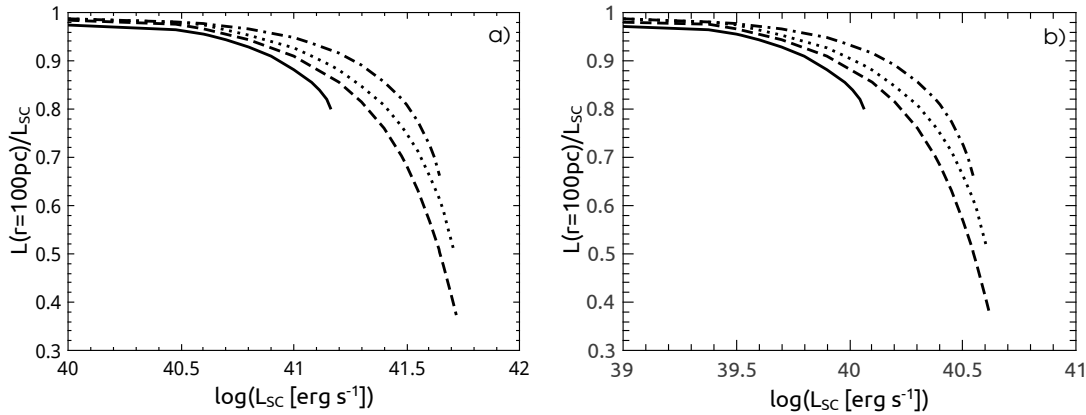
Figure 4.3: The fraction of inserted energy retained by stationary winds as a function of the star cluster luminosity, for β = 0, 1, 1.5 and 2. (solid, dashed, dotted and dash-dotted lines, respectively). The left panel a corresponds to dustless models while the right panel b illustrates dusty models.

4.3 Application to Observations: the case of PHL 293B

Winds driven by stellar clusters where the mechanical luminosity is close to the critical line, experience a rapid decay in temperature near the singular/sonic point (which may coincide with the edge of the cluster). Such clusters do not present an extended X-ray region but instead a recombining region and, given the ample supply of UV photons, a stationary re-ionized region, rapidly expanding close to the sonic point.

PHL 293B is a blue compact dwarf galaxy (with an ionized radius ~ 0.4 kpc) first observed by Haro & Luyten (1962). The analysis of observational data for the past quarter of century has shown no significant changes on the intensities and the shift of the lines in this galaxy; this implies that they are not associated to a transient phenomena but instead that they are formed in the stationary cluster wind. The Balmer line luminosity and its equivalent widths manifest that *PHL 293B* hosts at its center, a young ($\sim 5 - 7$ Myr) and massive ($\sim$ a few times 10^5 M$_\odot$) star cluster with a diameter ~ 5 pc. The optical spectra of the star cluster shows strong emission in narrow lines with low-intensity broad wings and weak narrow absorptions features in the hydrogen recombination lines and FeII multiplet 42, which appear blue-shifted by about 800 km s^{-1} with respect to the narrow emission.

Here it is suggested that the components are formed in different regions of the host galaxy as it is shown in the right-hand panel in Figure 4.4. This figure displays the emission and absorption components required to match the HII spectra of *PHL 293B* (see Figure 2 of Terlevich et al. 2014 or Figure 3 of Izotov et al. 2011), together with a sketch showing the structure of the galaxy and of its ionizing cluster, according to the present interpretation, as well as the observers location. Various regions in the galaxy sketch and in the composed spectra are labeled (from HII and B-D) to indicate their proposed correspondence. In this way, the narrow emission line component, centered at

the redshift of the galaxy and showing its low metal abundance, results from the general ionization of the galaxy ISM (region HII). The narrow absorption line components are due to a fast (~ 800 km s^{-1}) strongly radiative cluster wind (region B) and the broadest components arise from rapidly evolving remnants cause by the off-centered explosion of the most recent type II supernovae (regions C and D). Then the hydrodynamic model of dusty star cluster winds was applied to region B while further discussion on regions C, D and HII can be found in Tenorio-Tagle et al. (2015).

To asses this task, several hydrodynamic calculations were performed assuming that massive stars follow a generalized Schuster stellar density distribution $\rho_* \propto [1 + (r/R_c)^2]^{-\beta}$ with $\beta = 1.5$. For the calculations were considered clusters close to L_{crit} what leads, as mentioned in Section 4.2, to strongly radiative winds and thus to the recombination of the stationary flow close to the cluster surface. In all cases the cluster half-mass radius, R_{HM}, and the cluster core radius, R_c, were fixed and then the corresponding cut-off radius, R_{SC}, was calculated.
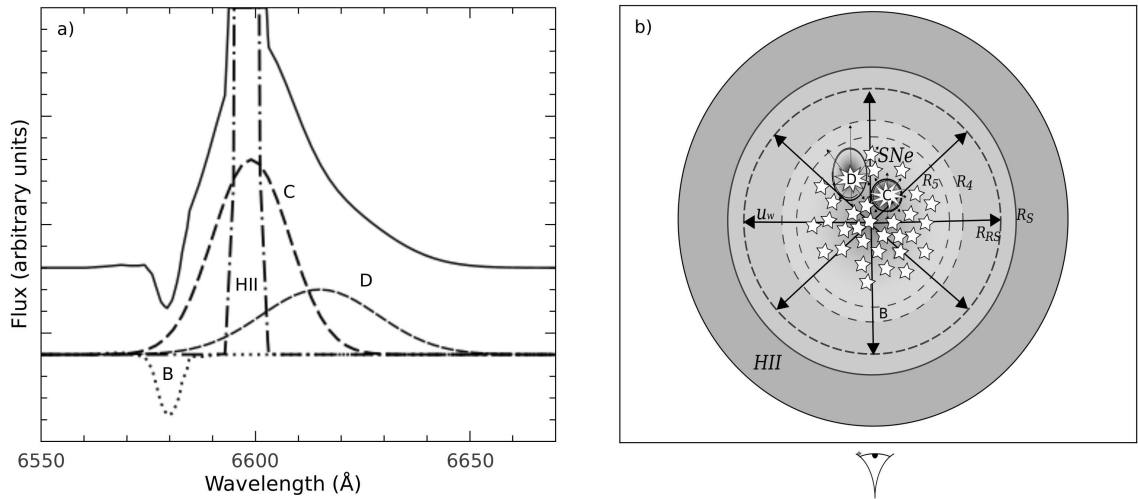

Figure 4.4: The structure of *PHL 293B*. Panel a) shows the emission and absorption line components that lead to the typical ionized H spectra in *PHL 293B* (solid line). The narrow line, well centered at the galaxy redshift, is associated to region HII in panel b). The narrow absorption line blueshifted by some 800 km s^{-1} is here associated to region B and the two broad red-shifted components correspond to two SN remnants evolving on the far side of the cluster environment. Panel b) displays the proposed structure of the galaxy and its ionizing cluster (note scales greatly distorted). Indicated are: the central ionizing cluster that contains two rapidly evolving SN remnants (regions C and D in both panels). The high velocity cluster wind (large arrows) impacting the galaxy ISM (region HII in both panels) and thus supporting a leading shock at a radius R_S and a reverse shock at a radius R_{RS}. Indicated also is region B, the shell at which the stationary cluster wind reaches temperatures of 10^5 K and 10^4 K (R_5 and R_4, respectively) and thus is able to recombine, as well as the observer's location.

Star clusters with typical mechanical luminosity $L_{SC} = (0.7 - 1) \times 10^{40}$ erg s^{-1} were considered. Table 4.2 summarizes the input parameters for models PHL1, PHL2, PHL3

37

and PHL4. Models PHL1-PHL3 are applicable once supernovae begin to explode within the cluster volume ($\sim$ 3 Myr of evolution) and a continuous presence of dust within the reinserted matter is established. In models PHL1-PHL3, the dust to gas mass ratio, Z_d, was set to 10^{-3}, and the same dust properties described in Table 2.1 were taken into account except that models PHL1 and PHL2 consider dust grains with a fixed size of 0.1 and 0.05 μm, respectively. Model PHL3 considers a dust size distribution with $a_{min} = 0.001$ μm and $a_{max} = 0.5$ μm. For the sake of comparison, a model (PHL4) with the same input parameters as model PHL3, but without dust radiative cooling, was explored. Figure 4.5, shows the results from the hydrodynamical calculations

Table 4.2: Input Parameters

Models	β	R_{HM} (pc)	R_c (pc)	R_{SC} (pc)	L_{SC} (erg s^{-1})	$V_{A\infty}$ (km s^{-1})	Z_d	a_{min} μm	a_{max} μm
PHL1	1.5	1	1	1.46	1×10^{40}	1000	10^{-3}	0.1	0.1
PHL2	1.5	1	1	1.46	7×10^{39}	1000	10^{-3}	0.05	0.05
PHL3	1.5	1	1	1.46	8×10^{39}	1000	10^{-3}	0.001	0.5
PHL4	1.5	1	1	1.46	8×10^{39}	1000	0	0	0

for models PHL1-PHL4. The dusty models PHL1-PHL3, were selected, among other models, because their stationary wind terminal velocity, V_∞, reaches a value $\sim$ 800 km s^{-1} and further because strong radiative cooling brings the wind temperature down to the range $T \sim 10^5 - 10^4$ K, what allows for H recombination, at a short distance from the star cluster surface. The selected models exhibit very similar hydrodynamic radial profiles; they all have central wind densities $\sim 10^3$ cm^{-3} and temperature $\sim 10^7$ K (see Figure 4.5). Therefore, the central hot zone is transparent to the ionizing radiation. However, outside of the cluster, the density decays to values of a few (cm^{-3}) when the wind temperature drops to $\sim 10^5$ K at $r = R_5$ between 10 pc and 15 pc, and then goes to ~ 1 cm^{-3} when the cluster wind temperature reaches 10^4 K, at a distance $R_4 \sim 25$ pc. It is within this temperature range that hydrogen recombination takes place and the free wind is no longer transparent to the ionizing radiation.

The distributions of density, temperature and velocity presented in Figure 4.5 are used to calculate the outward flux of ionizing photons (cm^{-2} s^{-1}) $J = N_{UV}(r)/4\pi r^2$ and the degree of ionization $x = n_i/(n_i + n_n)$, where n_i and n_n are the ionized and neutral gas number densities, in the free wind region. The transport of ionizing radiation and the ionization balance equations (Goldsworthy, 1958) are then reduced to:

$$\frac{\mathrm{d}J}{\mathrm{d}r} = -\frac{2J}{r} - (1-x)J\frac{\sigma_a \rho}{\mu}, \tag{4.3}$$

$$\frac{\mathrm{d}x}{\mathrm{d}r} = (1-x)\frac{\sigma_a J}{u} - \frac{\beta \rho}{\mu u}x^2, \tag{4.4}$$

where $\sigma_a = 6 \times 10^{-18}$ cm^2 and $\beta = 3 \times 10^{-10}T^{-3/4}$ cm^3 s^{-1} are the H absorption cross section for ionizing radiation and the recombination coefficient to all but the ground
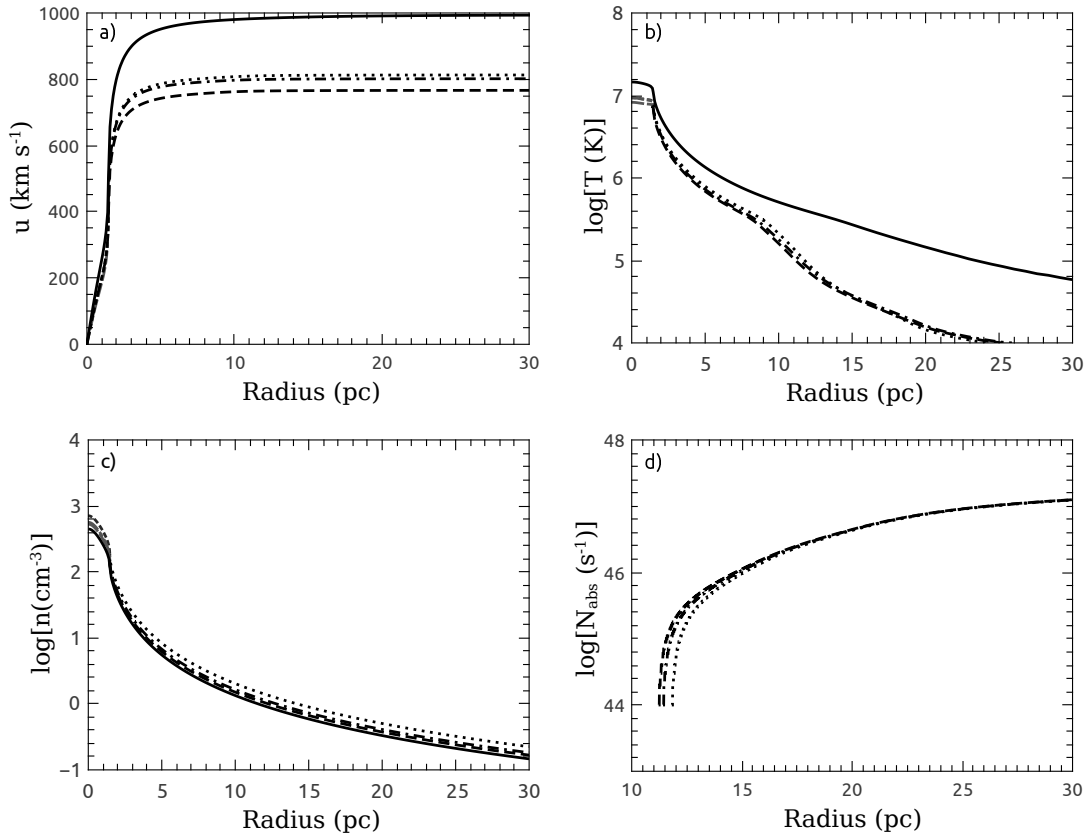
Figure 4.5: The distribution of the hydrodynamical variables in the free-wind region. Panels a, b, c and d present the wind velocity, temperature, density as a function of distance to the star cluster center, respectively, and the number of ionizing photons absorbed per unit time inside a volume of radius r The dotted, dashed, dash-dotted and solid lines display the results of the calculations for models PHL1, PHL2, PHL3 and PHL4, respectively.

level, respectively, μ is the mean mass per particle. These equations were solved numerically assuming that the ionizing radiation is not depleted in the hot wind region until the temperature drops to 10^5 K (at R_5) and thus that the degree of ionization and the total ionizing photon flux are kept $x = 1$ and $N_{UV} = 2.71 \times 10^{51}$ s^{-1}, up to this radius.

In all these models (PHL1-PHL4) the degree of ionization x is close but not equal to unity. Note also that the number of ionizing photons is large and the wind density has a moderate value when the wind temperature reaches about 10^5 K and recombination to all energy levels becomes significant. Consequently, in cases PHL1-PHL3 the number of neutral atoms which absorb the ionizing radiation at any time t is not negligible. To sustain the value of $x \sim 1$, some $10^{46} - 10^{47}$ ionizing photons s^{-1} are depleted from the radiation field to balance recombination within the volume enclosed between R_5 and R_4 (see the last panel of Figure 4.5).

Further out, the density continues to fall in all cases, inhibiting recombination in the outer wind region and thus the number of depleted ionizing photons s^{-1} reaches an asymptotic value (see panel d in Figure 4.5). It is within this region ($R_5 - R_4$) that radiation from the non-ionizing stellar continuum, blueshifted from the emission line centers by 800 km s^{-1}, finds the neutral atoms at different energy levels what produces the weak absorption lines seen in the spectra of *PHL 293B*.

In the dustless case PHL4, the temperature drops to 10^5 K at a a larger distance from the star cluster center ($R_5 \approx 23.5$ pc). By then the wind density has fallen to 0.23 cm^{-3}, sufficiently as to inhibit recombination.

One can also calculate the photoionized ($N(HII)$) and neutral ($N(HI)$) hydrogen column densities assuming that the degree of ionization x is close to unity in the whole free wind region: $N(HII) = \int_{R_5}^{\infty} n_5 (R_5/r)^2 dr \approx n_5 R_5$ and $N(HI) = \int_{R_5}^{\infty} n_5 (1 - x)(R_5/r)^2 \mathrm{d}r$, where n_5 is the wind number density at the radius R_5. In the models with dust cooling the calculated values of $N(HII)$ are 9.27×10^{19} cm^{-2}, 7.64×10^{19} cm^{-2} and 7.97×10^{19} cm^{-2}, for models PHL1, PHL2 and PHL3, respectively. These values are in good agreement with the estimate $(1 - 2) \times 10^{20}$ cm^{-2} by Terlevich et al. (2014). The values of the neutral hydrogen column densities are 1.10×10^{13} cm^{-2}, 1.11×10^{13} cm^{-2}, and 8.8×10^{12} cm^{-2}, for models PHL1, PHL2 and PHL3, respectively, which are also in good agreement with the observational estimates in the range 10^{13} cm^{-2} - 10^{14} cm^{-2} derived from the equivalent width of the Balmer lines by Terlevich et al. (2014).

One can compare now these results with the dustless model PHL4, which exhibits a quasi-adiabatic behavior, to note that despite the similar density and velocity distributions, model PHL4 does not present the drastic temperature fall at a short distance from the star cluster center and therefore it would not lead to the high velocity blueshifted absorption features predicted in models PHL1-PHL3.

Finally, one can use the calculated model profiles to estimate the expected diffuse X-ray

emission:

$$L_X = 4\pi \int_0^{R_{out}} r^2 n_e n_i \Lambda_X(T, Z) \mathrm{d}r, \tag{4.5}$$

where $n_e(r)$ and $n_i(r)$ are the electron and ion number densities, $\Lambda_X(T, Z)$ is the X-ray emissivity used by Strickland & Stevens (2000) and R_{out} marks the X-ray cut-off radius (the radius where the temperature in the wind drops below $T_{cut} \approx 5 \times 10^5$ K).

In all the models PHL1-PHL4, the 0.3 keV - 2.0 keV diffuse luminosity ($L_X = 3.8 \times 10^{39}$ erg s^{-1}, 2.24×10^{38} erg s^{-1}, 2.46×10^{39} erg s^{-1} and 1.15×10^{38} erg s^{-1}, respectively) are in a good agreement with the observed upper limit of $\sim 2.2 \times 10^{38}$ erg s^{-1} (Terlevich et al., 2014).

A hot dusty plasma radiates mainly in the X-ray and IR regimes. Thus one can obtain the upper limit for the IR luminosity expected in cases PHL1, PHL2 and PHL3 if one compares the star cluster mechanical luminosity L_{SC} with the energy flux through a sphere of radius $r = R_{out}$ at which the X-ray emission vanishes and assume that all energy lost within this volume is radiated away either in the IR or in the X-ray regime:

$$L_{IR} \approx L_{SC} - L_X - 4\pi \rho u R_{out}^2 \left(\frac{u^2}{2} + \frac{\gamma}{\gamma - 1} \frac{p}{\rho} \right), \tag{4.6}$$

where all hydrodynamical variables (the density ρ, velocity u and the value of thermal pressure P) are calculated at $r = R_{out}$. This leads to IR luminosities $L_{IR} = 2.9 \times 10^{39}$ erg s^{-1}, 2.6×10^{39} erg s^{-1} and 2.5×10^{39} erg s^{-1} in cases PHL1, PHL2 and PHL3, respectively. The dusty wind models thus lead to IR luminosities which exceed the cluster wind diffuse X-ray emission by about an order of magnitude ($L_{IR}/L_X = 7.65$, 11.6 and 10.3 in models PHL1, PHL2 and PHL3, respectively). In model PHL4 the hot wind cools mainly through X-ray radiation. L_X presents $\sim 87\%$ of the total radiated energy in this case.

4.4 Summary

Several dusty wind models have been run in order to quantify the effects that the stellar distribution, as well as the dust cooling law, have on the hydrodynamics of the matter reinserted within young and massive star clusters. In this scenario, it has been shown that such clusters, deposit into the ISM only a fraction of their mechanical energy (as predicted by synthesis models as Starburst99 Leitherer et al. 1999) and the wind terminal speed is strongly diminished. Additionally, the model predicts a drastic fall of temperature to a value 10^4 K at significantly smaller radii than from dustless models. Thus, the dust cooling law, effectively lowers the location of the critical line which separates clusters with stationary outflows from those thermally unstable which tend to mass accumulation (bimodal solution) and, presumably, lead to create secondary stellar generations. The new location of the critical line implies that young, massive and compact SSCs with masses $M_{SC} > 10^5 - 10^6$ M$_\odot$ can experience the bimodal solution.

The calculations also show that powerful dusty winds are able to produce stationary high velocity blue-shifted absorption features similar to those observed in the optical spectra of the central cluster of *PHL 293B*. The dusty wind model with strong radiative cooling also predicts the neutral and ionized gas column densities and the diffuse X-ray emission in good agreement with the observed values.

The results obtained in this Chapter are published as part of the papers Palouš et al. (2013); Tenorio-Tagle et al. (2013, 2015).

Chapter 5

Infrared Manifestations

In this chapter, stochastic dust injection, heating and cooling processes (cf. Section 2.2) are combined with the hydrodynamical calculations described in Chapters 3 and 4 to propose several scenarios of dust emission and its influence on the spectral energy distributions from the hot interiors of super star clusters. Under these considerations, super star clusters become ideal laboratories to study the evolution of dust immersed into a hot plasma. Here the stochastic injection of dust by supernovae is addressed following the evolution of the resultant grain size distribution due to thermal sputtering within the hot and dense plasma generated by young stellar clusters. Dust grains are heated by means of random collisions with gas particles which results on the appearance of infrared spectral signatures. Time-dependent infrared spectral energy distributions, which are to be expected from young stellar clusters, are presented. The results are based on hydrodynamic calculations that account for the stochastic injection of dust by supernovae. These also consider gas and dust radiative cooling, stochastic dust temperature fluctuations, the exit of dust grains out of the cluster volume due to the cluster wind and a time-dependent grain size distribution (cf. Chapter 2).

This chapter is organized as follows: In Section 5.2, the hydrodynamic results together with the physics of stochastic dust heating and cooling are employed to obtain the expected spectral energy distributions of young stellar clusters. In Section 5.3 the main results and conclusions are outlined.

5.1 Hydrodynamic Models with Dust Stochastic Temperature Fluctuations

Similarly to the treatment in the previous Chapters, here young and massive star clusters with a Schuster stellar density distribution with index $\beta = 1.5$ are considered. From the family of the Schuster distributions, this case provides the best fit to the empirical mass distribution in young star clusters (Veltmann, 1979). Supernovae are considered to inject dust uniformly throughout the star cluster with a standard Mathis et al. (1977) grain size distribution. Right after injection, the dust size distribution will evolve due

to the action of thermal sputtering and the exit of dust grains from the star cluster as part of the star cluster wind (cf. Section 2.1).

The values of $M_{dSN}^{(m)}$, the total dust mass injected by a single supernova, and $\Delta\tau_{SN} = \tau_{SN}^{(m+1)} - \tau_{SN}^{(m)}$, the interval between supernova events (cf. Equations (2.2) and (2.5) in Section 2.1), were selected pseudo-randomly from a Gaussian distribution (except for the first supernova, in which $M_{dSN}^{(m)}$ was chosen so that $Z_d = 10^{-3}$ at τ_{inj}). The mean value for $M_{dSN}^{(m)}$ was set to 0.5 M$_\odot$ with a standard deviation 0.15 M$_\odot$. The mean interval between supernova explosions (~ 17000 yr for a 10^5 M$_\odot$ cluster, see Figure 2.1) was obtained from the supernova rate of Starburst99 synthesis model (Leitherer et al., 1999) with a standard Kroupa initial mass function with lower and upper cut-off masses 0.1 M$_\odot$ and 100 M$_\odot$, respectively. The standard deviation for $\Delta\tau_{SN}$ was taken to be 10% of the mean value.

The prevailing conditions inside the star cluster volume (i.e. average values for the gas number density, n, and temperature, T) are calculated by making use of the hydrodynamical model discussed in Chapters 3 and 4. Once these conditions are known, one can apply Dwek (1986) prescriptions to calculate the dust temperature distribution, $G(a, T_d)$ (see Equation (2.24) in Section 2.3), resulting from stochastic temperature fluctuations.

All the models presented in this Chapter are quasi-adiabatic, however, they include the effects of gas (Raymond et al., 1976) and dust radiative cooling (Dwek, 1987) (cf. Section 2.2 for the complete description of the dust cooling calculation).

The infrared flux per unit wavelength, produced by a population of dust grains with the same chemical composition, from a star cluster located at distance D_{SC}, can then be calculated as (Dwek & Arendt, 1992):

$$f_\lambda = \left(\frac{1.4 m_H Z_d N_H}{\rho_d} \right) \pi \Omega_{SC} \int_{a_{min}}^{a_{max}} \int_0^\infty a^2 \frac{\partial n_i}{\partial a} Q_{abs}(\lambda, a) B_\lambda(T_d) G(a, T_d) \mathrm{d}T_d \mathrm{d}a, \tag{5.1}$$

in units erg s^{-1} cm^{-2} Å^{-1}, or alternatively, in units erg s^{-1} cm^{-2} Hz^{-1} or Jansky, if one is interested in the flux per unit frequency, f_ν, where $\lambda f_\lambda = \nu f_\nu$. Since both quantities, f_λ and f_ν, are widely used by different authors (e.g. Adamo et al., 2010b; Fisher et al., 2014; Izotov et al., 2014; Reines et al., 2008), figures 5.1-5.5 present them both, taking into account the contribution from graphite and silicate grains. In the above equation, N_H is the hydrogen column density through the star cluster volume ($= 4/3 n R_{SC}$), a is the dust grain radius, $\rho_d = 4/3 \pi \rho_{gr} \int_{a_{min}}^{a_{max}} a^3 \frac{\partial n_i}{\partial a}\, \mathrm{d}a$ is the size-averaged dust density, and $\Omega_{SC} = \pi (R_{SC}/D_{SC})^2$, is the solid angle subtended by the star cluster. Additionally, T_d is the dust temperature, $Q_{abs}(\lambda, a)$ is the dust absorption efficiency and $B_\lambda(T_d)$ is the Planck function in terms of the wavelength, λ. In these models the distance to the star cluster was set as $D_{SC} = 10$ Mpc. A complete discussion of the stochastic dust temperature fluctuations is presented in Appendix C.

In all these calculations, the charge of dust grains was neglected (Smith et al., 1996) as well as the contribution to the infrared flux from dust grains outside the star cluster volume. This treatment is also not dealing with possible effects related to the absorption of ionizing photons by dust grains which could be important as long as the ionizing flux from the star cluster is strong. However, coeval clusters suffer a substantial reduction of their ionizing photon flux as soon as they enter the SN era. The number of emitted UV photons falls with time, as t^{-5} (Beltrametti et al., 1982) and thus after $5-6$ Myr the number of UV photons is almost two orders of magnitude smaller than at the start of the evolution. This fall in the ionizing flux reduces the time during which the UV radiation may be more important than gas-dust collisions which, on the other hand, could be important during all the type II SN era (from ~ 3 to 40 Myr). The hydrodynamical model assumes that dust grains move with the same velocity as the injected gas and thus the effects of kinetic sputtering in the intracluster medium have not been considered.

5.2 Infrared Spectral Energy Distributions

To assess the impact that collisional heating of dust grains have on the expected infrared spectral energy distributions from young and massive dusty star clusters, several models have been run with the input parameters described in the previous section (L_{SC}, $V_{A\infty}$, R_c, R_{SC}, a_{min}, a_{max} and t). The reference model *A*, consists of a star cluster with a total mass of 10^5 M$_\odot$ (which corresponds to a mechanical luminosity 3×10^{39} erg s^{-1}), $R_{hm} = 3.92$ pc (obtained from values $R_c = 4$ pc and $R_{SC} = 5$ pc), an adiabatic wind terminal speed $V_{A\infty} = 1000$ km s^{-1}, lower and upper limits for the injected dust size distribution, $a_{min} = 0.001\mu$m and $a_{max} = 0.5\mu$m, respectively; and an equal mixture of graphite and silicate grains. The other models vary one or more of the input parameters with respect to model *A*. Models *B-C* explore different values of the mechanical luminosity, models *D* and *E* vary the adiabatic wind terminal speed and models *F* and *G* differ in the compactness of the star cluster. The reference model *A*, as well as models *B-G* are evaluated at the end of the first injection event ($t = 1000$ yr) where, as pointed out before, $M_{dSN}^{(1)}$ is set to allow $Z_d(\tau_{inj})$ to be equal to 10^{-3}. Models *A1-A4* are evaluated at later times. Table 5.1 presents the input parameters for the present 11 models.

5.2.1 The Reference Model

The outcomes from the reference model *A* are displayed in Figure 5.1. In this case, the prevailing conditions inside the star cluster are: an average value for the gas density ~ 10 cm^{-3} and an average gas temperature $\sim 1.35 \times 10^7$ K. From those conditions, the dust temperature distributions are computed, $G(a, T_d)$, for different dust sizes, and the resultant flux averaged by the size distribution of graphite and silicate grains (see Appendix A). In order to quantify the contribution to the total flux, separate fluxes from graphite and from silicate grains are displayed. As shown in panels e) and f),
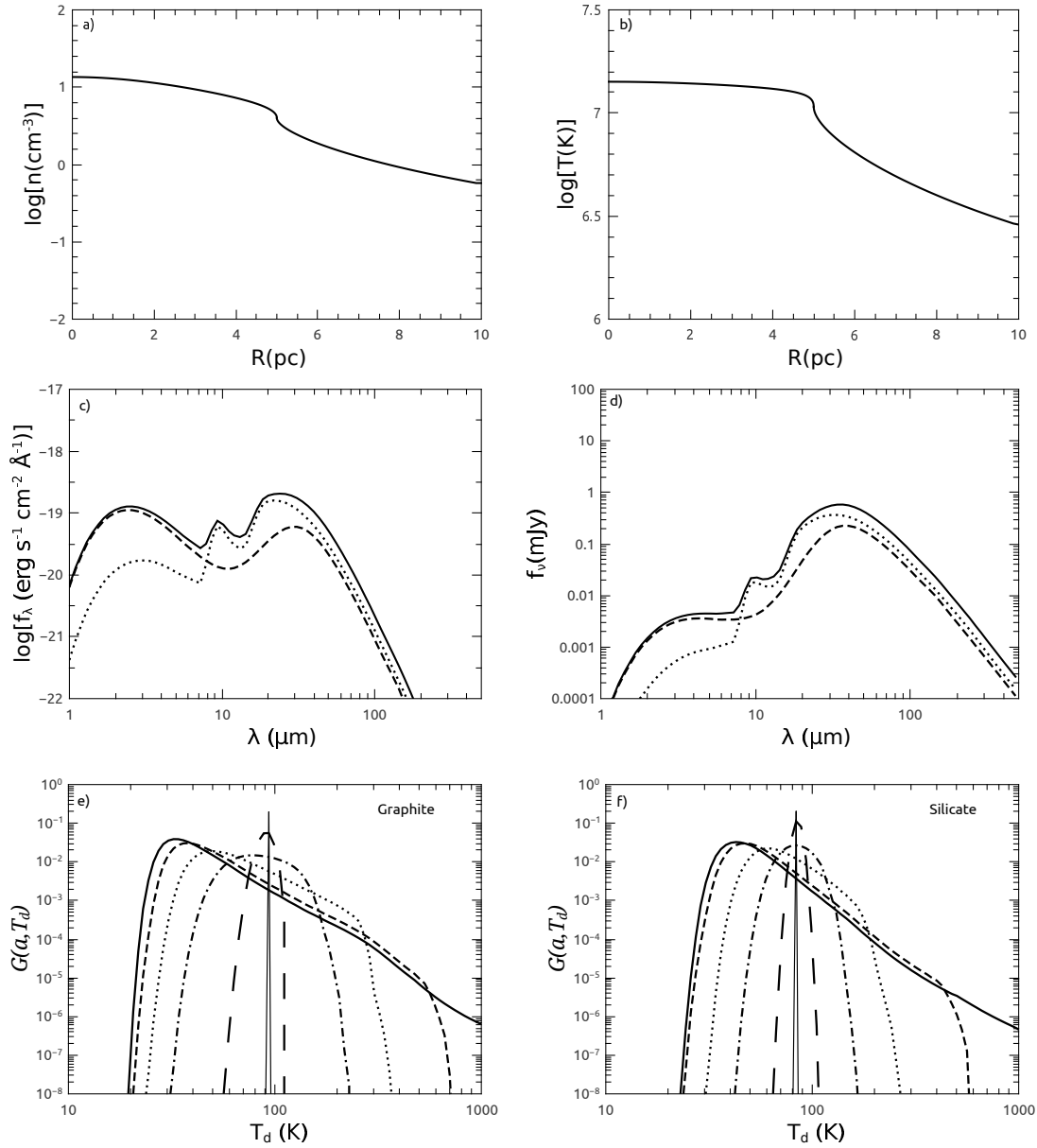
45

Figure 5.1: The Reference Model. Top panels a) and b), show the gas density and temperature radial profiles for the reference model *A*. Panels c) and d) present the fluxes per unit wavelength, f_λ, and per unit frequency, f_ν, respectively. The dashed line depicts the contribution from graphite grains, the dotted line the contribution from silicate grains while the solid line comprises both contributions. Bottom panels e) and f), present the dust temperature distribution for different grain sizes for graphite and silicate grains, respectively. In the bottom panels, the solid, dashed, dotted, dashed-dotted, long-dashed and the delta-like curves correspond to sizes 0.001, 0.002, 0.01, 0.05, 0.1 and 0.5 μm, respectively.

Table 5.1: Model Parameters

Model	t	R_c	R_{SC}	R_{hm}	L_{SC}	$V_{A\infty}$	Z_d
	(yr)	(pc)	(pc)	(pc)	(erg s^{-1})	(km s^{-1})	(10^{-3})
A	1000	4	5	3.52	3×10^{39}	1000	1.0
A1	17000	4	5	3.52	3×10^{39}	1000	3.1
A2	17500	4	5	3.52	3×10^{39}	1000	2.5
A3	25000	4	5	3.52	3×10^{39}	1000	0.4
A4	33000	4	5	3.52	3×10^{39}	1000	0.1
B	1000	4	5	3.52	1×10^{39}	1000	1.0
C	1000	4	5	3.52	9×10^{39}	1000	1.0
D	1000	4	5	3.52	3×10^{39}	750	1.0
E	1000	4	5	3.52	3×10^{39}	1500	1.0
F	1000	2	5	2.98	3×10^{39}	1000	1.0
G	1000	4	7	4.59	3×10^{39}	1000	1.0

small grains ($\lesssim 0.05$ μm) are more likely to undergo strong temperature fluctuations and therefore span a wide range of temperatures (from a few ~ 10 K to a few ~ 1000 K for grains with $a = 0.001$ μm, making them to strongly emit in all near-infrared (NIR), mid-infrared (MIR) and far-infrared (FIR) wavelengths) due to their low heat capacities (which scale as $\sim a^3$) and small cross sections.

On the other hand, big grains ($\gtrsim 0.1$ μm) with larger cross sections (which make them subject to more frequent collisions) emit nearly as a blackbody at their equilibrium temperature. Intermediate-size grains ($0.05 \gtrsim a \gtrsim 0.1$) exhibit a combination of both behaviors. Hence, the emission from 1 to 8 μm is dominated by hot and small graphite grains. Between 9 and 14 μm, the emission is dominated by the 10-micron broad feature, associated to the dust absorption efficiency, $Q_{abs}(\lambda, a)$, of silicate grains. The emission from 15 to several hundred microns peaks around ~ 35 μm; it is dominated by big grains near their equilibrium temperature (~ 93 K for graphite grains and ~ 75 K for silicate grains) and by small grains with temperatures ranging from ~ 10 K to ~ 100 K. Note that the emission from graphite and silicate grains is almost identical for $\lambda \gtrsim 35$ μm because their dust temperature distributions are very similar. In this case, the mass of dust inside the star cluster volume is $M_d(t = \tau_{inj}) = 0.19$ M$_\odot$.

The reference model *A* has been evaluated at four later times (models *A1*, *A2*, *A3* and *A4* evaluated at ~ 17000, 17500, 25000, and 33000 yr, respectively). When dust injection is not taking place (models *A2-A3*), the dust size distribution rapidly evolves and greatly departs from the injection dust size distribution as a consequence of the short timescale for thermal sputtering. This is reflected in a lack of small grains and therefore, the NIR excesses noted in models *A* and *A1* (evaluated just before the end of the first and second dust injection episodes, respectively) rapidly vanish. This situation is illustrated in Figure 5.2 which shows evolving spectral energy distributions for models *A*, *A1*, *A2*, *A3* and *A4*. Top panels show the evolution of the dust mass (panel a) and dust-
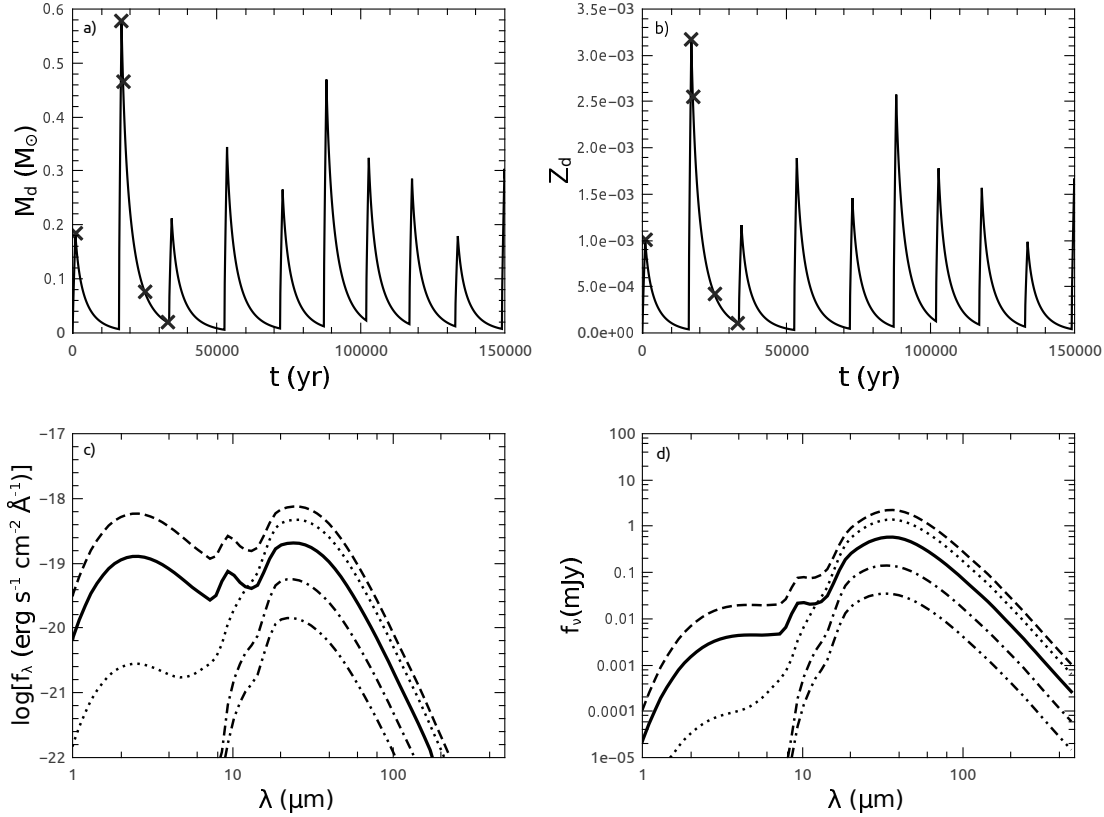
Figure 5.2: Spectral Energy Distributions for models *A*, *A1*, *A2*, *A3* and *A4*. Top panels a) and b) show the evolution of the dust mass and dust-to-gas mass ratio, respectively, during 9 injection events taking into account both dust sputtering and their exit out of the cluster as a wind. The times at which models *A1-A4* were evaluated are marked with crosses. Bottom panels c) and d) present the values of the fluxes per unit wavelength, f_λ, and per unit frequency, f_ν, for each evolved models, respectively. Solid, dashed, dotted, dashed-dotted and dashed-double-dotted lines depict the SEDs for models *A*, *A1*, *A2*, *A3* and *A4*, respectively. Note that the strong emission present during dust injection rapidly vanishes when dust injection has ceased.

to-gas mass ratio (panel b) during 9 injection events; the times at which these models were evaluated are marked with crosses. Bottom panels show evolving spectral energy distributions at the end of the first dust injection (1000 years, model *A*), at the end of the second dust injection. A strong emission at NIR and MIR wavelengths is present during dust injection, however, when dust injection has ceased, this strong emission rapidly vanishes which is notorious just 500 years after dust injection (model *A2*). Models *A3* and *A4*, which are more affected by thermal sputtering and the exit of dust grains, have diminished dust-to-gas mass ratios and a negligible emission at NIR-MIR wavelengths. The mass of dust in models *A1-A4* is 0.61, 0.51, 0.14 and 0.06 $M_\odot$, respectively. One can note that in these models, roughly 20% of the total mass injected by each supernova explosion is expelled out from the star cluster as a wind.

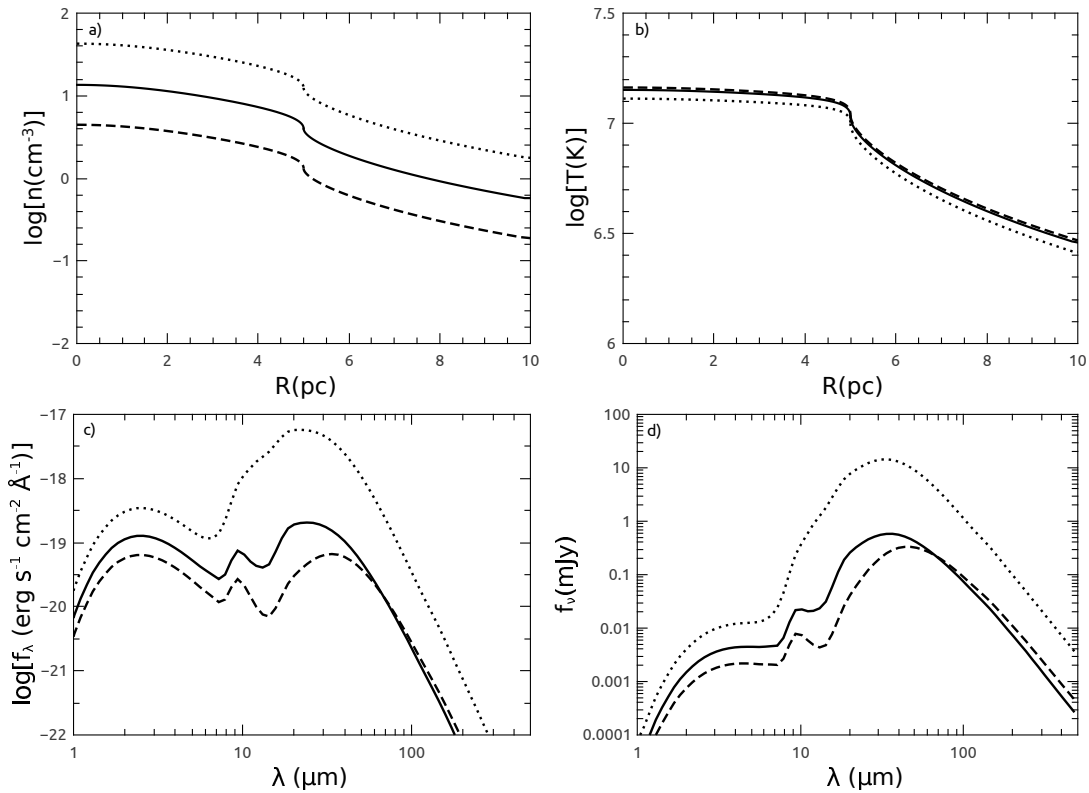## 5.2.2 Models with Different Star Cluster Mechanical Luminosities

Figure 5.3: Results for models with different mechanical luminosities A (3×10^{39} erg s^{-1}, solid curves), B (1×10^{39} erg s^{-1}, dashed curves) and C (9×10^{39} erg s^{-1}, dotted curves). Panels a) and b) show the gas number density and temperature profiles of each model, respectively. Panels c) and d) present the values of the fluxes per unit wavelength, f_λ, and per unit frequency, f_ν, for each model, respectively. Note that an increase in the star cluster mechanical luminosity (or equivalently in the mass of the star cluster), leads to an increase in the infrared emission from dust grains.

49

The results derived from models *A*,*B* and *C* are shown in Figure 5.3. These models (as well as models *D-G*) are evaluated at $t = \tau_{inj} = 1000$ yr. Models *B* and *C* consider three times smaller ($L_{SC} = 1 \times 10^{39}$ erg s^{-1}) and three times larger ($L_{SC} = 9 \times 10^{39}$ erg s^{-1}) values of the star cluster mechanical luminosity than what is considered in model *A*, respectively. An increase in the value of L_{SC}, yields a higher gas density inside the star cluster, which results in more frequent gas-grain collisions leading to an increase in the infrared emission (see equations 2.19 and 2.21 in Appendix C). As more massive clusters are considered, a higher supernova rate is expected and therefore, there is less time between supernova episodes to erode dust grains. This leads to a more persistent dust reservoir at all times which is reflected in an enhancement of the infrared spectrum. Thus, model *C* surpasses the infrared emission from models *A* and *B*. However, model *C* is also more affected by thermal sputtering which is noticeable by a decreased emission at $\lambda \lesssim 15\ \mu$m. The mass of dust inside R_{SC} at $t = \tau_{inj}$ is 6.0×10^{-2} M$_\odot$ and 0.57 M$_\odot$ for models *B* and *C*, respectively.

5.2.3 Models with Different Adiabatic Terminal Speeds

Figure 5.4 shows the results obtained from models *A,G* and *E*. In these models different values of the adiabatic wind terminal speed are examined. As the gas density decreases with an increasing adiabatic wind terminal speed, the characteristic time between successive electron collisions with a dust grain increases (see equation 2.19 in Appendix C). Dust grains then are less heated and their emission decreases (model *E* compared to model *A*). The opposite situation occurs in models with a lower value of the adiabatic wind terminal speed (model *D* compared to model *A*) which also causes a decreased in the emission at $\lambda \lesssim 15\ \mu$m provoked by the depletion of small grains by the action of thermal sputtering in a denser medium. The mass of dust inside R_{SC} is 0.47 M$_\odot$ and 5.29×10^{-2} M$_\odot$ for models *D* and *E*, respectively.

5.2.4 Models for Different Cluster Sizes

Models *F* and *G* focus on models with different values of R_c and R_{SC} (see Figure 5.5). Model *F* is evaluated with a smaller star cluster core radius $R_c = 2$ pc. Model *G* corresponds to a star cluster with a larger cut-off radius $R_{SC} = 7$ pc. A more compact cluster, as in model *F* compared to model *A*, yields an enhanced flux at all wavelengths, however, this effect is more noticeable at FIR wavelengths where the role of thermal sputtering is less important. The situation is different when one considers a less compact cluster (model *G* compared to model *A*), when the gas number density is decreased and therefore, the dust emission is diminished. In these models, half of the star cluster mass is located inside 3.52 pc, 2.98 pc and 4.59 pc for models *A*, *F* and *G*, respectively. The mass of dust inside the star cluster volume is 0.21 M$_\odot$ and 8.62×10^{-2} M$_\odot$ for models *F* and *G*, respectively.
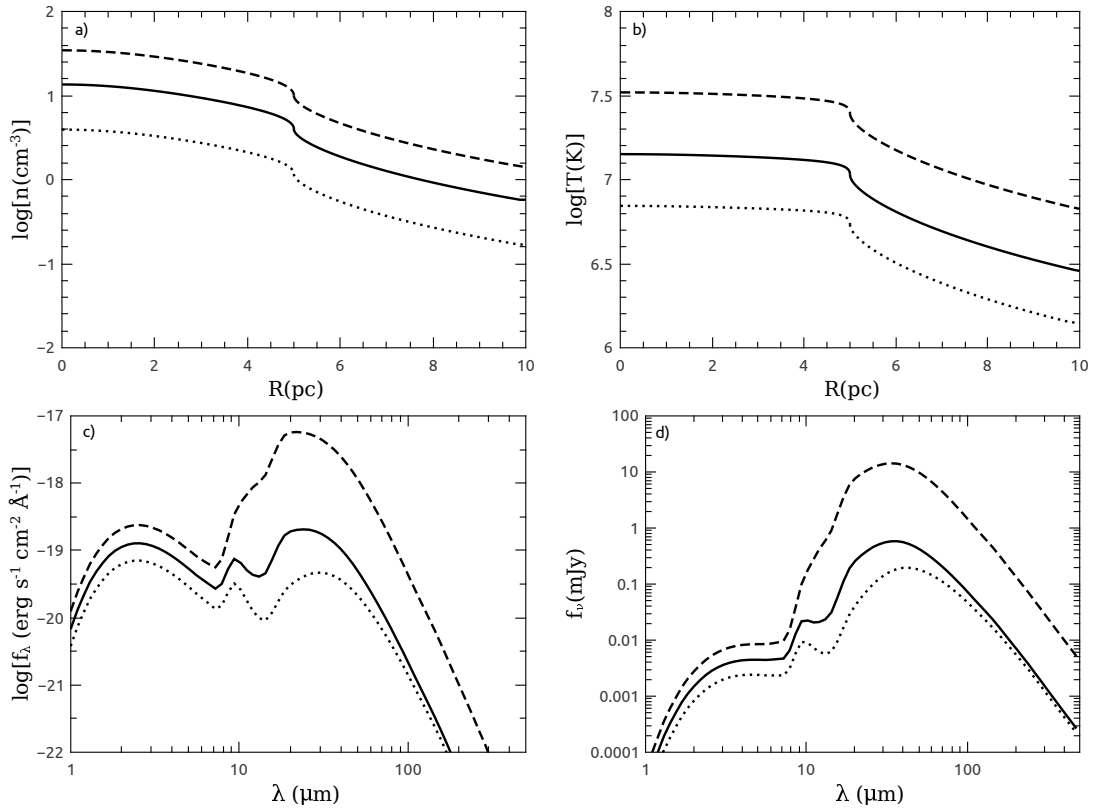
Figure 5.4: Same as Figure 5.3 but for models with different adiabatic wind terminal speeds A (1000 km s^{-1}, solid curves), D (750 km s^{-1}, dashed curves) and E (1500 km s^{-1}, dotted curves). Note that an increase in the adiabatic terminal speed, lead to a decrease in the dust emission inside the star cluster volume.
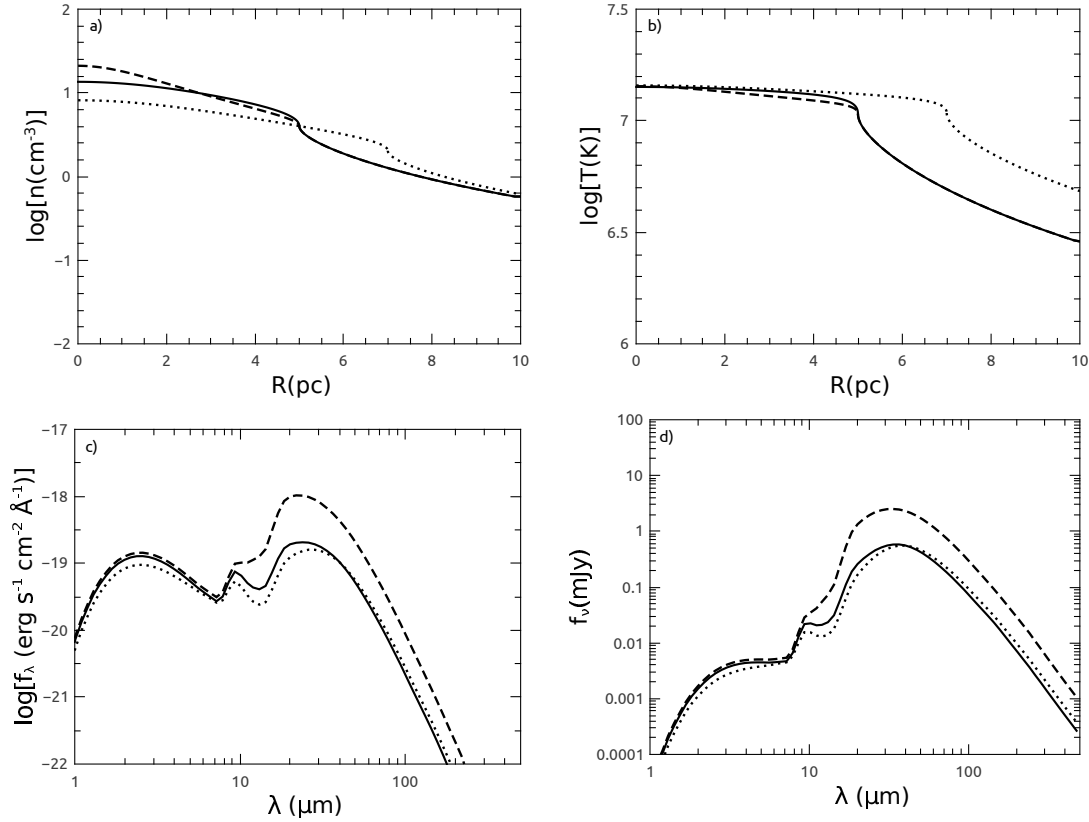
51

Figure 5.5: Same as Figure 5.3 but for models with different star cluster sizes. Solid lines correspond to model A ($R_c = 4$ pc, $R_{SC} = 5$ pc and $R_{hm} = 3.92$ pc), dashed lines display the results obtained from model F ($R_c = 2$ pc, $R_{SC} = 5$ pc and $R_{hm} = 3.52$ pc), and dotted lines show the results from model G ($R_c = 4$ pc, $R_{SC} = 7$ pc and $R_{hm} = 5.45$ pc). Note that more compact clusters lead to an increase in the dust emission inside the star cluster volume, especially at FIR wavelengths.

52

5.3 Summary

Motivated by the abundant evidence for core-collapse supernovae as major dust producers, and the large SN rate expected in young massive star clusters, here the frequent injection of dust grains into the plasma interior of super star clusters has been studied. Thus super star clusters become ideal laboratories to study dust grains which are heated by means of random gas-grain collisions. Then the hydrodynamic star cluster wind model has been combined with the stochastic dust injection, heating and cooling models to calculate the expected spectral energy distributions from super stellar clusters.

The evolution of the grain size distribution has been followed, what changes drastically the resultant spectrum. The exit of dust grains as they stream out, coupled to the gas, to compose the star cluster wind has also been considered. For the latter, a finite difference method was employed.

In this scenario, a certain mass of silicate and graphite dust, and an initial grain size distribution is injected into the intracluster medium. On top of this, the stellar winds are steady but the rate of supernova makes the dust injection an stochastic process. Therefore, dust is injected into the medium stochastically, and then heated and eroded before the next injection episode.

Several models were defined in order to quantify all these effects in the resultant infrared spectrum. Models which give more weight in the dust size distribution to small grains (as when dust injection is taking place), as well as models with larger values of the star cluster mechanical luminosity (in which the SN rate increases leading to more persistent dust reservoirs), lead to an enhanced dust emission. The opposite situation occurs with more extended star clusters and larger adiabatic terminal speeds, which lead to a decrease in their dust emission. When dust injection ceases, the resultant SEDs change drastically and the emission at NIR-MIR wavelengths vanishes due to thermal sputtering acting more effectively on small grains.

Despite the fact that these models imply the presence from hundredths to tenths of solar masses of dust inside the star cluster volume and transient strong NIR-MIR infrared excesses, the predicted SEDs are strong enough to be considered in order to explain the infrared excesses observed in bright young clusters and other stellar systems. In those cases, the combined action of many nearby star clusters, as well as higher SN rates in more massive clusters, could led to persistent infrared excesses. This and a detailed comparison with the observations of starburst galaxies will be part of future work.

The results obtained in this Chapter are published in the paper Martínez-González et al. (2016).

Chapter 6

Dusty Wind-Driven Shells

Stellar feedback - the injection of radiation and mechanical energy by young massive stars - plays a major role in the dynamics and structuring of the ISM around super star clusters. Powerful super star cluster winds and radiation pressure sweep-up the interstellar gas into thin expanding shells which trap the ionizing radiation produced by the central clusters affecting the dynamics and the distribution of their ionized gas. The trapping of the ionizing radiation emerging from an exciting cluster by either dust grains and recombining atoms leads to a non homogeneous density distribution even within static or pressure confined HII regions. This Chapter discusses the impact that the two major forces, the dynamic and radiation pressure, provide on the distribution of matter and thermal pressure within such shells.

The Chapter is organized as follows: in Section 6.1 the major equations formulated by Draine (2011, hereafter Dr11) for static spherically symmetric HII regions are presented together with a discussion on how the inner and outer boundary conditions affect the solution. In Section 6.2 different hydrodynamic regimes are discussed and also it is shown how Dr11's equations may be applied to the whole shell, including the outer, non-ionized segments. The results of the calculations are presented and discussed in Section 6.3 where different hydrodynamical models (standard energy and momentum dominated, leaky and low star clusters heating efficiency) are compared, then I calculate the model-predicted values of the ionization parameter and compare them to typical values found in local starburst galaxies. These results are also placed onto a diagnostic diagram which allows one to discriminate between the radiation pressure and wind pressure (thermal or ram) dominated regimes. The major results are summarized in Section 6.4.

6.1 Radiation pressure in static, dusty HII regions

Consider the idealized model of a static spherically symmetric HII region ionized by a central star cluster and confined by the thermal pressure of the ambient interstellar medium (ISM). Following Dr11, it is assumed that the outward force provided by radi-

ation pressure is balanced by the inward directed thermal pressure gradient. The set of equations describing such HII regions in the presence of dust grains is (cf. Dr11):

$$\frac{\mathrm{d}}{\mathrm{d}r}\left(\frac{\mu_i}{\mu_a}nkT_i\right) = n\sigma_d\frac{[L_n e^{-\tau} + L_i\phi]}{4\pi r^2 c} + n^2\beta_2\frac{\langle h\nu\rangle_i}{c} \, , \qquad (6.1)$$

$$S_0\frac{\mathrm{d}\phi}{\mathrm{d}r} = -\beta_2 n^2 - n\sigma_d S_0\phi \, , \qquad (6.2)$$

$$\frac{\mathrm{d}\tau}{\mathrm{d}r} = n\sigma_d \, , \qquad (6.3)$$

where L_i and L_n are the luminosities in ionizing and non-ionizing photons, respectively ($L_i + L_n = L_{bol}$, where L_{bol} is the bolometric luminosity of the cluster), $n(r)$ is the ionized gas density, $\phi(r)$ is the fraction of the ionizing photons that reaches a surface with radius r, $S_0 = Q_0/4\pi r^2$ where Q_0 is the number of ionizing photons emitted by the star cluster per second, $\langle h\nu\rangle_i = L_i/Q_0$ is the mean energy of the ionizing photons, $\tau(r)$ is the dust absorption optical depth, σ_d is the effective dust absorption cross section per hydrogen atom, $\beta_2 = 2.59 \times 10^{-13}$ cm^3 s^{-1} is the recombination coefficient to all but the ground level (Osterbrock, 1989), k and c are the Boltzmann constant and the speed of light, respectively, and T_i is the ionized gas temperature. It is assumed that the gas in the HII region is completely ionized and has a normal chemical composition with one helium atom per every ten hydrogen atoms. The mean mass per particle and the mean mass per ion then are: $\mu_a = 14/23 m_H$ and $\mu_i = 14/11 m_H$, respectively, where m_H is the proton mass. The value of the dust absorption cross section per hydrogen atom is set to $\sigma_d = 10^{-21}$ cm^2 (Dr11) and it is assumed that the temperature of the ionized gas is constant and equal to $T_i = 10^4$ K throughout this work. The first and the second terms on the right-hand side of equation (6.1) correspond to the photon momentum absorbed by dust grains and by the gas, respectively. The right-hand terms in equation (6.2) are the rates of absorption of ionizing photons in a thin spherical shell with radius r and thickness $\mathrm{d}r$ by recombination and by dust grains, respectively.

In order to select a unique solution of equations (6.1 - 6.3), one has to adopt a set of initial or boundary conditions. For example, Draine (2011) selected solutions by choosing the initial value of density at some fixed radius r. Here similar initial conditions are employed in the case of the wind-driven shell (cf. next Section), but prefer to select the static solution from the two boundary conditions which are the values of the confining pressure at the inner and outer edges of the HII region. Here it is assumed that the HII region is static and that the radiation field from the central cluster is strong enough to clean up the central region with a radius R_i as it seems appropriate to many galactic and extragalactic HII regions which are better fitted with models containing an empty central zone in the ionized gas distribution (cf. Dopita et al., 2003; Kewley & Dopita, 2002; Mathews, 1967, 1969). In such a case, the conditions at the inner edge of the HII region are: $\phi(R_i) = 1$, $\tau(R_i) = 0$ and $n(R_i) \to 0$ (cf. Dr11) whereas the value of the initial radius R_i is selected by the outer boundary condition which requires the thermal pressure at the outer edge of the HII region R_{HII} to be equal to that in the ambient ISM. A value of $n(R_i) = 10^{-10}$ cm^{-3} is used for the calculations and the integration stops

when all ionizing photons are trapped and thus the function ϕ becomes equal to zero: $\phi(R_{HII}) = 0$.

The input parameters (Q_0, L_i and L_n) for the calculations were taken from the Starburst99 synthesis model (Leitherer et al., 1999) and are summarized in Table 6.1. Models A, B and C correspond to a 10^6 M$_\odot$ coeval stellar cluster with a standard Kroupa initial mass function with upper and lower cut-off mass of 100 M$_\odot$ and 0.1 M$_\odot$ respectively and a turn off mass at 0.5 M$_\odot$, metallicity $Z = 0.4\,Z_\odot$, age $t \sim 1$ Myr and Padova evolutionary tracks with AGB stars, embedded into an interstellar gas with number density 1 cm^{-3}, 10^3 cm^{-3} and 10^6 cm^{-3}, respectively. Models D, E and F correspond to a two orders of magnitude less massive cluster of the same age located within the same environments.

Table 6.1: Stationary HII region models

Models	Q_0 s^{-1}	L_i $\mathrm{erg\ s}^{-1}$	L_n $\mathrm{erg\ s}^{-1}$	n_{ISM} cm^{-3}
A,B,C	4.27×10^{52}	1.44×10^{42}	1.96×10^{42}	$1, 10^3, 10^6$
D,E,F	4.27×10^{50}	1.44×10^{40}	1.96×10^{40}	$1, 10^3, 10^6$

The calculated density distributions for static HII regions with a central cavity are shown in Figure 6.1. The density grows always rapidly in a very narrow inner zone and then presents an almost even or flat distribution in the rest of the volume if the density of the ambient ISM is not very large (models A, B, D and E). Only when the exciting clusters are embedded into a very high density ambient medium ($n_{ISM} = 10^6$ cm^{-3}, models C and F) the density of the ionized gas grows continuously across the whole HII region. However, such HII regions are very compact (cf. left-hand panels in Figure 6.1). The size of the HII region, R_{HII}, and the radius of the inner empty cavity R_i are both functions of the interstellar ambient density. Both radii grow rapidly as one considers a lower ambient density (cf. the left-hand side panels in Figure 6.1) where the steps in the gas density distribution mark the edge of the HII regions and result from the condition that the thermal pressure at the HII region edge ought to be equal to that of the ambient neutral gas with a two orders of magnitude lower temperature ($T_{ISM} = 100$ K). This however is not evident when distances are normalized to the radius of the HII region and densities to their rms values as on Figure 2 of Dr11 (cf. right-hand panels in Figure 6.1). Thus dimensionless plots do not allow one to realize that static models with a low ambient density are unrealistic as in these cases the required time for the ionized gas re-distribution (the sound crossing time) highly exceeds the characteristic lifetime of the HII region, $\tau_{HII} \sim 10$ Myr.
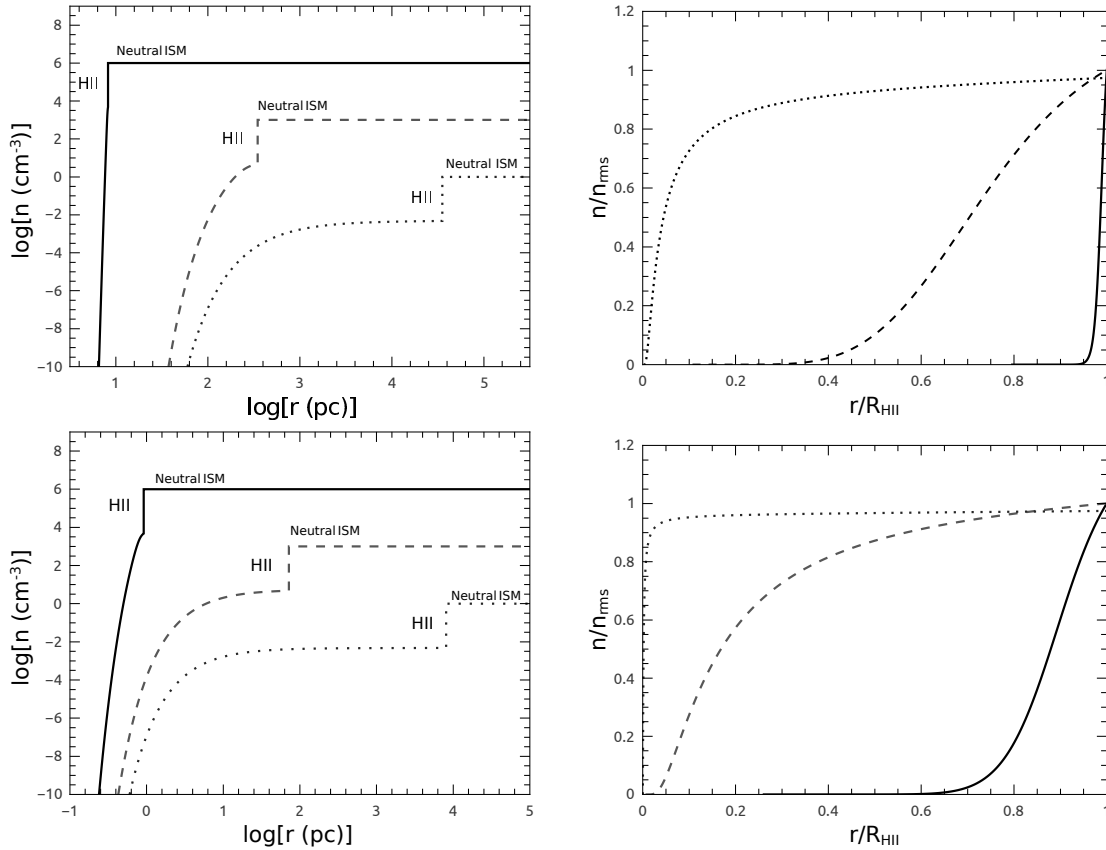
Figure 6.1: Static HII regions with a central cavity. The upper left-hand panel presents the gas number density distribution as a function of radius for models A (dotted line), B (dashed line) and C (solid line) in a log-log scale. The upper right-hand panel shows the same distributions when all distances are normalized to the radius of the HII region and densities to their rms values. The bottom panels present similar density distributions for models D (dotted line), E (dashed line) and F (solid line), respectively.

6.2 Radiation pressure in dusty wind-driven shells

Given the continuous supply of photons and their instantaneous re-processing by the surrounding gas, here Dr11's equations are adapted to calculate the impact that radiation pressure has on the structure and on the dynamics of evolving wind-driven shells. A constant density ISM and a set of evolving star cluster parameters are considered to evaluate at consecutive times the impact of radiative pressure on the evolving shells and thus neglect all effects dealing with a plane-stratified density distribution in galactic disks, gas shear and gravity. The impact that the ambient pressure provides on the shell dynamics is also not taken into account as it is only significant when the shell expansion velocity approaches the sound speed value in the ambient ISM. The distribution of the ionized gas then becomes quasi-static and is defined by the values of thermal pressure at the inner edge of the shell and in the ambient ISM as was discussed in the previous Section. In the strongly supersonic regime (which is the case in all the present calculations, see the captions in Figures 6.3 and 6.4), the rate of mass accumulation by the expanding shell depends on the speed of the leading shock, $V_s \sim (P_{edge}/\rho_{ISM})^{1/2}$, where P_{edge} is the thermal pressure value immediately behind the leading shock and ρ_{ISM} is the gas density in the ambient ISM. The impact of the external pressure on the shell dynamics is thus negligible in this case. When a star cluster wind impacts a constant density ISM, a four zone structure is established: there is a central free wind zone, surrounded by a shocked wind region. The latter is separated by a contact discontinuity from the matter swept up by the leading shock which evolves into the constant density ISM (cf. Koo & McKee, 1992; Mac Low & McCray, 1988; Weaver et al., 1977). In the wind-blown bubble case, the central zones are hot and thus transparent to the ionizing flux as it is also the case in the static HII regions with a central cavity considered in the previous Section. However, the density at the inner edge of the ionized shell is not arbitrarily small, but must be selected from the condition that $P_{HII}(R_s) = P_s$, where $P_{HII}(R_s)$ and P_s are the thermal pressures at the inner edge of the ionized shell and in the shocked wind region, respectively, and R_s is the inner radius of the ionized shell. The swept up shell is also hot at first ($T \geq 10^6$ K) and thus transparent to the ionizing radiation from the star cluster. However, it cools down in a short time scale due to strong radiative cooling. If the density and metallicity of the ambient medium are n_{ISM} and Z_{ISM}, respectively, and the star cluster mechanical luminosity is L_{SC}, the shell characteristic cooling time scale, τ_{cool}, is (Mac Low & McCray, 1988):

$$\tau_{cool} = (2.3 \times 10^4) Z_{ISM}^{-0.42} n_{ISM}^{-0.71} \left(\frac{L_{SC}}{10^{38} \text{ erg s}^{-1}} \right)^{0.29} yr. \tag{6.4}$$

Only after that time the swept up shell begins to recombine and absorb the ionizing radiation from the central cluster. For $L_{SC} = 10^{40}$ erg s^{-1}, $Z_{ISM} = 0.4 Z_\odot$ and $n_{ISM} = 1$ cm^{-3}, $\tau_{cool} \sim 0.12$ Myr while for an ISM with $n_{ISM} = 1000$ cm^{-3}, $\tau_{cool} \sim 10^{-3}$ Myr. When the wind-driven shell grows thick enough, it absorbs all ionizing photons and then forms an outer neutral skin which absorbs only non-ionizing photons that manage to escape the inner ionized part of the shell. One can calculate how these photons

affect the distribution of density and thermal pressure in the neutral part of the shell by removing the ionizing radiation from Dr11's equations and evaluating the rate at which non-ionizing energy, L_{nesc}, escapes from the ionized part of the shell. This leads to the set of equations:

$$\frac{\mathrm{d}n}{\mathrm{d}r} = \frac{n\sigma_d}{kT_n}\frac{L_{nesc}e^{-\tau}}{4\pi r^2 c} , \tag{6.5}$$

$$\frac{\mathrm{d}\tau}{\mathrm{d}r} = n\sigma_d . \tag{6.6}$$

It was assumed in all the calculations that the temperature in the outer, neutral part of the shell is constant and equal to $T_n = 100$ K. It was also assumed that the shell is thin and thus the total mass of the shell is $M_{sh} = 4\pi\rho_{ISM}R_s^3/3$.

Thus, the initial conditions which allow one to select a unique solution of equations (6.1-6.3) in the case of the wind-blown shell are very similar to those used in the previous Section: $\phi(R_s) = 1$, $\tau(R_s) = 0$ and the value of the thermal pressure in the shocked wind zone which depends upon the dynamical time t. However the inner radius of the ionized shell R_s and the pressure P_s at the inner edge of the shell at different evolutionary times t are calculated from the Weaver et al. (1977) wind-blown bubble model and the integration stops when the total mass of the ionized and neutral segments reaches M_{sh}. The values of thermal pressures at the outer (P_{edge}) and inner (P_s) edges of the swept-up shell obtained from the calculations are compared in order to check if radiation pressure may affect the shell dynamics significantly.

In the energy-dominated regime, R_s and P_s are (Bisnovatyi-Kogan & Silich, 1995)

$$R_s(t) = \left[\frac{375(\gamma - 1)L_{SC}}{28(9\gamma - 4)\pi\rho_{ISM}}\right]^{1/5} t^{3/5}, \tag{6.7}$$

$$P_s(t) = 7\rho_{ISM}^{1/3}\left[\frac{3(\gamma - 1)L_{SC}}{28(9\gamma - 4)\pi R_s^2}\right]^{2/3}, \tag{6.8}$$

where ρ_{ISM} is the interstellar gas density and $\gamma = 5/3$ is the ratio of specific heats. At this stage the free wind occupies only a small fraction of the bubble volume and the value of thermal pressure P_s is defined by the amount of thermal energy accumulated in the shocked wind region and the bubble volume and thus does not depend on the wind terminal speed directly (see for more details Bisnovatyi-Kogan & Silich, 1995). The ion number density at the inner edge of the ionized shell then is:

$$n_s(t) = \frac{\mu_a P_s}{\mu_i kT_i}. \tag{6.9}$$

However, evaporation of the swept-up shell into the hot shocked wind region may cause strong radiative cooling and lead to the end of the energy dominated regime. If the star cluster is embedded into an ambient ISM with density n_{ISM}, this occurs at (Mac Low

& McCray, 1988):

$$\tau_{tran} = (1.6 \times 10^7)Z_{ISM}^{-35/22}n_{ISM}^{-8/11}\left(\frac{L_{SC}}{10^{38} \text{ erg s}^{-1}}\right)^{3/11} yr. \tag{6.10}$$

After this time the free wind impacts directly on the shell and the thermal pressure at the inner edge of the swept-up shell is equal to the wind ram pressure $P_{ram} = \rho V_{A\infty}^2$, where $\rho = \dot{M}/4\pi R_s^2 V_{A\infty}$, $\dot{M}$ is the star cluster mass deposition rate and $V_{A\infty} = (2L_{SC}/\dot{M})^{1/2}$ is the adiabatic wind terminal speed. The shell further expands in the momentum dominated regime as (cf. Silich & Tenorio-Tagle, 2013, hereafter ST13):

$$R_s(t) = R_{tran}\left[\frac{3L_{SC}(t^2 + \tau_{tran}^2)}{\pi V_{A\infty}\rho_{ISM}R_{tran}^4} + \left(\frac{12}{5} - \frac{6L_{SC}\tau_{tran}^2}{\pi V_{A\infty}\rho_{ISM}R_{tran}^4}\right)\frac{t}{\tau_{tran}} - \frac{7}{5}\right]^{1/4} \tag{6.11}$$

$$P_s(t) = \frac{L_{SC}}{2\pi V_{A\infty}R_s^2}, \tag{6.12}$$

The radius of the shell at the time of the transition, R_{tran}, must be calculated by means of equation (6.7) at $t = \tau_{tran}$. Weaver's et al. equations do not include the momentum of starlight, however, as shown below, these terms do not make a major difference in the evolution of the bubbles except in the case of a low heating efficiency. The ion number density at the inner edge of the ionized shell in this case is:

$$n_s(t) = \frac{\mu_a P_{ram}}{\mu_i k T_i}. \tag{6.13}$$

Note, however, that if thermal conduction and mass evaporation of the outer shell are inhibited by magnetic fields, the radiative losses of energy from the shocked wind region remain negligible and the wind-driven bubble expands in the energy dominated regime during the whole evolution of the HII region (cf. ST13).

To assess the impact that radiation pressure provides on the shell, several models are run (cf. Table 6.2) with input parameters L_{bol}, L_i, L_n, L_{SC} and Q_0, which one has to know in order to use equations (6.1 - 6.3) and (6.5 - 6.6). These values were taken from the Starburst99 synthesis code at the corresponding times $t = 1$ Myr, 3.3 Myr and 5 Myr, respectively (cf. Figure 6.2).

Table 6.2: Wind-driven shell models

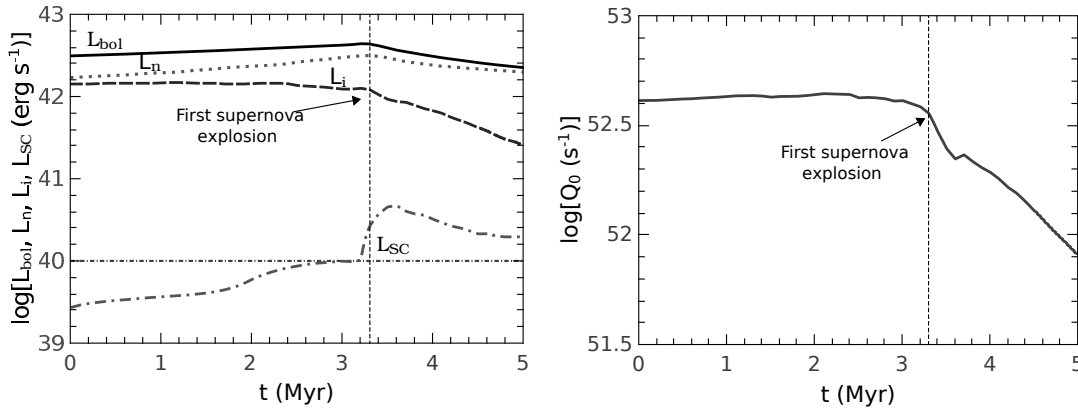| Models	L_{SC}	n_{ISM}	Z_{ISM}	t	Regime
	erg s^{-1}	cm^{-3}	$Z_\odot$	Myr	
LDS a, b, c	10^{40}	1	0.4	1, 3.3, 5	Low density energy dominated
LDL a, b, c	10^{40}	1	0.4	1, 3.3, 5	Low density with gas leakage
HDS a, b, c	10^{40}	10^3	0.4	1, 3.3, 5	High density energy/momentum dominated
HDE a, b, c	10^{40}	10^3	0.4	1, 3.3, 5	High density with low heating efficiency

Figure 6.2: Input parameters as a function of time. The left-hand panel shows the evolution of the bolometric (solid line), non-ionizing (dotted line), ionizing (dashed line) and mechanical (dash-dotted line) luminosities. The horizontal dash-dotted line displays the value of mechanical luminosity that has been used in Weaver et al. (1977) analytic relations. The right-hand panel shows the number of ionizing photons produced by a 10^6 M$_\odot$ cluster per unit time. The vertical lines in both panels mark the onset of supernova explosions.

To calculate the inner radius of the ionized shell and the ionized gas density at the inner edge of the HII region equations (6.7-6.9) were used and if equation (6.10) is fulfilled these were replaced by equations (6.11-6.13). The procedure thus implies that the dynamical evolution of the shell is done through the classical Weaver's et al. equations, while the density and pressure structure of the swept up shell is evaluated by means of Dr11's static equations. In all of these, an average mechanical luminosity $L_{SC} = 10^{40}$ erg s^{-1} was used.

6.3 Results and discussion

6.3.1 Shells evolving in a low density ISM

The impact that radiation provides on the wind-driven shells expanding into a low density ambient medium is first explored (Table 6.2, LDS model). Models LDSa, LDSb and LDSc present different evolutionary stages of the "standard bubble model". In this case the wind-driven shell expands into a low density (1 cm^{-3}) ISM in the energy-dominated regime. In all cases the mass of the driving cluster is 10^6 M$_\odot$ and the selected times allow one to see how the ionization structure of the shell changes with time due to the bubble and radiation field evolution.

Figure 6.3 displays the density (solid lines), thermal pressure (dashed lines) and ram pressure (dotted lines) distributions within and at both sides of the expanding shell, while this is exposed to the radiation from the central cluster. The sudden density jumps at the inner edge of the ionized shell result from the fact that the thermal pressure there must be equal to the thermal pressure of the hot thermalized cluster wind (equations
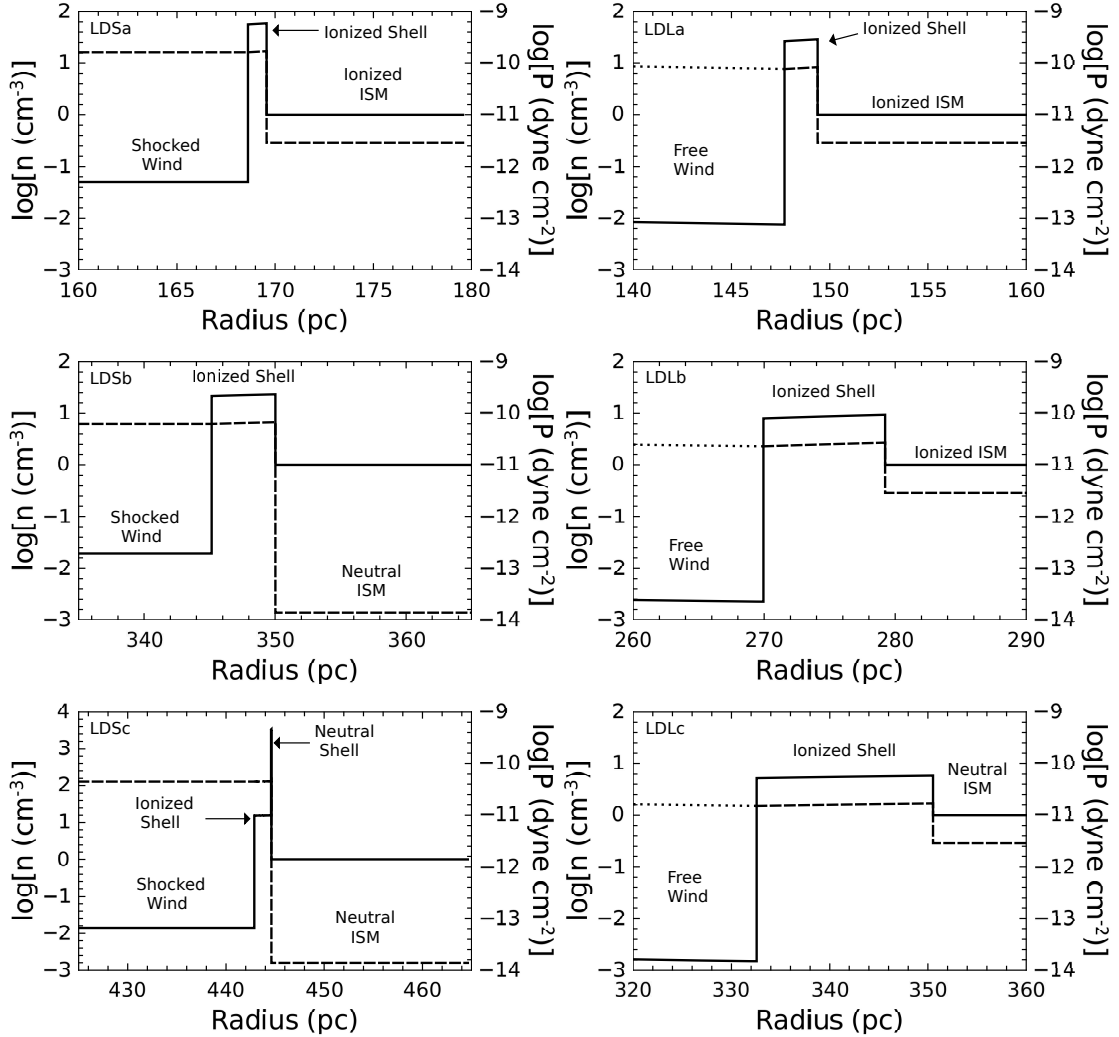
Figure 6.3: The wind-blown shell structure for a low-density environment. Zoom at the density (left-hand axes) and pressure (right-hand axes) distributions across and at both sides of the expanding shell. The left-hand panels present the results of the calculations for models LDSa (top panel), LDSb (middle panel) and LDSc (bottom panel). The right-hand panels displays the results for models with gas leakage: models LDLa (top panel), LDLb (middle panel) and LDLc (bottom panel), respectively. Solid lines show the radial density distribution in the shocked/free wind region, ionized, neutral shell and in the ambient ISM. Dashed and dotted lines display the distribution of thermal pressure inside the shell and in the ambient ISM and that of the ram pressure in the free wind region, respectively. The Mach number for the LDS models a, b and c is 84.96, 52.70 and 44.63, respectively, while for the LDL models a, b and c is 63.11, 34.52 and 28.02, respectively.

63

6.9) while the temperature in the ionized gas is 10^4 K. As shown in Figure 6.3, in the case of model LDSa ($t = 1$ Myr) the swept up shell has already cooled down and is completely photo-ionized by the Lyman continuum from the young central cluster. Furthermore, a fraction of the ionizing photons still escapes from the shell into the ambient ISM keeping it also at $T = 10^4$ K. Model LDSb presents the shell structure at the trapping time, $\tau_{trap} = 3.3$ Myr. At this time the shell absorbs all ionizing photons, and the mass of the ionized matter is exactly that of the swept-up shell: $M_{ion} = M_{sh}$. The thermal pressure outside of the shell then falls by two orders of magnitude as it is assumed that the temperature of the ambient neutral gas in this case is 100 K (cf. the left-hand middle and bottom panels in Figure 6.3).

The first supernova explosion also occurs at this time and thus the number of ionizing photons emerging from the central cluster begins to decay rapidly afterwards. Model LDSc presents the shell structure at a later time, $t = 5$ Myr, when all ionizing photons are absorbed in the inner segments of the shell and thus the outer skin of the shell remains neutral.

The conditions for model LDL assume a leaky bubble model (e.g. Harper-Clark & Murray, 2009; Matzner, 2002). In this case, the thermal pressure inside the wind-driven bubble drops below the Weaver et al. (1977) model predictions due to the escape of hot shocked-wind plasma through holes in the wind-driven shell. In this case individual bow shocks around the shell fragments should merge to create a coherent reverse shock near the contact discontinuity, or inner side of the broken shell (cf. Rogers & Pittard, 2013; Tenorio-Tagle et al., 2006). It is thus assumed that the minimum driving force on the shell in the leaky bubble model is determined by the cluster wind ram pressure at the shell location and can never fall below such value (ST13). Hereafter it will be assumed that in the leaky case the transition from energy to momentum dominated regimes occurs at the earliest possible time, 0.13 Myr, just after the shell cools down and thus replace equations (6.7-6.9) with equations (6.11-6.13) at this time. Certainly, this time is arbitrary, but warrants the maximum possible effect of radiation pressure.

The density and thermal pressure distributions within and at both sides of the shell in the leaky case are shown on the right-hand panels of Figure 6.3. Here the top middle and bottom panels correspond to models LDLa, LDLb and LDLc and thus present the density, thermal pressure and ram pressure profiles at the same evolutionary times $t = 1$, 3.3 and 5 Myr, respectively. The size of the leaky shell is smaller and its thickness larger than those predicted by the standard bubble model (model LDS) and the difference grows with time (compare the right and left-hand panels in Figure 6.3). Note also that the leaky shell is not able to trap all ionizing photons and form an outer neutral skin for a much longer time (in this case $\tau_{trap} \approx 5$ Myr). This is because in the leaky bubble model the driving pressure and thus the ionized gas density at the inner edge of the shell are much smaller than those in the standard case (LDS).

The expectations resulting from calculations of the ionized gas distribution in static configurations with low pressure central cavities (Section 6.1) had been that radiation pressure would lead to a non homogeneous thermal pressure and density distributions

64

inside the wind-driven shell. Both, density and thermal pressure should grow from a low value at the inner edge of the shell to a maximum value at the outer edge, as in the high density static models (cf. Section 6.1). The calculations however, do not show such large enhancements in density and in the leading shock driving pressure relative to that at the inner edge of the shell. The density enhancement is about ~ 1.04 and ~ 1.09 at 1 Myr, ~ 1.07 and ~ 1.18 at 3.3 Myr and ~ 1.04 and ~ 1.12 at 5 Myr in the standard and the leaky bubble model, respectively (cf. the left-hand and right-hand panels of Figure 6.3). Two more models were also explored for an order of magnitude less massive cluster (10^5 M$_\odot$). However, no significant difference was found with the above results (cf. Appendix C). These results demonstrate how significantly the inner boundary condition (the value of thermal pressure at the inner edge of the HII region) may change the ionized gas density distribution. The results also imply that the impact from radiation pressure on the dynamics of shells formed by massive young stellar clusters embedded into a low density ambient medium is not significant throughout their evolution even if all of the hot plasma leaks out from the bubble interior into the surrounding medium. Consequently, this allows for the use of equations (6.7-6.8) and (6.11-6.12), ignoring the impact of the starlight momentum.

6.3.2   Shells evolving in a high density ISM

The high-density models (Table 6.2, models HDS and HDE) are evaluated at the same dynamical times: $t= 1$, 3.3 and 5 Myr and are displayed in Figure 6.4. In these cases the model predicts that the transition from energy to the momentum dominated regime occurs at much earlier times (cf. equation 6.10). For example, in the case of model HDS, $\tau_{tran} \approx 1.58$ Myr. Thus, models HDSb and HDSc correspond to a shell expanding in the momentum dominated regime. The size of the shell in this case is much smaller than when it expands into a low density ISM, however the shell is much denser and thus recombines faster. Therefore in the high density cases the ionizing radiation is not able to photoionize the whole shell from the very early stages of the bubble evolution (cf. the top left-hand panel in Figure 6.4). The density in the ionized shell drops when the transition to the momentum-dominated regime occurs. This allows the central cluster to photoionized a larger fraction of the swept-up material. Therefore the relative thickness of the ionized shell increases between the 1 Myr and 3.3 Myr (compare panels HDSa and HDSb in Figure 6.4). After 3.3 Myr the number of ionizing photons decreases rapidly (Figure 6.2) and the relative thickness of the ionized shell becomes smaller again despite the drop in driving pressure and the consequent drop in the ionized gas density (cf. panel HDSc). The density gradient also reaches the maximum value at 3.3 Myr and then drops at latter times. The density (and thermal pressure) gradient across the ionized shell in the high density models is larger than in the low density cases. For example, the enhancement of density relative to that at the inner edge of the shell in model HDSa is ~ 1.14, in model HDSb is ~ 1.67 and in model HDSc ~ 1.25 (cf. the left-hand panels in Figure 6.4). This is because the inner radius

65

of the ionized shell in the high density case is smaller and thus the impact that radiation pressure provides on the shell is larger.

The right-hand panels in Figure 6.4 present the results of the calculations when the driving cluster has a low heating efficiency (models HDEa, HDEb and HDEc). These calculations were motivated by the discrepancy between the Weaver et al. (1977) model predictions and the observed sizes and expansion velocities of the wind-blown bubbles known as "the growth-rate discrepancy" (Oey, 1996) or "the missing wind problem" (Bruhweiler et al. 2010; Freyer et al. 2006, see also Dopita et al. 2005; Silich et al. 2007, 2009; Smith et al. 2006) and by the fact that at the initial stages of the bubble evolution the star cluster mechanical luminosity still does not reach the average value adopted in the present calculations (cf. Figure 6.2). At later stages of evolution a low heating efficiency may be physically justified by assuming mass loading of the matter left over from star formation, as in Wünsch et al. (2011), or an oversolar metallicity of the SN ejecta what enhances the cooling rate, as in Tenorio-Tagle et al. (2005). Another possible scenario for a low heating efficiency has been shown to also arise from the consideration of a reservoir of dust within the cluster volume, as illustrated in Chapters 4 and 5. In this case, the values of L_i, L_n and Q_0 are kept equal to those predicted by the Starburst99 synthetic model for a 10^6 M$_\odot$ cluster, but instead of using $L_{SC} = 10^{40}$ erg s^{-1}, as in models HDSa - HDSc, an order of magnitude smaller mechanical luminosity is employed: $L_{SC} = 10^{39}$ erg s^{-1}. The transition to the momentum dominated regime in this case occurs at ≈ 0.84 Myr. The relative thickness of the ionized shell is much larger than that in model HDS as the size of the shell is about two times smaller and thus the flux of the ionizing radiation is about four times larger than in model HDS (compare the left-hand and right-hand panels in Figure 6.4). This leads to the largest calculated enhancement in the shell density (and thus thermal pressure) relative to that at the inner edge of the shell which is: ~ 6.41 at $t = 1$ Myr, ~ 7.26 at 3.3 Myr and ~ 3.47 at 5 Myr. These results imply that radiation pressure must be taken into consideration in calculations with low heating efficiency and that Weaver et al. (1977) model (equations 6.7-6.8 and 6.11-6.12) must be corrected in this case. The radiation pressure may also contribute to the shell dynamics at very early stages (before 3 Myr) of the wind-blown bubbles evolution (cf. also Figure 3 in ST13). Similar results were obtained for the less massive (10^5 M$_\odot$) clusters. In this case the maximum enhancement of density is ~ 1.43 in the standard (HDS) case and ~ 4.68 in the low heating efficiency (HDE) model, respectively.

The time evolution of the thermal pressure excess, P_{edge}/P_s, where P_{edge} and P_s are the values of the thermal pressure behind the leading shock and at the inner edges of the wind-driven shell, is shown in Figure 6.5. In the high density models (dashed and dash-dotted lines) this ratio decreases first as the flux of ionizing energy at the inner edge of the shell drops faster (as R_s^{-2}) than thermal pressure in the shocked wind region which drops as $R_s^{-4/3}$ (cf. equation 6.8). It then grows to a larger value when the hydrodynamic regime changes from the energy to a momentum-dominated expansion and the wind pressure at the inner edge of the shell drops abruptly. After this time
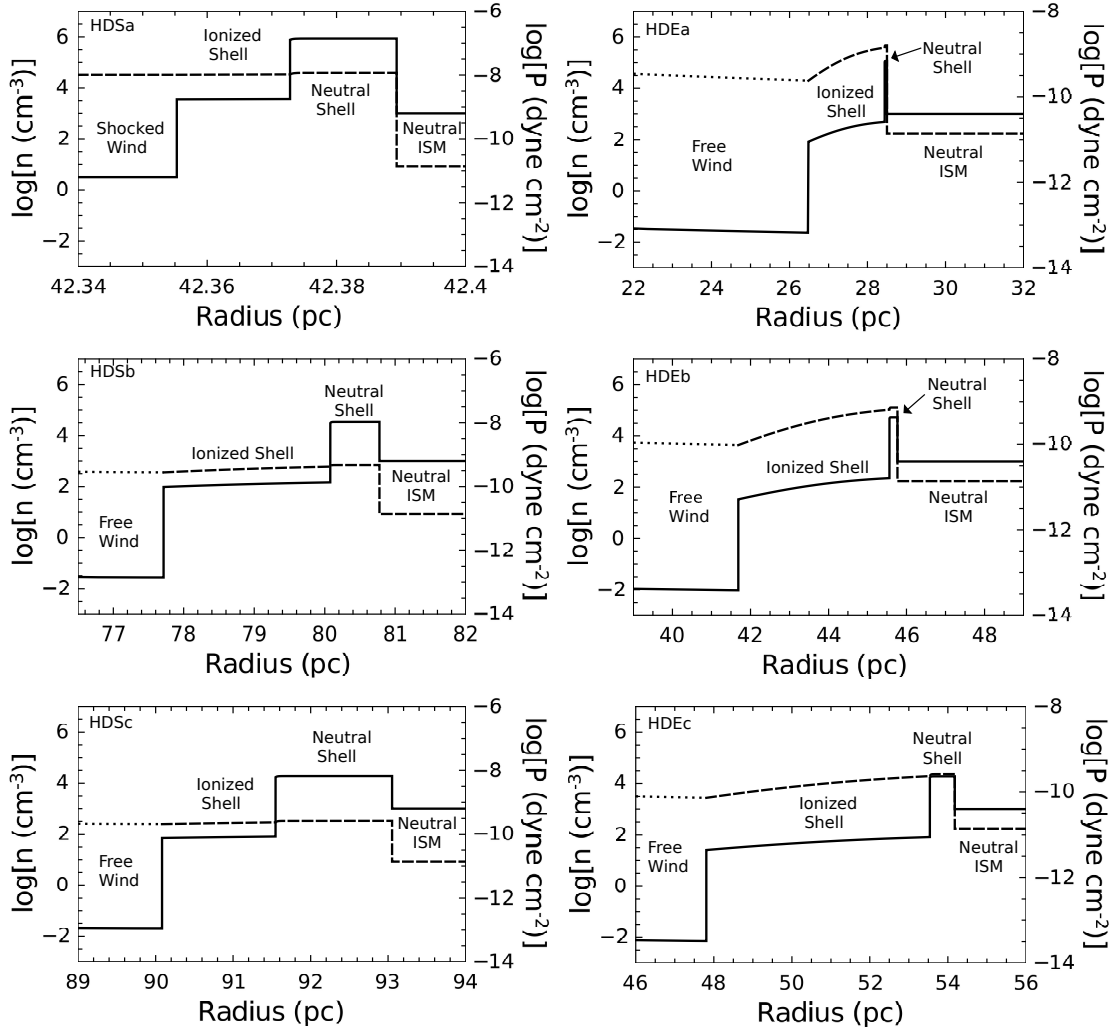
66

Figure 6.4: The wind-blown shell structure for a high-density environment. The left-hand column shows the results for models HDSa (top panel), HDSb (middle panel) and HDSc (bottom panel). The right-hand column displays the results for models with a low cluster heating efficiency: HDEa (top panel), HDEb (middle panel) and HDEc (bottom panel). Solid lines correspond to the radial density distribution (left axes) for the free wind, shocked wind, ionized shell, neutral shell and the ambient ISM. Dashed and dotted lines depict the radial thermal and ram pressure distributions (right axes), respectively. The Mach number for the HDS models a, b and c is 21.34, 7.35 and 5.20, respectively, while for the HDE models a, b and c is 11.14, 3.51 and 2.65, respectively.

67

both, the flux of radiation energy and the wind ram pressure at the inner edge of the shell drop as R_s^{-2}. The P_{edge}/P_s ratio then grows slowly as the number of non-ionizing photons absorbed by the outer neutral shell increases with time. The slow increase of the P_{edge}/P_s ratio continues until the number of ionizing photons begins to drop after the first supernova explosion at 3.3 Myr when the P_{edge} over P_s ratio reaches 1.67 ($\log P_{edge}/P_s \approx 0.22$) in the case of model HDSb and 7.26 ($\log P_{edge}/P_s \approx 0.86$) in the case of model HDEb.

In the low density cases (solid and dotted lines) the swept-up shell is not able to absorb all ionizing photons until it grows thick enough and therefore the number of ionizing photons trapped inside the completely ionized shell grows continuously until the first supernova explosion at 3.3 Myr. This compensates the R_s^{-2} drop of the ionizing energy flux and leads to a continuously growing P_{edge}/P_s ratio at this stage. However, in the standard (solid line) case and leaky (dotted line) bubble model this ratio remains always smaller than ~ 1.7. In the low density models LDS and LDL it is even smaller (less than 1.2) and is below the upper limit obtained in ST13. This is because in the low density cases wind-driven shells absorb only a fraction of the star cluster bolometric luminosity.

The fraction of the star cluster bolometric luminosity trapped within a shell as a function of time in models LDS, LDL, HDS and HDE is shown in Figure 6.6 by solid, dotted, dashed and dash-dotted lines, respectively. Note that the dashed and dash-dotted lines overlap rapidly as in the high density calculations expanding shells absorb all available (ionizing and non ionizing) photons at the very beginning of their time evolution (at $t << 1$ Myr). However, even in this case the shell remains optically thin to the IR photons re-emitted by dust grains, as shown in Figure 6.7. Here a dust opacity $\kappa_d = 2.3$ cm^2 g^{-1} is adopted (cf. Table 1 in Novak et al., 2012) and the optical depth for the IR radiation is calculated as $\tau_{IR} = \kappa_d \Sigma_s$, where the column density of the shell, Σ_s, is $\Sigma_s = \rho_{ISM} R_s/3$. The amplification of radiation pressure by the multiple re-emitted IR photons which is $\sim \tau_{IR} L_{bol}/c$ (cf. Hopkins et al., 2011; Krumholz & Thompson, 2012) thus remains less than unity. In all the present calculations, the amplification factor never exceeds 2, even if one uses a larger dust opacity, $\kappa_d = 5$ cm^2 g^{-1} adopted by Hopkins et al. (2011). This implies that the star cluster wind-driven shells expand in the radiation momentum rather than in the radiation energy dominated regime (cf. Fall et al., 2010; Krumholz & Thompson, 2012, for the detailed discussion of the two limiting cases).

It was also computed how radiation pressure affects the density and thermal pressure distribution in the case when the exciting cluster is embedded into a low ($n_{ISM} = 1$ cm^{-3}) density ISM and has a low heating efficiency and in the case of a leaky shell moving into a high ($n_{ISM} = 1000$ cm^{-3}) density medium. A little difference was found between these calculations and models LDL and HDS, respectively. For example, the enhancement of density from the inner to the outer edge of the shell in the low density calculations with a 10% heating efficiency is about 1.13, 1.2 and 1.11 at 1 Myr, 3.3 Myr and 5 Myr, whereas in the leaky bubble model LDL it is ~ 1.1, ~ 1.19 and ~ 1.12,
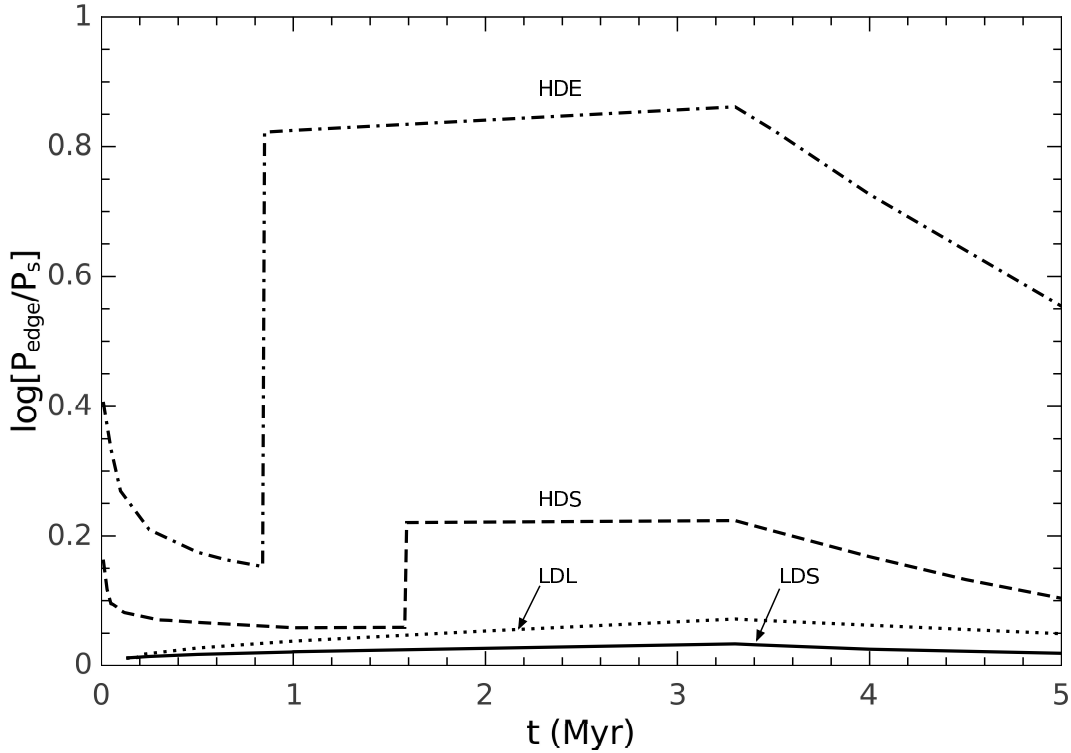
68

Figure 6.5: The P_{edge}/P_s ratio time evolution. The solid, dotted, dashed and dash-dotted lines display the logarithm of the P_{edge} over P_s ratio, $\log P_{edge}/P_s$, at different times t in the case of models LDS, LDL, HDS and HDE, respectively.

respectively. In the case when a leaky shell expands into a high density medium, the enhancement of density is : ~ 1.61 at 1 Myr, ~ 1.67 at 3.3 Myr and ~ 1.25 at 5 Myr, whereas in model HDS it is ~ 1.14, ~ 1.67 and ~ 1.25, respectively, and thus the only difference between the last two models is that the transition from energy to momentum dominated regimes occurs at different times. Therefore the detailed description of these calculations is not presented in the further discussion.

6.3.3 Comparison to other models and observations

Having the exciting cluster parameters and the distribution of the ionized gas density in the surrounding shell, one can obtain the model predicted values for diagnostic parameters often used in observations and compare them to the typically observed ones. In this Section first the values of the ionization parameter are calculated and put the results onto a diagnostic diagram proposed by Yeh & Matzner (2012) which allows one to conclude if radiation or the wind dynamical pressure dominates the dynamics of the ionized gas around young stellar clusters.
The ionization parameter U is defined as the flux of ionizing photons per hydrogen atom. It is directly related to the state of ionization and to the radiation pressure over
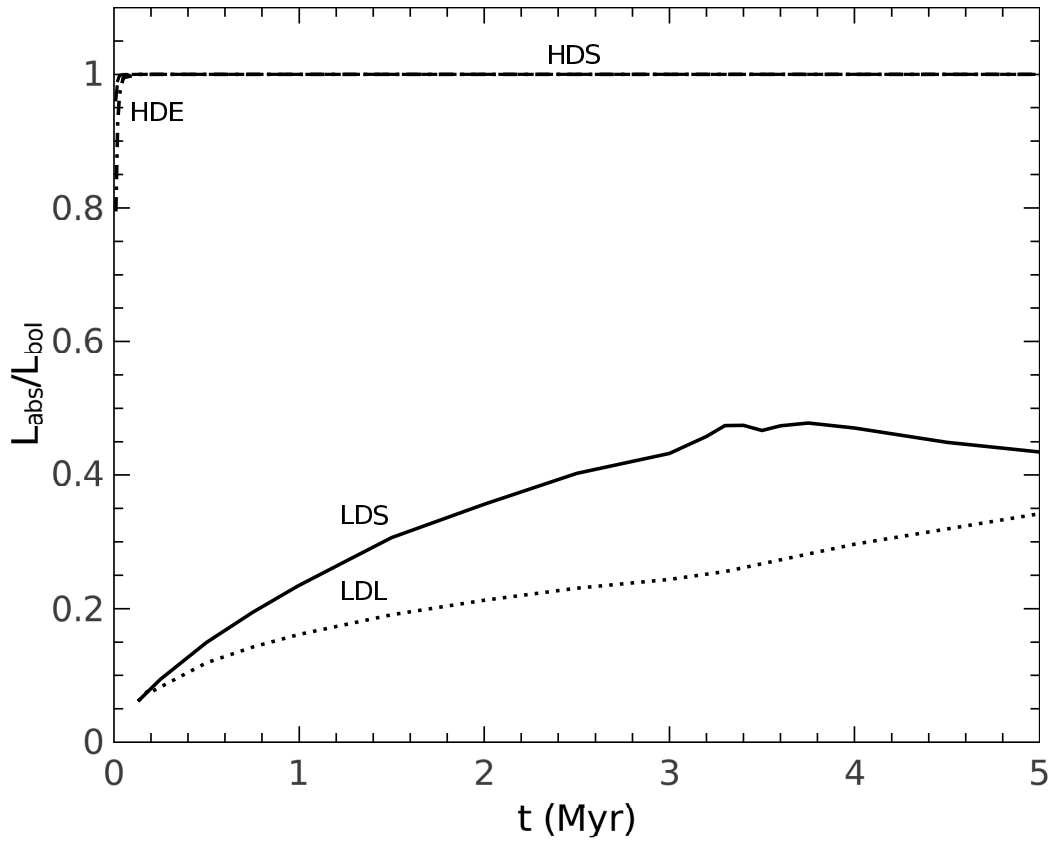
Figure 6.6: Fraction of the star cluster bolometric luminosity trapped within the shell as a function of time. The solid, dotted, dashed and dash-dotted lines display the L_{abs} over L_{bol} ratio at different evolutionary times t for models LDS, LDL, HDS and HDE, respectively. Note that dashed and dash-dotted lines overlap into a single horizontal line $L_{abs}/L_{bol} = 1$ at the earliest stages of the shell evolution.
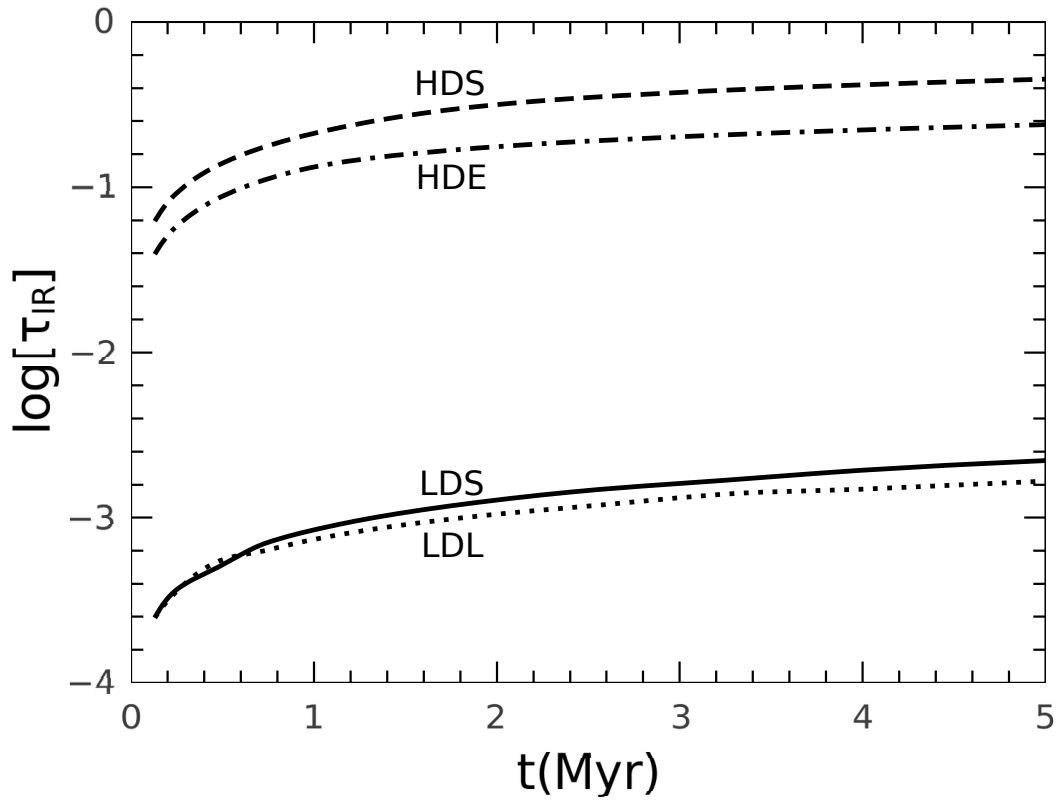
Figure 6.7: The star cluster wind-driven shell optical depth for the IR radiation as a function of time. The solid, dotted, dashed and dash-dotted lines show τ_d for models LDS, LDL, HDS and HDE, respectively.

gas thermal pressure ratio and is usually calculated at the inner edge of the ionized medium (e.g. Dopita et al., 2005):

$$U = \frac{Q_0}{4\pi n R_s^2 c} = \frac{\mu_i}{\mu_a} \frac{kT_i}{\langle h\nu \rangle_i} \frac{P_{rad}}{P_{HII}}. \tag{6.14}$$

In this approach, the presence of any neutral gas and dust able to deplete the radiation field in the free and shocked wind regions is neglected and thus it is assumed that all the photons produced by the star cluster are able to impact the shell. The ionization parameter may be measured observationally from the emission line ratios (e.g. Rigby & Rieke, 2004; Snijders et al., 2007; Yeh & Matzner, 2012, and references therein) and thus is a powerful tool to measure the relative significance of the radiation and gas thermal pressure around young stellar clusters. However, the number of ionizing photons varies radially within HII regions and therefore the measured values of U are weighted by the density distribution in the ionized nebula. This led Yeh & Matzner (2012) to propose as a relevant model parameter

$$U_w = \frac{\displaystyle\int 4\pi r^2 n^2 U(r)\mathrm{d}r}{\displaystyle\int 4\pi r^2 n^2 \mathrm{d}r}, \tag{6.15}$$

where the integrals are evaluated from the inner to the outer edge of the HII region (from R_s to R_{HII}). The models are used to obtain the ionized gas density distribution within wind-driven shells expanding into different interstellar media and the ionization parameter U_w is calculated at different times t. The results of the calculations are presented in Figure 6.8. One can note, that the time evolution of the ionization parameter U_w in the wind-driven bubble model is complicated as it depends not only on the varying incident radiation, but also on the hydrodynamics of the wind-driven shell. In all cases the value of U_w drops first as the wind-driven shell expands and the photon flux at the inner edge of the shell drops accordingly. In the standard case (LDS, solid line) the value of U_w drops continuously but turns to decrease faster after the first supernova explosion as since that time the flux of incident photons per unit area drops not only because of the shell expansion, but also because of the reduced value of Q_0. In the high density model HDS (dashed line) the value of the ionization parameter increases by about an order of magnitude after the transition to the momentum-dominated regime as when the transition occurs, the wind pressure and the ionized gas density at the inner edge of the shell drop, what enhances the value of U_w significantly (cf. equations 6.14 and 6.15). The value of the ionization parameter then remains almost constant until the first supernova explodes at about 3.3 Myr as at this stage both, the flux of ionizing photons and the ram pressure of the wind at the inner edge of the shell drop as R_s^{-2} and thus the radiation over the dynamical pressure ratio depends only on the L_{bol}/L_{SC} ratio (cf. ST13) which in the present calculations does not change much at this stage. After 3.3 Myr the value of the ionization parameter drops as the number of massive stars and

the number of available ionizing photons Q_0 decline rapidly. The behavior of U_w in the leaky (model LDL, dotted line) and low heating efficiency (model HDE, dash-dotted line) cases is very similar to that in the high density case HDS. The only difference is that the transition to the momentum-dominated regime in these cases occurs at earlier times and the maximum values of the ionization parameter are larger than that in model HDS. One can also note that the ionization parameter reaches the maximum possible value, $logU_w \approx -1.5$, in the low heating efficiency model HDL and that the model predicted values of the ionization parameter fall into the range of typical values found in local starburst galaxies: $-3 \leq logU_w \leq -1.5$, (cf. Figure 10 in Rigby & Rieke, 2004). The larger values of the ionization parameter (e.g. Snijders et al., 2007) either require a lower heating efficiency, as was also claimed in Dopita et al. (2005), or a more complicated physical model than a single ionized shell formed by a young stellar cluster (for a discussion on this issue refer to Snijders et al., 2007).

Finally, the results are placed onto a diagnostic diagram proposed by Yeh & Matzner (2012) in order to show where physically motivated models are located in this diagram. For example, their model with more than an order of magnitude increasing density (cf. Figure 7 in their paper), $L_i = 10^{42}$ erg s^{-1}, $\log \Phi = -1.09$ and $\log \Omega = -1.56$ corresponds, according to the calculations in this work, to a very compact (R_{HII} less than 3 pc) and very dense (n_s is a few hundred particles per cm^3) shell at the age of 2 Myr what implies that the HII region is quasi-static and requires a very low star cluster heating efficiency and a large confining (thermal/turbulent) pressure in the ambient ISM (cf. Silich et al., 2007, 2009; Smith et al., 2006). The two-dimensional parameter space introduced by Yeh & Matzner (2012) is related to the compactness of the HII region (parameter Ψ) and to the relative strength of different driving forces (parameter Ω). Parameter Ψ is defined as the R_{HII}/R_{ch} ratio, where R_{HII} is the radius of the ionization front (in this work this is the radius of the outer edge of the ionized shell) and R_{ch} is the radius of a uniform density Strömgren sphere whose thermal pressure is equal to the maximum possible unattenuated radiation pressure at the edge of the HII region $P_{rad} = L_{bol}/4\pi c R_{st}^2$:

$$R_{ch} = \frac{\beta_2 \mu_a^2 L_{bol}^2}{12\pi \mu_i^2 (kT_i c)^2 Q_0}. \tag{6.16}$$

Parameter Ω is related to the volume between the ionization front and the inner edge of the HII region and to the values of thermal pressure at its inner and outer edges:

$$\Omega = \frac{P_s R_s^3}{P_{edge} R_{edge}^3 - P_s R_s^3}. \tag{6.17}$$

Parameter Ω is obtained by calculating the volume between the outer and the inner edge of the ionized shell and the values of thermal pressure P_s and P_{edge} even at earlier stages of models LDS and LDL when the ionized shell is still embedded into an extended diffuse HII region. As long as the ionized shell is thin, parameter Ω is:

$$\Omega \approx 4\pi c R_s^2 P_s/L_{bol}, \tag{6.18}$$

73

and thus measures the wind dynamical over the radiation pressure ratio (the shell moves in the radiation-dominated regime if $\log \Omega < 0$ and in the wind-dominated regime if $\log \Omega > 0$). In all static models discussed in Section 6.1 the parameter Ω is very small
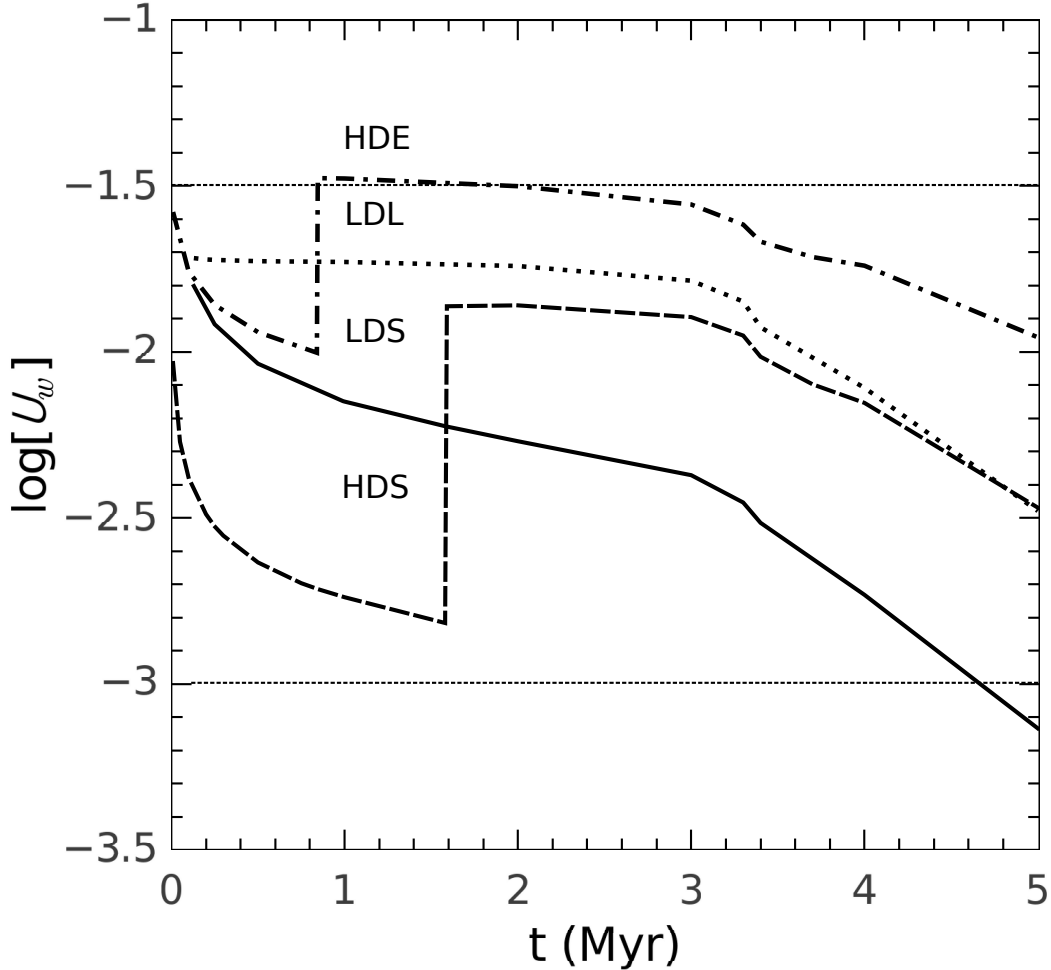

Figure 6.8: The ionization parameter time evolution. The solid, dotted, dashed and dash-dotted lines correspond to models LDS, LDL, HDS and HDE, respectively (cf. Table 6.2). The horizontal lines display the range of typical values for the ionization parameter found in local starburst galaxies (cf. Rigby & Rieke, 2004).

($\log \Omega \sim -15$) what implies that radiation pressure controls the ionized gas distribution in all static configurations with low-pressure central cavities. In the wind-blown cases the parameter Ψ is a function of time as both radii, R_{HII} and R_{ch}, change with time. Therefore it is instructive to show first how parameter Ω changes with time. This is shown in Figure 6.9 , panel a. Panel b in this figure displays the evolutionary tracks of the wind-driven shell models in the $\Omega - \Psi$ parameter space. The initial points for models LDS, LDL, HDS and HDE were calculated at the star cluster age of 0.13 Myr. The initial values of the normalization radius R_{ch} then are: ~ 72 pc in model LDL and

~ 70 pc in models LDS, HDS and HDE, respectively. As both star cluster parameters, L_{bol} and Q_0, change with time, the value of R_{ch} also changes with time significantly and by 10 Myr reaches ≈ 720 pc. In cases LDS and LDL parameter Ω grows continuously (cf. panel a, solid and dotted lines). In the high density cases parameter Ω drops drastically when the transition occurs to the momentum dominated regime, then slightly declines and increases again after the first supernova explosion as the number of the ionizing photons then drops rapidly. The strong time evolution of R_{ch} leads to the intricate tracks of the ionized shells in the $\log\Omega - \log\Psi$ diagram (cf. panel b). In the low density models LDS and LDL the tracks go to the left and up because the normalization radius R_{ch} grows with time faster than the radius of the shell and thus the ionization front radius R_{HII}. In the high density cases HDS and HDE the tracks are more intricate. They first go to the right, then drop down when the transition to the momentum dominated regime occurs, make a loop and finally go back to the left and up.

Thus, in the low density cases the impact of radiation pressure on the shell dynamics is always negligible and declines with time. In the high density model HDS the contribution of radiation pressure to the shell dynamics becomes more significant when the shell makes a transition from the energy to the momentum dominated regime. However, in this case parameter $\log\Omega$ also remains positive and thus in all models with a 100% heating efficiency the shells expand in the wind-dominated regime. Parameter $\log\Omega$ falls below a zero value only in the low heating efficiency case HDE. Thus, only in this case radiation pressure may dominate the shell dynamics. The radiation dominated phase lasts from the beginning of the momentum dominated regime at ~ 0.85 Myr till ~ 7.36 Myr (cf. panel a). This implies that radiation pressure may dominate the dynamics of the gas around young stellar clusters either at early stages of evolution (before ~ 3 Myr) or if the major fraction of the star cluster mechanical luminosity is dissipated or radiated away within the star cluster volume and thus the energy of the star cluster driven winds is significantly smaller than what star cluster synthetic models predict. However, even if this is the case, radiation pressure will dominate only if the exciting cluster is embedded into a high density ambient medium.

6.4 Conclusions

Radiation pressure may strongly affect the structure of static, dusty HII regions. However, the impact that star cluster winds provide on the flows and the strong time evolution of the ionizing photon flux and the star cluster bolometric luminosity lead to a more intricate picture. In a more realistic model, the impact of radiation pressure on the expanding shell crucially depends on the strength of the star cluster wind at the inner edge of the shell and thus on the hydrodynamic regime of the shell expansion and on the star cluster age and heating efficiency.

Radiation pressure may affect the inner structure and the dynamics of the wind-driven shell only at the earliest stages of evolution (before ~ 3 Myr, when the L_{bol} over L_{SC}
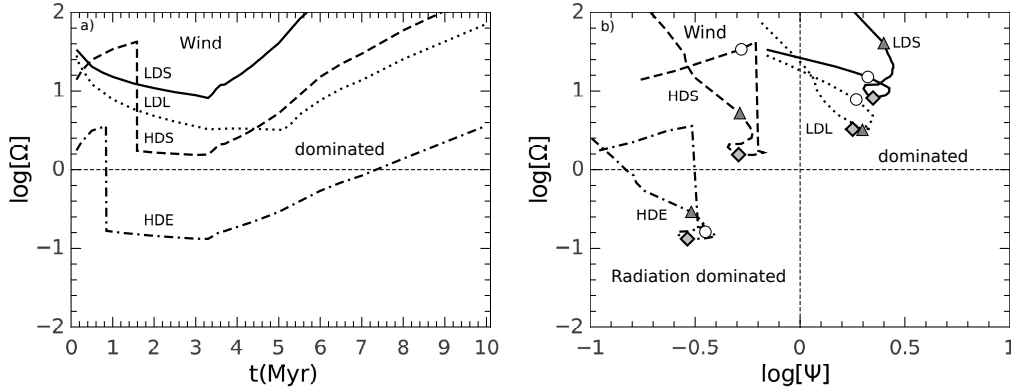
Figure 6.9: Evolutionary tracks of the expanding ionized shells in the diagnostic parameter space. The evolution of the diagnostic parameter Ω (cf. text) is presented in panel a. Panel b displays the location of the expanding shell exposed to the radiation from the central cluster in the $\log\Omega - \log\Psi$ diagram at different times t. The solid, dotted, dashed and dash-dotted lines correspond to models LDS, LDL, HDS and HDE, respectively. The circles, diamonds and triangles mark the evolutionary times of 1 Myr, 3.3 Myr and 5 Myr, respectively. Note that shells with values of $\log\Omega$ above the horizontal dotted lines in both panels are wind dominated; while shells with values of $\log\Omega$ below the horizontal dotted line in panel b are radiation dominated.

ratio is still larger than that used in the present calculations), or if a major fraction of the star cluster mechanical luminosity is dissipated or radiated away within the star cluster volume and thus the star cluster mechanical energy output is much smaller than what star cluster synthetic models predict. However, even in these cases, radiation effects may be significant only if the exciting cluster is embedded into a high density ambient medium.

The impact that radiation pressure provides on the dynamics and inner structure of the wind-driven shell is always negligible during the advanced stages of evolution, as the radiation energy flux declines rapidly after the first supernovae explosion, whereas the mechanical power of the cluster does not.

The calculated values of the density weighted ionization parameter U_w fall into the range of typical values found in nearby starburst galaxies ($-3 \leq \log U_w \leq -1.5$). The larger values of the ionization parameter sometimes detected around very young stellar clusters require either a lower heating efficiency, or a more complicated than a single ionized shell physical model.

The model location in the $\log\Omega - \log\Psi$ diagnostic diagram which was proposed by Yeh & Matzner (2012) strongly depends on the evolutionary time t what leads to intricate evolutionary track patterns. The standard wind-driven and leaky bubble model are located in the upper segments in this diagram where HII regions evolving in the thermal pressure dominated regime settle in. The only evolutionary track that temporarily passes through the lower left corner, where radiation-pressure-dominated HII regions are located, is that resulting from calculations with a low heating efficiency.

The results obtained in this Chapter are published in the paper Martínez-González et al. (2014).

Chapter 7

Concluding Remarks

This work has been devoted to elucidate the impact that the presence of dust grains have on (1) the hydrodynamics and observational manifestations of the matter reinserted via stellar winds and supernovae explosions within young and massive star clusters, and (2) on the dynamics and inner structure of wind-blown shells.

For the first part, a self-consistent semi-analytic model was developed for the winds driven by stellar clusters which follow different cases of the generalized Schuster stellar density distribution. In this approach, besides the cooling from a gas in collisional ionization equilibrium, the contribution to the cooling law from dust-induced cooling, via gas-grain collisions, was carefully considered following the prescriptions given by Dwek (1987).

In such clusters, a steeper stellar density distribution, a higher value of the dust-to-gas mass ratio and distribution of dust sizes giving more weight to small grains, strongly increase the fraction of the mechanical energy that is radiated away and thus lowers the location of the critical line which separates stationary from thermally unstable winds in the L_{SC} *vs.* R_{SC} diagram. For example, star clusters with a Schuster profile with a realistic index $\beta = 1.5$, a dust-to-gas mass ratio $Z_d = 10^{-3}$ and a MRN size distribution with lower and upper limits 0.001 μm and 0.5 μm, respectively, and a mass $< 10^6$ M$_\odot$, would experience the bimodal regime in which thermal instabilities lead to clump formation and eventually could form new stellar generations.

As one approaches the critical line, the distribution of the hydrodynamic variables (flow velocity, temperature and density) changes radically, in particular, they experience a rapid decay in temperature near the sonic point, consequently not presenting an extended X-ray free wind region but instead a recombining region and, given the ample supply of UV photons, a re-ionized region, rapidly expanding close to the sonic point (which may coincide with the star cluster edge). This results, when applied to the exciting cluster of the blue compact dwarf *PHL 293B*, successfully explain the high velocity blue-shifted absorption features observed in its optical spectra, as well as provide estimates of its ionized and neutral gas column densities and diffuse X-ray emission in good agreement with the observed values.

Next, the theory of stochastic dust temperature fluctuations, also prescribed by Dwek

(1986), was combined with the theory of stochastic dust injection by supernovae and the hydrodynamic dusty model to present the spectral energy distributions which are to be expected from the interiors of super stellar clusters. These calculations have shown that star clusters evolving closer to the critical line (i.e. with larger values of the star cluster mechanical luminosity) lead to an enhanced dust emission. The opposite situation occurs with more extended star clusters and larger adiabatic terminal speeds, which lead to a decrease in their dust emission. The combined action of multiple central clusters, can be the key to explain the near-infrared excesses observed in bright young clusters, as in the case of the blue compact dwarfs *IZw18*, *SBS 0335-052E*, *Henize 2-10* and *NGC 5233*. This issue will be addressed in the near future.

Last but not least, for the second part, I addressed the effects that radiation pressure, acting on dust grains and recombining atoms, has on the distribution of density and thermal pressure within wind-blown shells and thus how it may affect the velocity of the outer shock and the dynamics of the ionized gas around young stellar clusters. The main conclusion drawn from this analysis is that radiation pressure may affect the inner structure and the dynamics of the wind-driven shell only at the earliest stages of evolution (before ~ 3 Myr, or if a major fraction of the star cluster mechanical luminosity is dissipated or radiated away within the star cluster volume and thus the star cluster mechanical energy output is much smaller than what star cluster synthetic models predict. However, even in these cases, radiation effects may be significant only if the exciting cluster is embedded into a high density ambient medium. This situation is what occurs in the strongly radiative dusty models described in the first part of the thesis, however, a more careful treatment on the fraction of the ionizing and non-ionizing radiation absorbed within the free-wind region is needed, which I also plan to address. These models also predict values for the density weighted ionization parameter, U_w, which fall into the range of typical values found in nearby starburst galaxies ($-3 \leq \log U_w \leq -1.5$).

There is a vast number of possible applications to the interplay between the theory of dust-induced cooling and stochastic dust temperature fluctuations and the application of hydrodynamic models to, for example, blue compact dwarfs like *PHL 293B*, *IZw18* and *SBS 0335-052E*, and stellar systems with extreme star formation rates, like the SCUBA galaxies. Also, the consideration of the absorption of ionizing photons by dust grains as a heating source for dust could be an important effect to consider when the ionizing flux from the star cluster is strong.

In summary, this work offers a set of predictions and/or explanations for the observational manifestations of young dusty star clusters; these include the ionization parameter associated to the shells surrounding them, infrared spectral energy distributions, infrared luminosities, the optical depth for the IR radiation, the blue-shifted weak narrow absorptions features in the hydrogen recombination lines in the optical spectra of *PHL 293B*, a quantification of the outward flux of (ultraviolet) ionizing photons and X-ray luminosities.

Appendix A

Dust Cooling Calculations

This Appendix provides tables which contain the results of the calculations of the dust cooling function for different grain size distributions as a function of the gas temperature and normalized to the dust-to-gas mass ratio, for a_{min} set to 0.001 μm and different a_{max} values (Table A.1), and for a_{max} set to 0.5 μm and different a_{min} values (Table A.2).

Table A.1: The Cooling Function with different grain size distribution (with $a_{min} = 0.001$ μm in all cases) normalized to the dust-to-gas mass ratio.

a_{max} (μm)	0.001	0.002	0.005	0.01	0.05	0.1	0.5
T (K)	Λ_d/Z_d (erg s^{-1} cm^3)						
1.00E+04	8.787E-22	6.213E-22	3.930E-22	2.778E-22	1.234E-22	8.606E-23	3.565E-23
1.25E+04	1.256E-21	8.884E-22	5.619E-22	3.973E-22	1.774E-22	1.252E-22	5.702E-23
1.57E+04	1.763E-21	1.246E-21	7.883E-22	5.574E-22	2.490E-22	1.756E-22	8.000E-23
1.97E+04	2.473E-21	1.749E-21	1.106E-21	7.821E-22	3.493E-22	2.464E-22	1.122E-22
2.47E+04	3.470E-21	2.453E-21	1.552E-21	1.097E-21	4.900E-22	3.457E-22	1.575E-22
3.09E+04	4.868E-21	3.442E-21	2.177E-21	1.539E-21	6.875E-22	4.850E-22	2.209E-22
3.87E+04	6.830E-21	4.830E-21	3.054E-21	2.160E-21	9.646E-22	6.805E-22	3.100E-22
4.86E+04	9.583E-21	6.776E-21	4.286E-21	3.030E-21	1.353E-21	9.547E-22	4.349E-22
6.09E+04	1.344E-20	9.507E-21	6.013E-21	4.251E-21	1.899E-21	1.339E-21	6.102E-22
7.63E+04	1.886E-20	1.334E-20	8.436E-21	5.965E-21	2.664E-21	1.879E-21	8.561E-22
9.56E+04	2.646E-20	1.871E-20	1.184E-20	8.369E-21	3.737E-21	2.637E-21	1.201E-21
1.20E+05	3.713E-20	2.625E-20	1.660E-20	1.174E-20	5.244E-21	3.699E-21	1.685E-21
1.50E+05	5.209E-20	3.683E-20	2.330E-20	1.647E-20	7.357E-21	5.190E-21	2.364E-21
1.88E+05	7.308E-20	5.168E-20	3.269E-20	2.311E-20	1.032E-20	7.282E-21	3.317E-21
2.36E+05	1.025E-19	7.250E-20	4.586E-20	3.242E-20	1.448E-20	1.022E-20	4.653E-21
2.96E+05	1.434E-19	1.017E-19	6.431E-20	4.548E-20	2.031E-20	1.433E-20	6.524E-21
3.70E+05	1.995E-19	1.422E-19	9.010E-20	6.373E-20	2.847E-20	2.008E-20	9.132E-21
4.64E+05	2.737E-19	1.978E-19	1.258E-19	8.907E-20	3.981E-20	2.807E-20	1.274E-20
5.82E+05	3.672E-19	2.716E-19	1.744E-19	1.238E-19	5.540E-20	3.907E-20	1.767E-20
7.29E+05	4.773E-19	3.651E-19	2.389E-19	1.703E-19	7.650E-20	5.395E-20	2.428E-20
9.14E+05	5.998E-19	4.772E-19	3.213E-19	2.310E-19	1.045E-19	7.370E-20	3.300E-20
1.15E+06	7.272E-19	6.032E-19	4.223E-19	3.077E-19	1.406E-19	9.932E-20	4.426E-20
1.44E+06	8.536E-19	7.363E-19	5.399E-19	4.012E-19	1.863E-19	1.319E-19	5.851E-20
1.80E+06	9.735E-19	8.691E-19	6.701E-19	5.109E-19	2.428E-19	1.724E-19	7.629E-20
2.25E+06	1.080E-18	9.951E-19	8.063E-19	6.342E-19	3.111E-19	2.218E-19	9.808E-20
2.82E+06	1.176E-18	1.110E-18	9.415E-19	7.667E-19	3.918E-19	2.810E-19	1.244E-19
3.54E+06	1.264E-18	1.209E-18	1.068E-18	9.016E-19	4.850E-19	3.508E-19	1.561E-19
4.44E+06	1.329E-18	1.296E-18	1.183E-18	1.033E-18	5.902E-19	4.316E-19	1.933E-19
5.56E+06	1.383E-18	1.365E-18	1.280E-18	1.153E-18	7.051E-19	5.232E-19	2.371E-19
6.97E+06	1.447E-18	1.419E-18	1.360E-18	1.258E-18	8.264E-19	6.248E-19	2.879E-19
8.73E+06	1.485E-18	1.469E-18	1.425E-18	1.346E-18	9.494E-19	7.345E-19	3.459E-19
1.09E+07	1.498E-18	1.508E-18	1.473E-18	1.415E-18	1.067E-18	8.484E-19	4.117E-19
1.37E+07	1.506E-18	1.522E-18	1.505E-18	1.465E-18	1.174E-18	9.614E-19	4.849E-19
1.72E+07	1.508E-18	1.520E-18	1.523E-18	1.497E-18	1.265E-18	1.068E-18	5.646E-19
2.15E+07	1.505E-18	1.514E-18	1.532E-18	1.516E-18	1.336E-18	1.161E-18	6.494E-19
2.70E+07	1.497E-18	1.503E-18	1.524E-18	1.518E-18	1.387E-18	1.238E-18	7.367E-19
3.38E+07	1.483E-18	1.488E-18	1.502E-18	1.514E-18	1.419E-18	1.297E-18	8.224E-19
4.24E+07	1.464E-18	1.468E-18	1.478E-18	1.496E-18	1.434E-18	1.336E-18	9.022E-19
5.31E+07	1.441E-18	1.444E-18	1.451E-18	1.463E-18	1.434E-18	1.357E-18	9.716E-19
6.66E+07	1.414E-18	1.416E-18	1.421E-18	1.429E-18	1.422E-18	1.363E-18	1.027E-18
8.35E+07	1.384E-18	1.385E-18	1.389E-18	1.394E-18	1.400E-18	1.356E-18	1.068E-18
1.05E+08	1.352E-18	1.353E-18	1.355E-18	1.359E-18	1.375E-18	1.340E-18	1.095E-18
1.31E+08	1.319E-18	1.319E-18	1.321E-18	1.324E-18	1.339E-18	1.315E-18	1.109E-18
1.64E+08	1.286E-18	1.286E-18	1.287E-18	1.289E-18	1.295E-18	1.290E-18	1.113E-18
2.06E+08	1.253E-18	1.254E-18	1.254E-18	1.256E-18	1.258E-18	1.257E-18	1.110E-18
2.58E+08	1.224E-18	1.224E-18	1.224E-18	1.225E-18	1.225E-18	1.219E-18	1.106E-18
3.23E+08	1.197E-18	1.197E-18	1.198E-18	1.198E-18	1.197E-18	1.190E-18	1.097E-18
4.05E+08	1.176E-18	1.176E-18	1.176E-18	1.176E-18	1.175E-18	1.167E-18	1.095E-18
5.08E+08	1.160E-18	1.160E-18	1.160E-18	1.160E-18	1.159E-18	1.153E-18	1.094E-18
6.37E+08	1.151E-18	1.152E-18	1.152E-18	1.152E-18	1.151E-18	1.145E-18	1.090E-18
7.98E+08	1.151E-18	1.151E-18	1.151E-18	1.152E-18	1.151E-18	1.147E-18	1.099E-18

Table A.2: The Cooling Function with different grain size distribution (with $a_{max} = 0.5$ μm in all cases) normalized to the dust-to-gas mass ratio.

a_{min} (μm)	0.001	0.002	0.005	0.01	0.05	0.1	0.5
T (K)	Λ_d/Z_d (erg s^{-1} cm^3)						
1.00E+04	3.565E-23	2.625E-23	1.721E-23	1.234E-23	5.556E-24	3.930E-24	1.757E-24
1.25E+04	5.702E-23	3.959E-23	2.504E-23	1.774E-23	7.946E-24	5.619E-24	2.513E-24
1.57E+04	8.000E-23	5.555E-23	3.513E-23	2.489E-23	1.115E-23	7.883E-24	3.525E-24
1.97E+04	1.122E-22	7.794E-23	4.928E-23	3.493E-23	1.564E-23	1.106E-23	4.946E-24
2.47E+04	1.575E-22	1.093E-22	6.914E-23	4.900E-23	2.195E-23	1.552E-23	6.940E-24
3.09E+04	2.209E-22	1.534E-22	9.701E-23	6.875E-23	3.079E-23	2.177E-23	9.736E-24
3.87E+04	3.100E-22	2.152E-22	1.361E-22	9.646E-23	4.320E-23	3.055E-23	1.366E-23
4.86E+04	4.349E-22	3.020E-22	1.910E-22	1.353E-22	6.061E-23	4.286E-23	1.917E-23
6.09E+04	6.102E-22	4.237E-22	2.679E-22	1.899E-22	8.503E-23	6.012E-23	2.689E-23
7.63E+04	8.561E-22	5.944E-22	3.759E-22	2.664E-22	1.193E-22	8.436E-23	3.773E-23
9.56E+04	1.201E-21	8.340E-22	5.273E-22	3.738E-22	1.674E-22	1.183E-22	5.293E-23
1.20E+05	1.685E-21	1.170E-21	7.399E-22	5.244E-22	2.348E-22	1.661E-22	7.426E-23
1.50E+05	2.364E-21	1.642E-21	1.038E-21	7.357E-22	3.295E-22	2.330E-22	1.042E-22
1.88E+05	3.317E-21	2.303E-21	1.456E-21	1.032E-21	4.622E-22	3.268E-22	1.462E-22
2.36E+05	4.653E-21	3.231E-21	2.043E-21	1.448E-21	6.485E-22	4.586E-22	2.051E-22
2.96E+05	6.524E-21	4.533E-21	2.867E-21	2.032E-21	9.099E-22	6.434E-22	2.877E-22
3.70E+05	9.132E-21	6.360E-21	4.022E-21	2.851E-21	1.276E-21	9.027E-22	4.037E-22
4.64E+05	1.274E-20	8.922E-21	5.643E-21	3.999E-21	1.791E-21	1.266E-21	5.664E-22
5.82E+05	1.767E-20	1.251E-20	7.917E-21	5.611E-21	2.513E-21	1.777E-21	7.946E-22
7.29E+05	2.428E-20	1.751E-20	1.111E-20	7.872E-21	3.525E-21	2.493E-21	1.115E-21
9.14E+05	3.300E-20	2.441E-20	1.558E-20	1.105E-20	4.946E-21	3.497E-21	1.564E-21
1.15E+06	4.426E-20	3.380E-20	2.185E-20	1.550E-20	6.940E-21	4.907E-21	2.195E-21
1.44E+06	5.851E-20	4.632E-20	3.060E-20	2.174E-20	9.736E-21	6.885E-21	3.079E-21
1.80E+06	7.629E-20	6.266E-20	4.270E-20	3.049E-20	1.366E-20	9.659E-21	4.320E-21
2.25E+06	9.808E-20	8.350E-20	5.918E-20	4.271E-20	1.916E-20	1.355E-20	6.061E-21
2.82E+06	1.244E-19	1.095E-19	8.113E-20	5.963E-20	2.689E-20	1.901E-20	8.503E-21
3.54E+06	1.561E-19	1.413E-19	1.097E-19	8.271E-20	3.772E-20	2.668E-20	1.193E-20
4.44E+06	1.933E-19	1.796E-19	1.458E-19	1.135E-19	5.292E-20	3.743E-20	1.674E-20
5.56E+06	2.371E-19	2.251E-19	1.903E-19	1.534E-19	7.420E-20	5.251E-20	2.348E-20
6.97E+06	2.879E-19	2.782E-19	2.439E-19	2.036E-19	1.038E-19	7.366E-20	3.295E-20
8.73E+06	3.459E-19	3.394E-19	3.071E-19	2.649E-19	1.444E-19	1.032E-19	4.622E-20
1.09E+07	4.117E-19	4.088E-19	3.799E-19	3.376E-19	1.988E-19	1.443E-19	6.485E-20
1.37E+07	4.849E-19	4.865E-19	4.621E-19	4.214E-19	2.691E-19	2.001E-19	9.098E-20
1.72E+07	5.646E-19	5.716E-19	5.527E-19	5.152E-19	3.561E-19	2.736E-19	1.276E-19
2.15E+07	6.494E-19	6.621E-19	6.495E-19	6.166E-19	4.583E-19	3.659E-19	1.783E-19
2.70E+07	7.367E-19	7.551E-19	7.499E-19	7.223E-19	5.719E-19	4.746E-19	2.470E-19
3.38E+07	8.224E-19	8.465E-19	8.491E-19	8.266E-19	6.905E-19	5.940E-19	3.354E-19
4.24E+07	9.022E-19	9.315E-19	9.413E-19	9.247E-19	8.060E-19	7.157E-19	4.413E-19
5.31E+07	9.716E-19	1.005E-18	1.021E-18	1.011E-18	9.110E-19	8.300E-19	5.572E-19
6.66E+07	1.027E-18	1.064E-18	1.086E-18	1.081E-18	9.989E-19	9.287E-19	6.724E-19
8.35E+07	1.068E-18	1.107E-18	1.132E-18	1.132E-18	1.067E-18	1.008E-18	7.781E-19
1.05E+08	1.095E-18	1.135E-18	1.162E-18	1.165E-18	1.113E-18	1.065E-18	8.625E-19
1.31E+08	1.109E-18	1.149E-18	1.177E-18	1.182E-18	1.144E-18	1.103E-18	9.281E-19
1.64E+08	1.113E-18	1.152E-18	1.180E-18	1.186E-18	1.161E-18	1.122E-18	9.670E-19
2.06E+08	1.110E-18	1.147E-18	1.174E-18	1.180E-18	1.164E-18	1.133E-18	9.946E-19
2.58E+08	1.106E-18	1.140E-18	1.166E-18	1.173E-18	1.163E-18	1.144E-18	1.023E-18
3.23E+08	1.097E-18	1.129E-18	1.152E-18	1.158E-18	1.151E-18	1.139E-18	1.018E-18
4.05E+08	1.095E-18	1.124E-18	1.144E-18	1.150E-18	1.147E-18	1.140E-18	1.023E-18
5.08E+08	1.094E-18	1.118E-18	1.137E-18	1.142E-18	1.139E-18	1.134E-18	1.074E-18
6.37E+08	1.090E-18	1.110E-18	1.125E-18	1.129E-18	1.124E-18	1.118E-18	1.080E-18
7.98E+08	1.099E-18	1.116E-18	1.127E-18	1.129E-18	1.124E-18	1.118E-18	1.071E-18

Appendix B

Boundary Conditions for the Solution of the Hydrodynamic Equations

The boundary conditions which allow one to select the wind solution from the infinite number of integral curves is that the integral curve must pass through the singular point. The derivative of the expansion velocity at the singular point must be positive (Lamers & Cassinelli, 1999). The denominator in equation (3.13) vanishes when the wind velocity reaches the local sound speed and thus: $u_{sp} = c_{sp}$, i.e. the sonic point coincides with the singular point. The density at the singular point (cf. equation 3.15) then is:

$$\rho_{sp} = \frac{q_{m0}R_{sp}}{3u_{sp}}F_\beta(R_{sp}) \tag{B.1}$$

The second condition, that the numerator in equation (3.13) vanishes, then yields:

$$c_{sp}^4 - 2F_1(R_{sp})c_{sp}^2 + F_2(R_{sp})\Lambda = 0\,, \tag{B.2}$$

where functions F_1 and F_2 are:

$$F_1 = \frac{(\gamma - 1)q_e}{F_3}\,, \tag{B.3}$$

$$F_2 = \frac{2\left[q_{m0}R_cF_\beta(R_{sp})\right]^2}{\mu_i^2 F_3}\left(\frac{R_c}{R_{sp}}\right)^4\,, \tag{B.4}$$

and

$$F_3 = 4q_{m0}F_\beta(R_{sp})\left(\frac{R_c}{R_{sp}}\right)^3 - (\gamma + 1)q_m\,, \tag{B.5}$$

This nonlinear algebraic equation defines the temperature at the singular point, T_{sp}, if R_{sp} is known. One can present equation (B.2) in the dimensionless form:

85

$$\Phi = c_{sp}^4 - 2F_1(R_{sp})c_{sp}^2 + F_2(R_{sp})\Lambda(T_{sp}, Z) = 0. \tag{B.6}$$

and then solve it numerically. Equation (B.6) may have one, two, or have complex roots; the proper solution of equation (B.6) is obtained from an outward integration from the star cluster center and an inward integration from the singular point, then the two integrations must match at an intermediate radius: $0 < R_{fit} < R_{sp}$. The value of the singular radius, R_{sp}, is obtained by iterations, as explained in Section 3.4.

Having obtained the value of T_{sp}, one can obtain the wind velocity at the singular point, which is: $u_{sp} = c_{sp}$. The density in the singular point yields from equation (B.1), the pressure then is: $P_{sp} = \rho_{sp}c_{sp}^2/\gamma$.

Thus, one can obtain the values of all hydrodynamic variables at the singular point solving the nonlinear algebraic equation (B.6).

The derivative of the wind velocity at the singular point must be obtained by applying the L'Hôpital's Rule. The derivatives of numerator and denominator of equation (3.13) over radius are:

$$\frac{\mathrm{d}N}{\mathrm{d}r} = \frac{\partial N}{\partial r} + \frac{\partial N}{\partial u}\frac{\mathrm{d}u}{\mathrm{d}r} + \frac{\partial N}{\partial c^2}\frac{\mathrm{d}c^2}{\mathrm{d}r} + \frac{\partial N}{\partial T}\frac{\mathrm{d}T}{\mathrm{d}r} + \frac{\partial N}{\partial \rho}\frac{\mathrm{d}\rho}{\mathrm{d}r} = F_5\frac{\mathrm{d}u}{\mathrm{d}r} + F_6 + \frac{\partial N}{\partial r}, \tag{B.7}$$

$$\frac{\mathrm{d}D}{\mathrm{d}r} = \frac{\partial D}{\partial u}\frac{\mathrm{d}u}{\mathrm{d}r} + \frac{\partial D}{\partial c^2}\frac{\mathrm{d}c^2}{\mathrm{d}r} = -(\gamma + 1)c\left(\frac{\mathrm{d}u}{\mathrm{d}r} + \frac{q_m}{\rho}\right) + \frac{2c^2}{r}, \tag{B.8}$$

where functions N, D, $\partial N/\partial r$, F_5 and F_6 are:

$$N(r, u, \rho, c, T) = (\gamma - 1)(q_e - Q) + (\gamma + 1)q_m u^2/2 - 2c^2\rho u/r, \tag{B.9}$$

$$D(u, c) = c^2 - u^2 \tag{B.10}$$

$$\frac{\partial N}{\partial r} = -\frac{\beta}{r}\left(\frac{r}{R_c}\right)^2\left[\frac{(2(\gamma - 1)q_e + (1 + \gamma)q_m c^2}{[1 + (r/R_c)^2]}\right]$$
$$+ \quad \frac{2q_{m0}c^2}{r}\left(\frac{R_c}{r}\right)^3\left[3F_\beta(r) - \frac{(r/R_c)^3}{[1 + (r/R_c)^2]^\beta}\right], \tag{B.11}$$

$$F_5 = (1 - \gamma)cF_4 + (1 + \gamma)q_m c + \frac{2(\gamma - 1)\rho^2\Lambda}{c\mu_i^2} \tag{B.12}$$

$$F_6 = \frac{2(\gamma - 1)\Lambda\rho^2}{\mu_i^2 c}\left(\frac{2c}{r} - \frac{q_m}{\rho}\right) - \left[\frac{(\gamma + 1)q_m c}{\rho} - \frac{2c^2}{r}\right]F_4, \tag{B.13}$$

and

$$F_4 = \frac{(1 - \gamma)}{\gamma}\mu_a\frac{n^2}{k_B}\frac{\partial\Lambda}{\partial T} - 2q_{m0}F_\beta(r)\left(\frac{R_c}{r}\right)^3. \tag{B.14}$$

86

One can obtain then the derivative of the wind velocity (and thus the derivative of the thermal pressure) at the singular point substituting relations (B.7) and (B.8) into equation (3.13) and keeping in mind that at the singular point $u_{sp} = c_{sp}$. This leads to a quadratic algebraic equation:

$$\left(\frac{\mathrm{d}u}{\mathrm{d}r}\right)^2 - 2F_7\frac{\mathrm{d}u}{\mathrm{d}r} + F_8 = 0\,, \tag{B.15}$$

where functions F_7 and F_8 are:

$$F_7 = \left[2\rho c^2/r - (\gamma+1)cq_m - F_5\right]/2(\gamma+1)c\rho\,, \tag{B.16}$$

$$F_8 = [F_6 + \partial N/\partial r]/[(\gamma+1)c\rho]\,. \tag{B.17}$$

The root of equation (B.15), which results into positive derivative of the wind velocity at the singular point, is used in the calculations.

87

Appendix C

Shells driven by less massive star clusters

In order to complement the results obtained in Chapter 6, in this appendix two extra models are discussed. The model parameters are summarized in Table C.1. Model VHDL considers a young massive (10^5 M$_\odot$) star clusters embedded into a very high density ISM ($n_{ISM} = 10^4$ cm^{-3}) with temperature $T_{ISM} = 100$ K.

Table C.1: Additional wind-driven shell models

Models	L_{SC}	n_{ISM}	Z_{ISM}	t	Regime
	erg s^{-1}	cm^{-3}	$Z_\odot$	Myr	
VHDL a, b	10^{39}	10^4	0.4	1, 3.3	Very high density leaky/momentum-dominated
VHDE a, b	10^{39}	10^4	0.4	1, 3.3	Very high density with low heating efficiency

Figure C.1 presents the results of the calculations for two cases. In case VHDL (the left-hand panels in the Figure, the shell expansion begins in the energy-dominated regime. However the transition to the momentum-driven regime then occurs rapidly (at ~ 0.16 Myr) either due to strong radiative losses of energy in the shocked wind region or due to the gas leakage though the holes in the shell provided by multiple impacts with clumps in the surrounding ISM as suggested in the leaky bubble model (Matzner, 2002). Solid, dashed and dotted lines show the calculated density, thermal and ram pressure profiles in and around the wind-driven shell. The upper and middle panels on the right-hand column present the results of the calculations in the case with a low heating efficiency (model VHDE).

In this case the values of L_i, L_n and Q_0 are kept equal to those predicted by the Starburst99 synthetic model, but instead of using the average mechanical luminosity ($L_{SC} = 10^{39}$ erg s^{-1}) predicted by the synthetic model, an order of magnitude smaller $L_{SC} = 10^{38}$ erg s^{-1} was considered. The resultant expanding shell is dense and cools down rapidly in both calculations. The inner edge of this shell coincides with the contact discontinuity. Here the density jumps from a low value in the shocked wind zone where the gas temperature is large to the much larger value in the ionized shell with
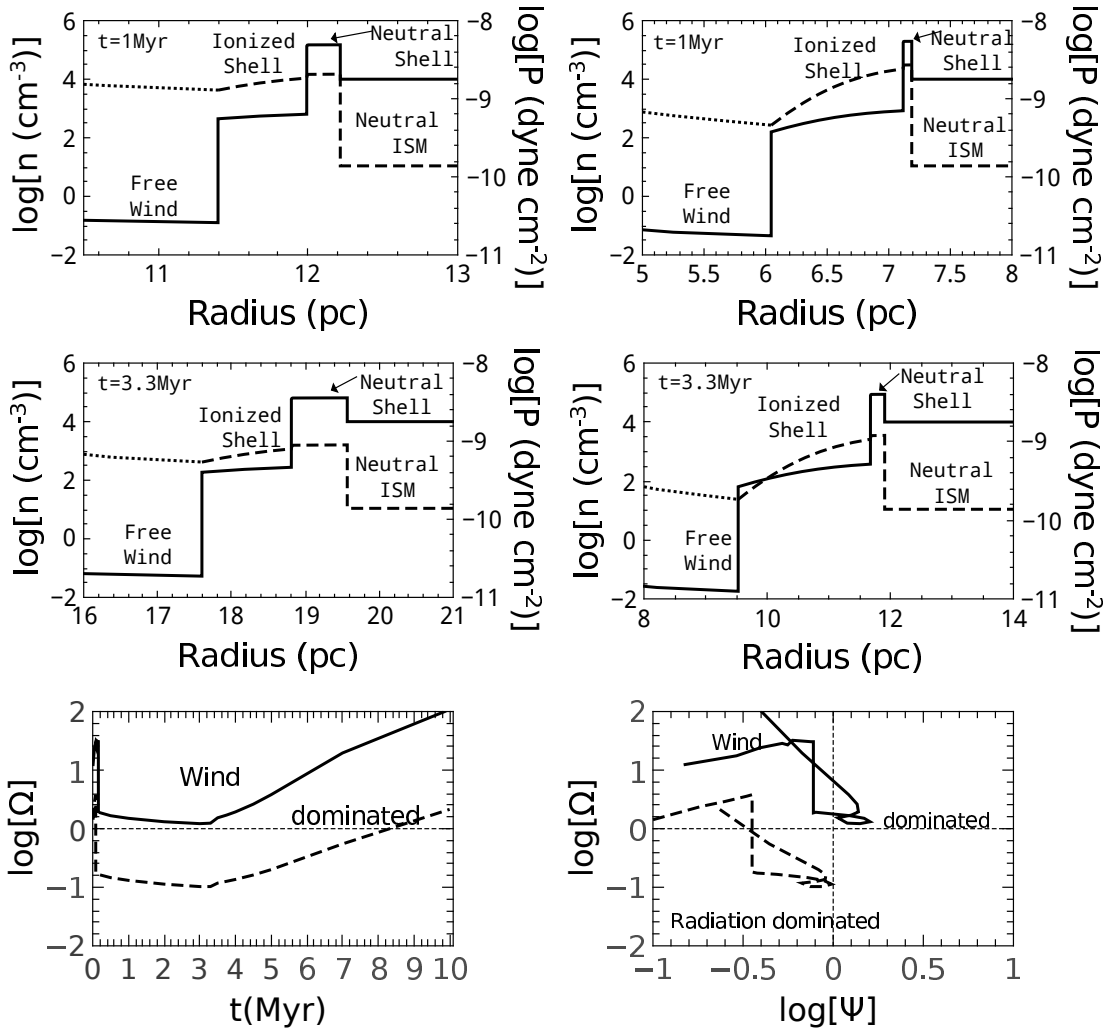
Figure C.1: The distribution of density and thermal pressure in the wind-blown shell exposed to the radiation from the central cluster. The left-hand column presents the results for the leaky/momentum-dominated model VHDL. The right-hand column displays the results for model VHDE with a low cluster heating efficiency. Solid lines correspond to the radial density distribution. Long-dashed and dotted lines show the distribution of thermal and ram pressure, respectively. The bottom panels display the evolutionary tracks of model VHDL (solid lines) and VHDE (dashed lines) on the diagnostic diagram which allows to discriminate between the thermal and radiation pressure dominated regimes.

a much lower (10^4K) temperature whereas the thermal pressure does not change. The second noticeable jump in the density distribution marks the outer edge of the ionized part of the shell. The outer side of the shell remains neutral as the number of the ionizing photons is not sufficient to photoionize all the swept-up gas. The density in the neutral segments grows two orders of magnitude as the gas temperature drops from 10^4 K in the inner ionized part of the shell to 10^2 K in the neutral skin.

In the bottom two panels of the figure the results for models VHDL and VHDE are plotted on the diagnostic diagram proposed in Yeh & Matzner (2012) discussed in Section 6.3 in order to discriminate between the wind and radiation-dominated regimes. One can note that in the leaky/momentum-dominated bubble model the enhancement of thermal pressure inside the wind-blown shell provided by radiation pressure remains small (the upper and middle left-hand panels), in this case the ratio of thermal pressure at the outer (neutral) and inner (ionized) edge of the shell, P_{edge}/P_s, reaches the maximum value of 1.47 at about 3.3 Myr, and the shell evolves in the wind-dominated regime ($\log \Omega > 0$, solid lines on the bottom panels). This implies that the impact of radiation pressure on the shell dynamics is not significant in this case. In the calculations with a low (10%) heating efficiency the situation is different. The value of P_{edge}/P_s in this case reaches 5.83 at about 3.3 Myr and thus in the models with strong radiative cooling in the star cluster volume (low heating efficiency) and at the earliest stages of the star cluster wind-driven bubble evolution one has to take care on the impact that radiation pressure provides on the dynamics and inner structure of the star cluster wind-driven shells.

These calculations reaffirm that radiation pressure may affect the inner structure and dynamics of the wind-driven shell only at the earliest stages of evolution or if a major fraction of the star cluster mechanical luminosity is dissipated or radiated away within the star cluster volume. However, the impact that radiation pressure provides on the dynamics and inner structure of the wind-driven shell is always negligible during the advanced stages of evolution as the flux of radiation energy flux drops rapidly after the first supernovae explosion whereas the mechanical power of the cluster does not.

The results in this Appendix are part of the conference paper Silich et al. (2014) (Guillermo Haro Conference 2013).

Figure Index

Table Index

References

Adamo, A., Östlin, G., Zackrisson, E., Hayes, M., Cumming, R. J., & Micheva, G. 2010a, MNRAS, 407, 870

Adamo, A., Östlin, G., Zackrisson, E., Papaderos, P., Bergvall, N., Rich, R. M., & Micheva, G. 2011, MNRAS, 415, 2388

Adamo, A., Zackrisson, E., Östlin, G., & Hayes, M. 2010b, ApJ, 725, 1620

Arthur, S. J. 2012, MNRAS, 421, 1283

Barlow, M. J., Krause, O., Swinyard, B. M., Sibthorpe, B., Besel, M.-A., Wesson, R., Ivison, R. J., Dunne, L., Gear, W. K., Gomez, H. L., Hargrave, P. C., Henning, T., Leeks, S. J., Lim, T. L., Olofsson, G., & Polehampton, E. T. 2010, A&A, 518, L138

Bautista, M. A., Depoy, D. L., Pradhan, A. K., Elias, J. H., Gregory, B., Phillips, M. M., & Suntzeff, N. B. 1995, AJ, 109, 729

Beltrametti, M., Tenorio-Tagle, G., & Yorke, H. W. 1982, A&A, 112, 1

Bisnovatyi-Kogan, G. S., & Silich, S. A. 1995, Reviews of Modern Physics, 67, 661

Bocchio, M., Jones, A. P., Verstraete, L., Xilouris, E. M., Micelotta, E. R., & Bianchi, S. 2013, A&A, 556, A6

Book, L. G., Chu, Y.-H., Gruendl, R. A., & Fukui, Y. 2009, AJ, 137, 3599

Bruhweiler, F. C., Freire Ferrero, R., Bourdin, M. O., & Gull, T. R. 2010, ApJ, 719, 1872

Burke, J. R., & Silk, J. 1974, ApJ, 190, 1

Cantó, J., Raga, A. C., & Rodríguez, L. F. 2000, ApJ, 536, 896

Capriotti, E. R., & Kozminski, J. F. 2001, PASP, 113, 677

Cernuschi, F., Marsicano, F., & Codina, S. 1967, Annales d'Astrophysique, 30, 1039

Chevalier, R. A., & Clegg, A. W. 1985, Nature, 317, 44

97

References

Compiègne, M., Verstraete, L., Jones, A., Bernard, J.-P., Boulanger, F., Flagey, N., Le Bourlot, J., Paradis, D., & Ysard, N. 2011, A&A, 525, A103

Dawson, J. R., McClure-Griffiths, N. M., Wong, T., Dickey, J. M., Hughes, A., Fukui, Y., & Kawamura, A. 2013, ApJ, 763, 56

Dieter, N. H., & Goss, W. M. 1966, Reviews of Modern Physics, 38, 256

Dopita, M. A., Fischera, J., Sutherland, R. S., Kewley, L. J., Tuffs, R. J., Popescu, C. C., van Breugel, W., Groves, B. A., & Leitherer, C. 2006, ApJ, 647, 244

Dopita, M. A., Groves, B. A., Fischera, J., Sutherland, R. S., Tuffs, R. J., Popescu, C. C., Kewley, L. J., Reuland, M., & Leitherer, C. 2005, ApJ, 619, 755

Dopita, M. A., Groves, B. A., Sutherland, R. S., & Kewley, L. J. 2003, ApJ, 583, 727

Draine, B. T. 1981, ApJ, 245, 880

—. 2011, ApJ, 732, 100

Draine, B. T., & Anderson, N. 1985, ApJ, 292, 494

Draine, B. T., & Salpeter, E. E. 1979, ApJ, 231, 77

Dwek, E. 1981, ApJ, 247, 614

—. 1986, ApJ, 302, 363

—. 1987, ApJ, 322, 812

Dwek, E., & Arendt, R. G. 1992, ARA&A, 30, 11

Dwek, E., & Werner, M. W. 1981, ApJ, 248, 138

Elmegreen, B. G., & Chiang, W.-H. 1982, ApJ, 253, 666

Elson, R. A. W., Fall, S. M., & Freeman, K. C. 1987, ApJ, 323, 54

Everett, J. E., & Churchwell, E. 2010, ApJ, 713, 592

Fall, S. M., Krumholz, M. R., & Matzner, C. D. 2010, ApJ Let, 710, L142

Ferrarotti, A. S., & Gail, H.-P. 2001, A&A, 371, 133

Finson, M. J., & Probstein, R. F. 1968, ApJ, 154, 327

Fisher, D. B., Bolatto, A. D., Herrera-Camus, R., Draine, B. T., Donaldson, J., Walter, F., Sandstrom, K. M., Leroy, A. K., Cannon, J., & Gordon, K. 2014, Nature, 505, 186

References

Freyer, T., Hensler, G., & Yorke, H. W. 2006, ApJ, 638, 262

Goldreich, P., & Kwan, J. 1974, ApJ, 189, 441

Goldsworthy, F. A. 1958, Reviews of Modern Physics, 30, 1062

Gomez, H. 2013, in Proceedings of The Life Cycle of Dust in the Universe: Observations, Theory, and Laboratory Experiments (LCDU2013). 18-22 November, 2013. Taipei, Taiwan. Editors: Anja Andersen (University of Copenhagen, Denmark), Maarten Baes (Universiteit Gent, Belgium), Haley Gomez (Cardiff University, UK), Ciska Kemper (Academia Sinica, Taiwan), Darach Watson (University of Copenhagen, Denmark)., 146

Gomez, H. L., Krause, O., Barlow, M. J., Swinyard, B. M., Owen, P. J., Clark, C. J. R., Matsuura, M., Gomez, E. L., Rho, J., Besel, M.-A., Bouwman, J., Gear, W. K., Henning, T., Ivison, R. J., Polehampton, E. T., & Sibthorpe, B. 2012, ApJ, 760, 96

Guhathakurta, P., & Draine, B. T. 1989, ApJ, 345, 230

Guillard, P., Boulanger, F., Pineau Des Forêts, G., & Appleton, P. N. 2009, A&A, 502, 515

Haro, G., & Luyten, W. J. 1962, Boletin de los Observatorios Tonantzintla y Tacubaya, 3, 37

Harper-Clark, E., & Murray, N. 2009, ApJ, 693, 1696

Hirashita, H., & Nozawa, T. 2013, Earth, Planets, and Space, 65, 183

Hopkins, P. F., Quataert, E., & Murray, N. 2011, MNRAS, 417, 950

Indebetouw, R., Matsuura, M., Dwek, E., Zanardo, G., Barlow, M. J., Baes, M., Bouchet, P., Burrows, D. N., Chevalier, R., Clayton, G. C., Fransson, C., Gaensler, B., Kirshner, R., Lakićević, M., Long, K. S., Lundqvist, P., Martí-Vidal, I., Marcaide, J., McCray, R., Meixner, M., Ng, C.-Y., Park, S., Sonneborn, G., Staveley-Smith, L., Vlahakis, C., & van Loon, J. 2014, ApJ Let, 782, L2

Izotov, Y. I., Guseva, N. G., Fricke, K. J., & Henkel, C. 2011, A&A, 533, A25

Izotov, Y. I., Guseva, N. G., Fricke, K. J., Krügel, E., & Henkel, C. 2014, A&A, 570, A97

Ji, L., Wang, Q. D., & Kwan, J. 2006, MNRAS, 372, 497

Johnson, K. E., Leitherer, C., Vacca, W. D., & Conti, P. S. 2000, AJ, 120, 1273

Kewley, L. J., & Dopita, M. A. 2002, ApJS, 142, 35

99

References

King, I. 1962, AJ, 67, 471

King, I. R. 1966, AJ, 71, 64

Koo, B.-C., & McKee, C. F. 1992, ApJ, 388, 93

Krumholz, M. R., & Matzner, C. D. 2009, ApJ, 703, 1352

Krumholz, M. R., & Thompson, T. A. 2012, ApJ, 760, 155

Lamers, H. J. G. L. M., & Cassinelli, J. P. 1999, Introduction to Stellar Winds

Laor, A., & Draine, B. T. 1993, ApJ, 402, 441

Leitherer, C., Schaerer, D., Goldader, J. D., González Delgado, R. M., Robert, C., Kune, D. F., de Mello, D. F., Devost, D., & Heckman, T. M. 1999, ApJS, 123, 3

Mac Low, M.-M., & McCray, R. 1988, ApJ, 324, 776

Marengo, M. 2000, PhD thesis, SISSA/ISAS, Harvard-Smithsonian Center for Astrophysics

Martínez-González, S. 2011, MSc Thesis, INAOE. The Impact of the Stellar Distribution on the Feedback of Super Star Clusters

Martínez-González, S., Silich, S., & Tenorio-Tagle, G. 2014, ApJ, 785, 164

Martínez-González, S., Tenorio-Tagle, G., & Silich, S. 2016, Submitted to ApJ

Mathews, W. G. 1967, ApJ, 147, 965

—. 1969, ApJ, 157, 583

Mathis, J. S., Rumpl, W., & Nordsieck, K. H. 1977, ApJ, 217, 425

Matsuura, M., Dwek, E., Barlow, M. J., Babler, B., Baes, M., Meixner, M., Cernicharo, J., Clayton, G. C., Dunne, L., Fransson, C., Fritz, J., Gear, W., Gomez, H. L., Groenewegen, M. A. T., Indebetouw, R., Ivison, R. J., Jerkstrand, A., Lebouteiller, V., Lim, T. L., Lundqvist, P., Pearson, C. P., Roman-Duval, J., Royer, P., Staveley-Smith, L., Swinyard, B. M., van Hoof, P. A. M., van Loon, J. T., Verstappen, J., Wesson, R., Zanardo, G., Blommaert, J. A. D. L., Decin, L., Reach, W. T., Sonneborn, G., Van de Steene, G. C., & Yates, J. A. 2014, ArXiv e-prints

Matzner, C. D. 2002, ApJ, 566, 302

Mengel, S., Lehnert, M. D., Thatte, N., & Genzel, R. 2002, A&A, 383, 137

Meurer, G. R., Heckman, T. M., Leitherer, C., Kinney, A., Robert, C., & Garnett, D. R. 1995, AJ, 110, 2665

Montier, L. A., & Giard, M. 2004, A&A, 417, 401

Moseley, S. H., Dwek, E., Glaccum, W., Graham, J. R., & Loewenstein, R. F. 1989, Nature, 340, 697

Nath, B. B., & Silk, J. 2009, MNRAS, 396, L90

Ninkovic, S. 1998, Serbian Astronomical Journal, 158, 15

Novak, G. S., Ostriker, J. P., & Ciotti, L. 2012, MNRAS, 427, 2734

Nozawa, T., Kozasa, T., Habe, A., Dwek, E., Umeda, H., Tominaga, N., Maeda, K., & Nomoto, K. 2007, ApJ, 666, 955

Nozawa, T., Kozasa, T., Umeda, H., Maeda, K., & Nomoto, K. 2003, ApJ, 598, 785

O'Connell, R. W., Gallagher, III, J. S., & Hunter, D. A. 1994, ApJ, 433, 65

Oey, M. S. 1996, ApJ, 467, 666

Oey, M. S., Watson, A. M., Kern, K., & Walth, G. L. 2005, AJ, 129, 393

Osterbrock, D. E. 1989, Astrophysics of gaseous nebulae and active galactic nuclei, ed. Osterbrock, D. E. ((Mill Valley, CA: University Science Books)

Ostriker, J., & Silk, J. 1973, ApJ Let, 184, L113

Palouš, J., Wünsch, R., Martínez-González, S., Hueyotl-Zahuantitla, F., Silich, S., & Tenorio-Tagle, G. 2013, ApJ, 772, 128

Pollack, J. B., Colburn, D. S., Flasar, F. M., Kahn, R., Carlston, C. E., & Pidek, D. 1979, Journal of Geophysical Research: Solid Earth, 84, 2929

Portegies Zwart, S. F., McMillan, S. L. W., & Gieles, M. 2010, ARA&A, 48, 431

Purcell, E. M. 1976, ApJ, 206, 685

Raymond, J. C., Cox, D. P., & Smith, B. W. 1976, ApJ, 204, 290

Reines, A. E., Johnson, K. E., & Hunt, L. K. 2008, AJ, 136, 1415

Rigby, J. R., & Rieke, G. H. 2004, ApJ, 606, 237

Rodríguez-González, A., Cantó, J., Esquivel, A., Raga, A. C., & Velázquez, P. F. 2007, MNRAS, 380, 1198

Rogers, H., & Pittard, J. M. 2013, MNRAS, 431, 1337

Sarazin, C. L., & White, III, R. E. 1987, ApJ, 320, 32

References

Sharma, M., & Nath, B. B. 2012, ApJ, 750, 55

Silich, S., Bisnovatyi-Kogan, G., Tenorio-Tagle, G., & Martínez-González, S. 2011, ApJ, 743, 120

Silich, S., Martínez-González, S., & Tenorio-Tagle, G. 2014, in Massive Young Star Clusters Near and Far: From the Milky Way to Reionization, 59–62

Silich, S., & Tenorio-Tagle, G. 2013, ApJ, 765, 43

Silich, S., Tenorio-Tagle, G., & Muñoz-Tuñón, C. 2007, ApJ, 669, 952

Silich, S., Tenorio-Tagle, G., & Rodríguez-González, A. 2004, ApJ, 610, 226

Silich, S., Tenorio-Tagle, G., Torres-Campos, A., Muñoz-Tuñón, C., Monreal-Ibero, A., & Melo, V. 2009, ApJ, 700, 931

Smith, L. J., Westmoquette, M. S., Gallagher, J. S., O'Connell, R. W., Rosario, D. J., & de Grijs, R. 2006, MNRAS, 370, 513

Smith, R. K., Krzewina, L. G., Cox, D. P., Edgar, R. J., & Miller, III, W. W. 1996, ApJ, 473, 864

Snijders, L., Kewley, L. J., & van der Werf, P. P. 2007, ApJ, 669, 269

Spitzer, L. 1978, Physical processes in the interstellar medium

Stickel, M., Lemke, D., Mattila, K., Haikala, L. K., & Haas, M. 1998, A&A, 329, 55

Strickland, D. K., & Stevens, I. R. 2000, MNRAS, 314, 511

Strömgren, B. 1939, ApJ, 89, 526

Temim, T., Dwek, E., Tchernyshyov, K., Boyer, M. L., Meixner, M., Gall, C., & Roman-Duval, J. 2015, ApJ, 799, 158

Temim, T., Sonneborn, G., Dwek, E., Arendt, R. G., Gehrz, R. D., Slane, P., & Roellig, T. L. 2012, ApJ, 753, 72

Tenorio-Tagle, G., Muñoz-Tuñón, C., Pérez, E., Silich, S., & Telles, E. 2006, ApJ, 643, 186

Tenorio-Tagle, G., Silich, S., Martínez-González, S., Muñoz-Tuñón, C., Palouš, J., & Wünsch, R. 2013, ApJ, 778, 159

Tenorio-Tagle, G., Silich, S., Martínez-González, S., Terlevich, R., & Terlevich, E. 2015, ApJ, 800, 131

Tenorio-Tagle, G., Silich, S., Rodríguez-González, A., & Muñoz-Tuñón, C. 2005, ApJ Let, 628, L13

Tenorio-Tagle, G., Wünsch, R., Silich, S., Muñoz-Tuñón, C., & Palouš, J. 2010, ApJ, 708, 1621

Tenorio-Tagle, G., Wünsch, R., Silich, S., & Palouš, J. 2007, ApJ, 658, 1196

Terlevich, R., Terlevich, E., Bosch, G., Díaz, Á., Hägele, G., Cardaci, M., & Firpo, V. 2014, MNRAS, 445, 1449

Tielens, A. G. G. M., McKee, C. F., Seab, C. G., & Hollenbach, D. J. 1994, ApJ, 431, 321

Todini, P., & Ferrara, A. 2001, MNRAS, 325, 726

Tsai, J. C., & Mathews, W. G. 1995, ApJ, 448, 84

Valiante, R., Schneider, R., Bianchi, S., & Andersen, A. C. 2009, MNRAS, 397, 1661

Vanzi, L., Hunt, L. K., Thuan, T. X., & Izotov, Y. I. 2000, A&A, 363, 493

Veltmann, U. I. K. 1979, AZh, 56, 976

Wang, J., Feigelson, E. D., Townsley, L. K., Broos, P. S., Román-Zúñiga, C. G., Lada, E., & Garmire, G. 2010, ApJ, 716, 474

Weaver, R., McCray, R., Castor, J., Shapiro, P., & Moore, R. 1977, ApJ, 218, 377

Whitmore, B. C. 2000, ArXiv Astrophysics e-prints

Whitmore, B. C., & Schweizer, F. 1995, AJ, 109, 960

Whitmore, B. C., Zhang, Q., Leitherer, C., Fall, S. M., Schweizer, F., & Miller, B. W. 1999, AJ, 118, 1551

Wright, E. L. 1981, ApJ, 250, 1

Wünsch, R., Silich, S., Palouš, J., Tenorio-Tagle, G., & Muñoz-Tuñón, C. 2011, ApJ, 740, 75

Wünsch, R., Tenorio-Tagle, G., Palouš, J., & Silich, S. 2008, ApJ, 683, 683

Yamada, K., & Kitayama, T. 2005, PASJ, 57, 611

Yeh, S. C. C., & Matzner, C. D. 2012, ApJ, 757, 108